THE PHYSICAL DYNAMICS OF PATTERNED GROUND

IN THE NORTHERN FOOTHILLS OF THE BROOKS RANGE, ALASKA

by

Pier Paul Overduin

RECOMMENDED: _____

_____

_____

_____

Chair, Civil Engineering Department

APPROVED: _____

Dean, College of Engineering and Mines

_____

Dean of the Graduate School

_____

Date

THE PHYSICAL DYNAMICS OF PATTERNED GROUND

IN THE NORTHERN FOOTHILLS OF THE BROOKS RANGE, ALASKA

A

DISSERTATION

Presented to the Faculty

of the University of Alaska Fairbanks

in Partial Fulfillment of the Requirements

for the Degree of

DOCTOR OF PHILOSOPHY

By

Pier Paul Overduin, M. Sc., H. B. Sc.

Fairbanks, Alaska

December 2005

UMI Number: 3206053

Copyright 2006 by
Overduin, Pier Paul

All rights reserved.

INFORMATION TO USERS

The quality of this reproduction is dependent upon the quality of the copy
submitted. Broken or indistinct print, colored or poor quality illustrations and
photographs, print bleed-through, substandard margins, and improper
alignment can adversely affect reproduction.

In the unlikely event that the author did not send a complete manuscript
and there are missing pages, these will be noted. Also, if unauthorized
copyright material had to be removed, a note will indicate the deletion.

UMI®

UMI Microform 3206053
Copyright 2006 by ProQuest Information and Learning Company.
All rights reserved. This microform edition is protected against
unauthorized copying under Title 17, United States Code.

ProQuest Information and Learning Company
300 North Zeeb Road
P.O. Box 1346
Ann Arbor, MI 48106-1346

Abstract

Periglacial landforms, called patterned ground, change the vegetation, microtopography and organic content of the surface soil horizons. Because they are uniquely products of the periglacial environment, changes in that environment affect their distribution and activity. As surface features, they mitigate heat and mass transfer processes between the land and atmosphere. For environmental change detection, the state of the soil and active layer must be monitored across temporal and spatial scales that include these features. It is suggested here that changes in the state of the active layer due to the abrupt spatial changes in surface soil character lead to changes in the distribution of soil components, soil bulk thermal properties and the thermal and hydrological fluxes result.

The determination of soil volumetric moisture content using the relative dielectric permittivity of the soil is extended to include live and dead low-density feathermoss. High temporal resolution monitoring of the thermal conductivity of mineral and organic soil horizons over multiple annual cycles is introduced, along with a new method for analyzing the results of transient heat pulse sensor measurements. These results are applied to studies of frost boils and soil stripes in the northern foothills of the Brooks Range in Alaska. Active layer ice dynamics determine the thermal properties of the frozen soil in the frost boil pedon. Annual heaving and subsiding of the ground surface reflects these changes in ice content and can be used to estimate active layer ice content as a function of depth. These estimates correlate with bulk soil thermal diffusivity, inferred as a function of depth from temperature data. Differences in soil thermal

diffusivity determine thaw depth differences between frost boil and tundra, and between wet and dry soil stripes. For the latter, deeper subsurface flow through the high organic content wet stripes is delayed until mid-summer; when it does occur, it has a large component normal to the hillslope as a consequence of differential heave. Dynamics in these periglacial landforms can be identified from surface features, highlighting the potential for scaling up their net effect using remote sensing techniques.

Table of Contents PAGE

List of Figures   PAGE

List of Tables PAGE

List of Appendices   PAGE

Acknowledgements

Rothwell, Jörg Sommer, Prof. Matthew Wooller, Roc the Suburban Tipper Yuan, and Dr. Yuriko Yano. Fieldwork was made joyful through greatly appreciated logistic support in the field from Mike Abels and Richard Flanders.

Jeff Oatley sustained me through my time at the Water and Environment Research Center and Bob Bolton's companionship in the Ph. D. and INRA programs propped me up. Martin and Gaby Antunez de Mayolo Wilmking warmly shared their hearth and home, when it was in its infancy - thank you.

Most of my thanks go to Julia.

Chapter 1 - Introduction

Through science, humans are familiarizing themselves with their world. We have learned

that our number, combined with the lifestyles that we choose, is sufficient to begin

changing the movement and distribution of water, air, energy and mass on a global scale

(Watson et al., 2001). We have learned that the Polar Regions play an important role in

the global system, arguably more important than their relative area, population and

economic, demographic or cultural roles. This has led to a rollicking quest by Arctic

researchers to find reliable indicators of climate and related change and, more

importantly, of the trajectory and consequences of change.

Positive feedbacks between surficial and atmospheric processes render the Arctic an

inherently highly dynamic system, which nonetheless may now be undergoing an

unprecedented degree of environmental change (Hinzman et al., 2005). Based on global

climate circulation models, air temperatures in northern high latitude land areas,

particularly the northern regions of North America and northern and central Asia, will

warm more rapidly than the global average, exceeding the global mean warming in each

model by more than 40% (Watson et al., 2001). Observed changes in air temperature and

precipitation means in high latitudes of the northern hemisphere are predicted to

continue. We are faced with the challenges of selecting relevant parameters to

appropriately capture the consequences of these changes and of predicting the responses

of climate-relevant exchanges (such as greenhouse gas or water fluxes) between the land

and atmosphere.

Changes in the terrestrial environment are often observed on the basis of proxies for climate, such as botanical macrofossils (Kienast et al., 2005) or stable isotope records (Stuiver et al., 1995), changes in integrated fluxes such as river discharge (Peterson et al., 2002) or changes in flora or fauna (Griffith et al., 2002). In every case, the observed changes in proxy variables must be linked to climatic drivers before predictions of the consequences of further change can be made. For example, shrubs (Sturm et al., 2001) and spruce trees (Wilmking and Juday, 2005) in Alaska are reacting to changes in their environment, although in both cases, the response is complex making predictions of its feedback to the climate difficult.

Feedbacks between soil processes in permafrost landscapes and larger scale systems complicate the prediction of the change. These feedbacks are largely determined by the interface between the permafrost and the atmosphere, the seasonally freezing and thawing of the surficial soils known as the active layer. For example, the active layer fluctuates seasonally and interannually between source and sink states for carbon exchange with the atmosphere (Oechel et al., 1993); changes in either the heat or moisture balance of the active layer will affect the net role of the tundra soils in the carbon balance. Warming of the active layer will lead to increased carbon fluxes to the atmosphere. Through the entrainment of organic material, cryoturbation is the main mechanism for the sequestration of carbon in the permafrost on the North Slope (Ping et al., 2004), so that decreases in cryoturbation would lead to supplemental increases in carbon fluxes into the atmosphere over decadal and greater time scales. The redistribution of soil organic material and changes in microtopography affect the distribution and routing of soil water,

for example through water track drainage of slopes in permafrost environments. At a small scale, both determine flow paths (Quinton et al., 2000). Trajectories of environmental change that affect the vegetation will thus also affect the hydrology. The non-linear interactions between vegetation and hydrology underscore the importance of understanding the influence of periglacial patterning on hydrology. Kane et al. (2003) examined the impact of surficial permafrost landforms on surface hydrology and found that periglacial features could fragment drainage networks, reducing the contributing area for runoff, in a manner that changed seasonally. Surficial landforms also have the capability to block flow locally, by changing the microtopgraphy along a topographic gradient (Kane et al., 2003). Vegetation changes alter the heat budget at the ground surface, and this can lead to dramatic changes as ground ice melts (e.g. the development of thermokarst), or aggrades (e.g. solifluction through decreased effective stress). The former process can lead either to lake formation (Yoshikawa and Hinzman, 2003) or to lake draining (Smith et al., 2005), while the latter leads to massive structural instability (Buteau et al., 2005). In either case, the critical parameters are the distribution of ground ice, particularly in its segregated form, and the amount of ice that thaws in any particular year. Both parameters may be variable from year to year. Changes in ground ice as a result of thawing can have catastrophic consequences, or lead to changes in groundwater pathways at the watershed scale, particularly in discontinuous permafrost landscapes. Topographic and latitudinal gradients on the North Slope provide transitions in climate (Walker et al., 2004). In the active layer, these gradients are expressed as changes in 1) vegetation, 2) soil organic content and 3) the thermal regime. All three expressions of

climate lead to the ubiquity of patterned ground through the agency of cryopedological

processes such as cryoturbation, ice segregation and frost cracking (MacKay, 1957;

Washburn, 1956). Periglacial patterned ground thus functions as an indicator of past

environmental conditions (e.g. Vliet-Lanoë et al., 2004; Walker et al., 2004). Further

change can also be expected to alter the intensity of cryopedological processes.

Objectives and Hypotheses

In this thesis, I focus on feedbacks between ground patterning and physical processes

operating in the active layer. One aspect of the significance of patterned ground is its self-

organization into deci- to hectometer scale domains of comparatively high and low

organic content soils, or into domains of mineral soil organized by grain-size. Kessler et

al. (2001) simulated the creation of patterns in "cyber tundra" through the agency of

heave, subsidence and the horizontal compression of stone domains. An ice wedge

formation model (Plug and Werner, 2002) also seems to mimic pattern-forming

processes. Mann (2003, p. 355), however, warns that 'models must be treated with

caution, because they can mimic the work of nature but use the wrong mechanisms' and

Burn (2004) points out ways in which Plug and Werner's model (2002) fails to reproduce

field observations. Patterned ground distribution and spatial density seem certain to affect

net fluxes of heat and moisture between the land surface and the atmosphere, while their

occurrence and activity depend on these fluxes. A study of the fluxes and temporal

dependence of soil components, especially ice, represents an attempt to extrapolate point

measurements to the mesoscale occupied by these features. I therefore pursue

investigations of those fluxes, how they vary spatially and over short time scales (diurnal to inter-annual). It is processes working at these timescales that result in the organization of soil domains over the century and greater time scale (Mann, 2003).

Fieldwork is carried out on the North Slope of Alaska, and is concentrated in the northern foothills of Brooks Range. My aim is to (i) develop appropriate field methods to determine the state of the active layer across the small spatial scales associated with patterned ground and across the strong gradients of soil organic content, (ii) use these field methods to quantify the active layer thermal dynamics that create, maintain and degrade these patterns and (iii) investigate the effect of soil patterning on surface thermal and hydrological processes at the slope and small-research basin scale. A series of focussed hypotheses on field methods and natural processes have developed.

Permafrost landscapes are unique in that the agency of intense freeze-thaw cycles and limited subsurface drainage create the unique surficial landforms referred to as periglacial landforms. Spatial variability of vegetation density and species composition is high in patterned landscapes, creating spatial variability in the former two factors (intensity of freeze-thaw cycles and permafrost distribution and temperature).

I hypothesize that the spatial variability of organic soils changes the thermal diffusivity of the active layer in such a way as to exert considerable control over the intensity of the processes, such as cryoturbation, that lead to the initiation and maintenance of patterned ground features. The differences in bulk soil thermal diffusivity lead to differential freezing rates and may lead to frost heave. Frost heave is primarily due to the growth of segregated ice in the soil during freezing and is central to the creation of the small to

intermediate scale (<100 m) periglacial landforms shown in Figure 1.1. The influence of periglacial features, such as soil stripes, hummocks, and solifluction lobes, on hillslope hydrology extends the analysis of these features to a larger scale. Based on the high topographic gradient and the scale of the features, hillslope flowpaths are lengthened by the presence of soil stripes.

In this thesis, I also tackle two problems of methodology. The dependence of bulk dielectric permittivity and volumetric water is expected to differ between moss and organic soil horizons and primarily mineral horizons (as has been shown elsewhere for similar materials); I hypothesize that the hydrophilic surfaces of plant tissue, its tendency to swell on wetting and the additional interfacial area created by cellular walls will all tend to decrease the bulk dielectric permittivity of the wet soil as a function of water content. I also seek to improve analysis of transient heat pulse sensor output data in the hopes of using it to infer soil ice content, a difficult to measure but important parameter in the study of patterned ground.

Outline of Chapters

This thesis is organized as a series of publications, with one publication forming the basis for each of Chapters 2 to 5. Tables and figures referred to in each chapter are found following the references for that chapter.

Techniques for measuring liquid water content and distribution must be able to distinguish changes in these variables in a landscape of varying vegetation and soil organic content at a variety of scales, since the patterns themselves are present from the

centimeter to hectometer scales (Figure 1.1), and be robust enough to distinguish these changes from variations in the distribution of soil materials (in addition to the robustness required by use in an extreme and remote environment). Despite the ubiquity of low bulk density organic horizons and moss as landcover in boreal and tundra regions, few established sensor technologies provide models or calibrations for predicting the liquid water content of these materials. In Chapter 2 of this thesis, I investigate electromagnetic techniques for measuring the volumetric liquid water content of feather moss (Overduin et al., 2005). Together with two other papers on *Sphagnum* moss (Yoshikawa et al., 2004) and frozen mineral soils (Yoshikawa and Overduin., 2005), this work establishes a basis for comparing measurements of liquid water content made with a variety of electromagnetic sensors in frozen mineral soils and in two types of low bulk density organic materials. In addition to the practical sensor calibrations generated, we contribute data on the bulk dielectric permittivity as a function of liquid water content in these materials.

The sensitivity of the bulk thermal conductivity of the active layer to changes in its state has been documented (Yoshikawa et al., 2003), although few measurements have been carried out in the field (mostly due to problems associated both with remote installations and measurements that thermally perturb the frozen soil). In Chapter 3, I introduce a field method for measuring the bulk apparent thermal conductivity of soil in which the temperature of the soil surrounding a transient heat source is monitored (Overduin et al., in review). This method is shown to be useful in determining the water and ice contents of the soil. In addition, sensor-soil thermal contact resistance is expected to vary between

mineral and low bulk density, high organic content soils. We base this expectation on differences in particle size and shape and in soil frost susceptibility. The latter leads to differences in frost heave and subsidence. Our method reduces the likelihood of contact resistance affecting the measured value, improves sensitivity in frozen soils and incorporates latent heat effects.

In Chapter 4, I use the techniques developed in Chapter 2 and 3 to measure the seasonal changes in ice content and thermal properties in the active layer in a field setting (Overduin et al., 2003). Frost boils in the Galbraith Lake region of Alaska are selected as an example of well-developed patterned ground, for which the mechanism of formation is not clear. Galbraith Lake frost boils are remarkable because the change in soil properties, especially soil grain size, dry bulk density and organic content, in particular, is dramatic over decimeter and lower spatial scales. These features have the appearance of being sorted circles at the surface. Chapter 4 explores the effects of these differences on the measured apparent thermal conductivity and volumetric heat capacity.

The ice dynamics within the frost boil system are explored in Chapter 5. The seasonally changing soil ice content is assessed using ground surface subsidence and active layer development and the effect of changes in ice content on a meso-scale cluster of frost boils is investigated (Overduin and Kane, submitted; Boike et al., in review). The importance of snow and surface energy balances in winter in determining the shallow active layer ice content is shown, but the deeper active layer ice contents show little inter-annual variability despite dramatic differences in freezing rate.

Appendix A extends the analysis of active layer dynamics to features distributed throughout a watershed (Overduin and Kane, 2005). Patterned ground is likely to affect the soil thermal and hydrological dynamics at the watershed scale, although it is not clear whether it will have an effect on integrative variables such as the basin discharge hydrograph. We suggest that soil stripes are one of three surface morphologies (including water tracks and valley fill) that alter the rate of transport of water downhill at the Imnavait Creek Research Basin. Thaw depth and soil moisture content response to summer rain events are examined. Appendix B represents an update to Chapter 4. It expands upon and re-treats the data with the analytic techniques described in Chapter 5. A number of problems are solved by applying new analytic techniques to the data, and the multi-year data record shows greater seasonal and interannual variability in thermal conductivity for wet soils, while drier soils show much less variability than expected based on literature values.

References for Chapter 1

Boike, J., Ippisch, O., Overduin, P. P., Hagedorn, B., Roth, K., (in review). Water, heat and solute dynamics of a mud boil, Spitsbergen. Geomorphology.

Burn, C. R., 2004. A field perspective on modelling 'single-ridge' ice-wedge polygons. Permafrost and Periglacial Processes 15: 59-65. doi: 10.1002/ppp.475.

Buteau, S., Fortier, R., Allard, M., 2005. Rate-controlled cone penetration tests in permafrost. Canadian Geotechnical Journal 42: 184-197.

Griffith, B., Douglas, D. C., Walsh, N. E., Young, D. D., McCabe, T. R., Russell, D. E., White, R. G., Cameron, R. D., Whitten, K. R., 2002. The Porcupine caribou herd. in: Douglas, D. C., Reynolds, P. E. and Rhode, E. B. (eds.), Arctic Refuge Coastal Plain Terrestrial Wildlife Research Summaries, U.S.Geological Survey, Biological Resources Division, Biological Science Report USGS/BRD BSR-2002-0001, pp. 8-37.

Hinzman, L. D., Bettez, N. D., Bolton, W. R., Chapin F. S., Dyurgerov, M. B., Fastie, C. L., Griffith, B., Hollister, R. D., Hope, A., Huntington, H. P., Jensen, A. M., Jia, G. J., Jorgenson, T., Kane, D. L., Klein, D. R., Kofinas, G., Lynch, A. H., Lloyd, A. H., McGuire, A. D., Nelson, F. E., Oechel, W. C., Osterkamp, T. E., Racine, C. H., Romanovsky, V. E., Stone, R. S., Stow, D. A., Sturm, M., Tweedie, C. E., Vourlitis, G. L., Walker, M. D., Walker, D. A., Webber, P. J., Welker, J., Winker, K. S., Yoshikawa, K., 2005. Evidence and implications of recent climate change in northern Alaska and other Arctic regions. Climatic Change, 72(3): (in press).

Kane, D. L., Gieck, R. E., Bowling, L. C., 2003. Impacts of surficial permafrot landforms on surface hydrology. In: Proceedings of the 8th International Conference on Permafrost, Zurich, Phillips M, Springman SM, Arenson LU (eds). Balkema: Lisse, Netherlands; 507-511.

Kessler, M. A., Murray, A. B., Werner, B. T. and Hallet, B., 2001. A model for sorted circles as self-organized patterns. Journal of Geophysical Research 106(B7): 13287-13306.

Kienast, F., Schirrmeister, L., Siegert, C., Tarasov, P., 2005. Palaeobotanical evidence for warm summers in the East Siberian Arctic during the last cold stage, Quaternary Research, 63(3): 283-300. DOI: http://dx.doi.org/10.1016/j.yqres.2005.01.003

MacKay, J. R., 1957. Field observation of patterned ground. Canadian Alpine Journal 40: 91-101.

Mann, D., 2003. On patterned ground. Science 299: 354-355.

Oechel, W. C., Hastings, S. J., Vourlitis, G. L., Jenkins, M., Riechers, G., Grulke, N., 1993. Recent change of arctic tundra ecosystems from a net carbon dioxide sink to a source. Nature 361: 520-523.

Overduin, P. P., Ping, C.-L., Kane, D. L., 2003. Frost boils, soil ice content and apparent thermal diffusivity. In: Proceedings of the 8th International Conference on Permafrost, Zurich, Phillips M, Springman SM, Arenson LU (eds). Balkema: Lisse, Netherlands; pp. 869-874.

Overduin, P. P., Kane, D. L., Loon, W. K. P. van, (in review). Measuring thermal conductivity in freezing and thawing soil using the soil temperature response to heating. Cold Regions Science and Technology.

Overduin, P. P., Yoshikawa, K., Kane, D. L., Harden, J., 2005. Comparing electronic probes for volumetric water content of low-density feathermoss. Sensor Review 25(3): 215-221.

Overduin P. P., Kane, D. L., 2005. Soil stripes and active layer dynamics on Alaska's North Slope. Abstract presented at: 2nd European Conference on Permafrost, June 11-16, Potsdam, Germany.

Overduin P. P., Kane, D. L., (submitted). Ice content and frost boils: field observations. Permafrost and Periglacial Processes.

Peterson, B. J., Holmes, R. M., McClelland, J. W., Vorosmarty, C. J., Lammers, R. B., Shiklomanov, A. I., Shiklomanov, I. A., Rahmstorf, S., 2002. Increasing river discharge to the Arctic Ocean. Science, 298: 2171-2173.

Ping, C.-L., Clark, M. H., Swanson, D. K., 2004. Cryosols in Alaska. in: pp. 71-94. in: Kimble, J., (ed.) Cryosols: Permafrost-affected soils. Springer Verlag, New York.

Ping, C.-L., Michaelson, G. J., Overduin, P. P., Stiles, C. A., 2003. Morphogenesis of frost boils in the Galbraith Lake area, Arctic Alaska. In: Proceedings of the 8th International Conference on Permafrost, Zurich, Phillips M, Springman SM, Arenson LU (eds). Balkema: Lisse, Netherlands; 897-900.

Plug, L. J., Werner, B. T., 2002. Nonlinear dynamics of ice-wedge networks and resulting sensitivity to severe cooling events. Nature 417: 929–933.

Quinton, W. L., Gray, D. M., Marsh, P., 2000. Subsurface drainage from hummock-covered hillslopes in the Arctic tundra. Journal of Hydrology 237: 113–125.

Smith, L. C., Sheng, Y., MacDonald, G. M., Hinzman, L. D., 2005. Disappearing Arctic Lakes. Science 308: 1429. DOI: 10.1126/science.1108142.

Stuiver, M., Grootes , P. M., Braziunas, T. F., 1995. The GISP2 18O climate record of the past 16,500 years and the role of the sun, ocean and volcanoes. Quaternary Research 44: 341-354.

Sturm, M., Racine, C., Tape, K., 2001. Increasing shrub abundance in the Arctic. Nature 411: 546-547.

Vliet-Lanoë, van B., Magyari, A., Meilliez, F., 2004. Distinguishing between tectonic and periglacial deformations of quaternary continental deposits in Europe. Global and Planetary Change 43: 103-127. DOI:10.1016/j.glopacha.2004.03.003.

Walker, D. A., Epstein, H. E., Gould, W. A., Kelley, A. M., Kade, A. N., Knudson, J. A., Krantz, W. B., Michaelson, G. J., Peterson, R. A., Ping, C.-L., Raynolds, M. K., Romanovsky, V. E., Shur, Y., 2004. Frost-Boil Ecosystems: Complex interactions between landforms, soils, vegetation and climate. Permafrost and Periglacial Processes 15: 171–188.

Washburn, A. L., 1956. Classification of patterned ground and review of suggested origins. Bulletin of the Geological Society of America 67: 823-866.

Watson, R.T. and the Core Writing Team (eds.), 2001. IPCC Third Assessment Report: Climate Change 2001. IPCC, Geneva, Switzerland. pp 184.

Wilmking, M., Juday, G. P., 2005. Longitudinal variation of radial growth at Alaska's northern treeline - Drought stress controls recent changes and possible scenarios for the 21st century. Global and Planetary Change (in press).

Yoshikawa, K., Bolton, W. R., Romanovsky, V. E., Fukuda, M., Hinzman, L. D., 2003. Impacts of wildfire on the permafrost in the boreal forests of interior Alaska. Journal of Geophysical Research, 108(D1): 8148, doi:10.1029/2001jd000438.

Yoshikawa, K., Hinzman, L. D., 2003. Shrinking thermokarst ponds and groundwater dynamics in discontinuous permafrost. Permafrost Periglacial Processes 14(2): 151–160.

Yoshikawa, K., Overduin, P. P., 2005. Comparing unfrozen water content measurements of frozen soil using recently developed commercial sensors. Cold Regions Science and Technology, in press.

Yoshikawa, K., Overduin, P. P., Harden, J., 2004. Moisture content measurements of moss (Sphagnum spp.) layers using recently developed sensors. Permafrost and Periglacial Processes 15(4): 309-318, doi: 10.1002/ppp.505.
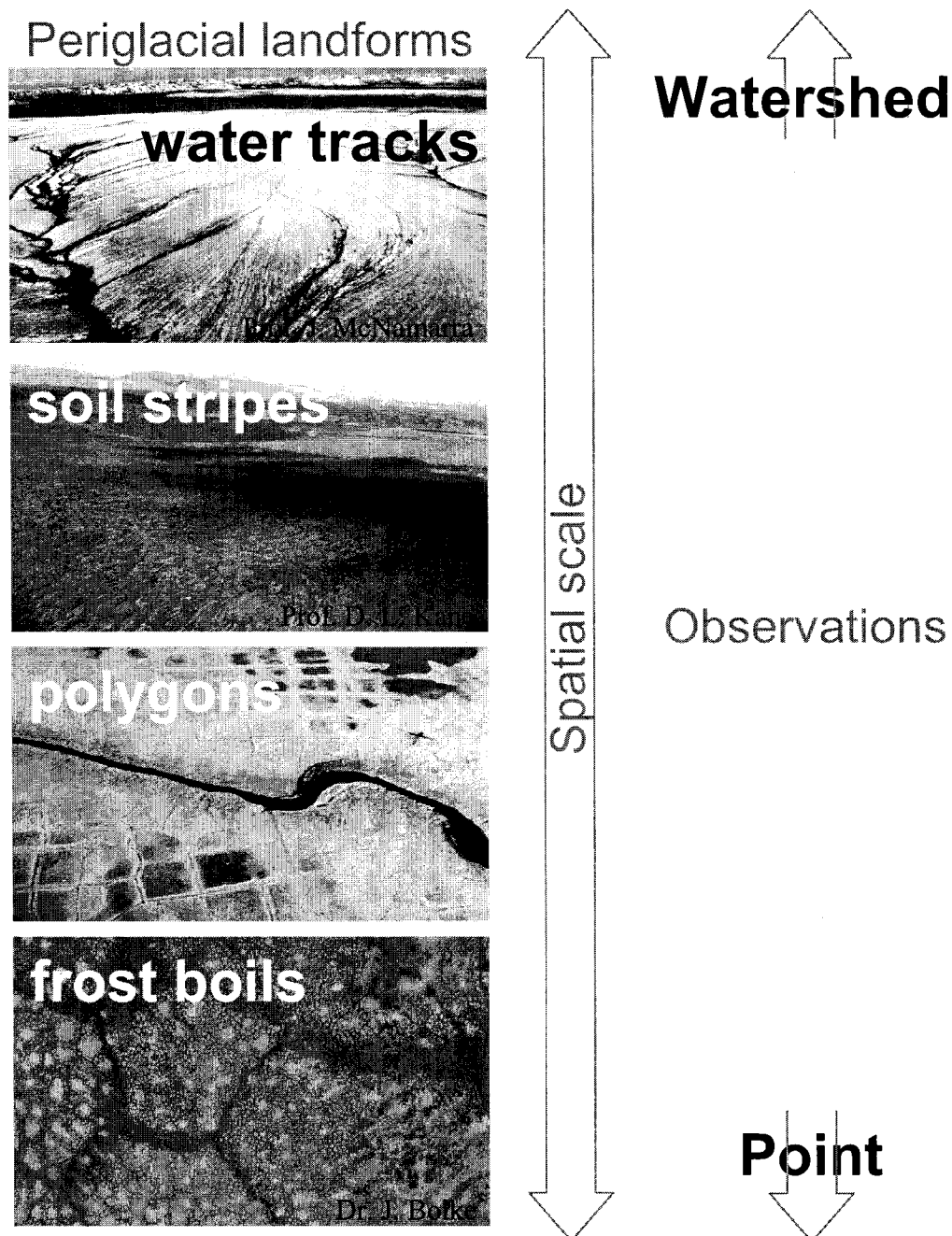
Figure 1.1. The range of spatial scales of periglacial landforms is illustrated through four examples (frost boil, polygons, soil stripes, water tracks). There are also larger and smaller scale examples of periglacial landforms. Observations are usually made at point scale, and transfer processes are generally measured one-dimensionally, even in distributed models. Integral variables, such as hydrograph responses of watersheds deal with heat transfer and mass movement at larger scales, but have little predictive capability over intermediate scales.

Chapter 2 - Comparing electronic probes for volumetric water content of low-density feathermoss[*]

Abstract

Feathermoss is ubiquitous in the boreal forest and across various land-cover types of the Arctic and sub-Arctic. A variety of affordable commercial sensors for soil moisture content measurement have recently become available and are in use in such regions, often in conjunction with fire-susceptibility or ecological studies. Electromagnetic sensors available include frequency and time domain designs with variations in wave guide and sensor geometry, the location of sensor electronics and operating frequency. Few come supplied with calibrations suitable or suggested for low bulk density soils high in organics. We tested seven of these sensors (CS615, ECH$_2$O, GroPoint, Vitel, Theta, TDR, Watermark) for use in feathermoss. Sensors installed in live, dead and burned feathermoss samples, drying in a controlled manner, were monitored continuously and compared to gravimetric determinations of moisture content. Almost all of the sensors tested were suitable for measuring the moss sample water content over a range of water contents from dry to field capacity. We present a unique empirical calibration for each sensor for this material. Differences in sensor design lead to changes in sensitivity as a function of volumetric water content. These differences will affect the spatial averaging

---

over the soil measurement volume. Sensitivity analysis also shows that empirical calibrations are required for different soil types.

Electromagnetic Techniques for Measuring Volumetric Water Content

Since the 1960s, electromagnetic techniques have been studied and used for measuring the volumetric water content of porous media. Most applications in the geosciences have been in mineral soils, for which both empirical relationships (for example, Ledieu et al., 1986; Topp et al., 1980; Stein and Kane, 1983) and theoretical models (for example, Roth et al., 1990) exist for estimating volumetric water content from the bulk relative dielectric permittivity. A few empirical relationships exist for soils high in organic content (Herkelrath et al., 1991; Roth et al., 1992), but not for mosses other than cultivated peat derived from *Sphagnum* moss (Myllys and Simojoki 1996). Based on their review of calibration equations, Jacobsen and Schønning (1995) suggested that organic soils might require special treatment.

Under the assumption that all moss tissues have a common dielectric constant, differences in the bulk dielectric constant of mosses at the same volumetric water content are due to differences in volumetric fractions of air and moss in the sampling volume, i.e. to differences in bulk density and to differences in the distribution of water between bound and free states. Moss differs from low bulk density soils in that the solid phase is composed mostly of organics with highly polar surfaces and a significant portion of the soil water is incorporated into the moss as inner-cellular solution, which may have a

different dielectric constant than that of free water. Both factors can be expected to increase the proportion of water in a bound state relative to mineral soils with similar characteristic particle size and therefore to decrease the apparent relative dielectric permittivity of the bulk soil for a similar water content.

Assuming a representative volume element of soil, a general relationship between the real part of the dielectric permittivity, ε, and the volumetric water content, θ, should exist for a porous medium with spatially homogeneous composition, porosity and texture. In practice, however, the apparent relative dielectric permittivity of the medium is also affected by sensor measurement frequency and geometry and medium structure, density, and water content (Topp et al., 1980). An empirical calibration lumps together the influences of the medium and of the sensor on the measurement. Most calibrations presented in the literature deviate from Topp's relationship (Topp et al., 1980; for example, Jacobsen and Schønning, 1995) and soil texture is generally invoked as the cause of the deviation. Attempts have been made to extend the applicability of TDR calibration curves by soil characteristics such as bulk density (e.g. Malicki and Skierucha, 1989). In practice, this will not eliminate the necessity of sampling the material, or similar materials, in which water content measurements are to be carried out in order to create suitable calibration curves.

More than 23 studies of the TDR technique in a wide variety of materials are available in the literature. Third-order calibration curves for peat moss, litter or soils high in organic or measured carbon content are available from Gray and Spies (1995), Herkelrath et al.,

(1991), Ledieu et al., (1986), Myllys and Simojoki (1996), Pepin et al., (1992), Roth et al., (1992), Schap et al., (1996), Toikka and Hallikainen (1989) and Topp et al., (1980). Mineral soil calibrations (e.g. Dasberg and Hopmans, 1992; Jacobsen and Schønning, 1995; Ledieu et al., 1986; Malicki and Skierucha, 1989; Nadler et al., 1991) predict higher relative dielectric permittivities for volumetric water contents above 0.4 m^3 m^{-3}, consistent with predicted lower relative dielectric permittivities in organic materials vs. mineral soils. Below this value, the regions bounded by organic and mineral calibrations overlap.

Sensor type influences the calibration through sensor geometry and frequency, both of which affect the spatial weighting function applied to the soil volume (Ferré et al., 1996; Nissen et al., 2003; Zegelin et al., 1989). Both the measurement volume and spatial weighting are dependent on sensor design (Ferré et al., 1996; Knight 1992; Zegelin et al., 1989; Pepin et al., 1992). Ferré et al. (1996) showed that sensor output is an average of water content along the wave guides for uncoated wave guides. Coating the wave guides, however, results in unpredictable averaging of water content. For all sensor designs, the soil volume proximal to the sensor wave guides is more heavily weighted in averaging of the apparent relative dielectric permittivity. Thus, the density of plant tissue immediately adjacent to the tines of the sensor exerts a disproportionately large influence on sensor output. Thicker tined-sensors, which shift and compact more of the solid soil matrix (moss tissue) on insertion may have a tendency to change the character of this near-tine material to a greater degree, particularly in a low bulk-density material.

Since TDR was developed and gained common usage as a means of measuring volumetric soil water, numerous other devices exploiting the sensitivity of the relative dielectric permittivity to soil water content have appeared on the market. They have the advantage of being cheaper and simpler to employ than TDR. While TDR measurements are only slightly influenced by the nature of the soil (Ledieu et al., 1986), most inexpensive commercially available sensors, both time domain and capacitance, provide calibrations relating sensor output directly to volumetric water content for use in a limited number of media. A few sensor manufacturers provide high organic carbon calibrations, but none distinguish between organic soil types.

Feathermoss is virtually ubiquitous in the boreal forest and common in higher latitudes. Its presence is sensitive to changes in environmental conditions and particularly to changes in water content. The water content of moss cover in both of these regions is also important because it determines boreal forest fire susceptibility, and because the thermal properties of the surface layers are highly sensitive to moisture levels (Yoshikawa et al., 2003). The bulk thermal conductivity and heat capacity of this surface layer have been shown elsewhere to play a pivotal role in controlling permafrost persistence or degradation (Yoshikawa et al., 2003).

Feather mosses include species from a number of genera, all of which share similar morphological characteristics, such as prostate growth habit and branched stems. Dry bulk densities for feathermoss species have been reported in the literature (Table 2.1) and cover a range from 0.01 to 0.05 kg m^{-3}. Feathermoss changes in bulk density within live and decomposing layers, as well as generally over depth. As an indication of their

variability, values for dry bulk density from a number of sources are plotted with sample

depth in Figure 2.1. Higher dry bulk densities are recorded with greater depth, and reflect

the accumulation of dead moss tissue beneath the living layer.

In this paper, we test the suitability of a number of electromagnetic devices for measuring

the volumetric water content of feathermoss. These sensors are used in low bulk density

moss and feathermoss in the Arctic (Romanovsky and Osterkamp, 2000; Hinkel et al.,

2001) and in feathermoss in the sub-Arctic (Harden et al., 2004) soils. The differences

between sensor calibrations and the influence of their design are important considerations

when planning field measurements and when comparing data derived from different

sensors or using the same sensors when measuring water content in differing materials.

This has particular relevance to climate gradient and remote-sensing studies that seek to

compare results from different ecosystems or to ground-truth spatially distributed data.

Methods

Seven electronic sensors (Figure 2.2) were tested and included two time domain

reflectometry sensors: the TDR100 (Campbell Scientific, Inc.) with the CS605 TDR

probe and the GroPoint (Environmental Sensors Inc.). Four capacitance (sometimes

referred to as frequency domain reflectometry or FDR) sensors were also included: the

CS615 probe (Campbell Scientific, Inc.), the ECH_2O probe (Decagon device, Inc.), the

Hydra Vitel probe (Stevens Water Monitoring Systems Inc.), and the Theta ML2x Delta-

T probe (Delta-T devices, Inc.), as well as a device based on measured electrical

resistance, the Watermark sensor model 200SS (Irrometer Co.). Other than the latter

device, each sensor has unique wave-guide geometry, frequency and electronics, details

of which are given in Table 2.2. The CS615, ECH_20, GroPoint, Hydra Vitel probe and

Theta probe carry on-board electronics, while the TDR 100 CS605 probe is a simple

wave-guide. The wave-guide geometry is important for the ease of installation as it can

disturb the soil matrix on installation to different degrees; this changes the soil volume

properties over which the measurement is made. Finally, the ECH_20 probe is unique

among the electromagnetic sensors tested here, because its tines are encased in a sensor

board.

Methods were selected to demonstrate that the seven soil water sensors listed in Table 2.2

were effective in determining the water content of the live and dead part of

feathermoss. Bulk samples of forest floor feathermoss were harvested in spring (May and

June) from three locations around Fairbanks, Alaska (Birch Hill, University Ski Trails

and Delta Junction). Each block contained a mix of feathermoss species, in each case

predominantly of *Pleurozium* and *Hylocomium* species. Both live and decomposing moss

was collected in each case. A sample of burned, partially charred moss from the Tanana

River flood plain, Alaska was also used for TDR calibration. The four feathermoss

samples were discriminated by layer (live or dead) and cut to known volume. Live and

dead moss layers are usually distinguished on the basis of color, the presence of litter and

the relative proportion of fibric moss tissue. In practice, we found a division of lesser

cohesion between more loosely bound live moss tissue and the underlying, more tightly

matted dead moss tissue, which roughly corresponded to the division based on color. Each layer was over 0.1 m thick.

The seven sensors were placed in the sample block in parallel orientation, extending from the insertion side of the block into its interior. Feathermoss sample blocks were set in an upright position and allowed to soak for more than 24 hours before measurements began. The saturated feathermoss samples, including sensors, were lifted out of the water in mesh baskets, drained to approximately field capacity and weighed during drying in a 30°C forced air oven using an electronic balance. Sensor cables were supported to avoid their influence on the measured weight and the sensors remained inserted in the samples for the duration of the experiment. Balance output was recorded every 5 minutes. Temperature data within the oven and the moss samples was recorded using thermistors at 5-minute intervals during the experiment. Sensor output was measured simultaneously with all seven sensors at five-minute intervals during drying until the sample block reached a stable weight over a twelve-hour period. The volume of the sample block varied with water content and was estimated using its dimensions at a number of points during the drying process.

All sensor output signals were logged with a CR10X datalogger (Campbell Scientific, Inc.). TDR waveforms were analyzed with a computer algorithm based on Heimovaara and Bouten (1990), but including an endpoint determination algorithm that accounts for signal attenuation with increased travel time. All waveforms were analyzed visually, following the recommendations of Dasberg and Hopmans (1992). The Vitel sensor outputs three voltages for soil water content determination and one for sensor head

temperature, so that temperature compensation to dielectric and conductivity values can be performed. The manufacturer provides an algorithm for this compensation. The CS615 sensor outputs a single period measurement from which the bulk soil dielectric constant may be calculated using an empirical polynomial calibration. The manufacturer-supplied calibrations are for 20 °C and a correction coefficient has been developed for measurement temperatures of 10 to 30 °C (Campbell Scientific, Inc., 1996). Output from the ECH_2O (single voltage), GroPoint (single current) and Watermark (single resistance) sensors were left untreated.

For TDR, the measured travel time is related to the relative dielectric permittivity:

$$t = \frac{L\sqrt{\varepsilon}}{c} \tag{2.1}$$

where t is the travel time, ε is the relative dielectric permittivity, L is the length of the TDR wave guides and c is the speed of light in free space (2.997×10^8 m s^{-1}). For the CS615 sensor, the measured response is a time period from which the bulk dielectric constant may be calculated:

$$\tau = 2\left(t_{cir} + \frac{2L\sqrt{\varepsilon}}{c} \right) \tag{2.2}$$

where τ is the period output, t_{cir} is delay of the circuit components, L is the probe length, c is the speed of light. The Vitel Hydraprobe is delivered with binary versions of proprietary software that calculates soil water content from 3 sensor output voltages and sensor temperature from the fourth voltage. Output values include the real and imaginary parts of the soil dielectric constant, the soil conductivity, water content and temperature.

We make the assumption that the sensor response is accurately represented by the calculated real part of the dielectric constant before temperature correction. The Delta-t Theta probe operation has been described by Miller and Gaskin (1999). The measured quantity for the sensor in a datalogging mode is a voltage for which Delta-t provides a linear and a cubic calibration to relative dielectric permittivity:

$$\sqrt{\varepsilon} = 4.44V + 1.10 \tag{2.3}$$

and:

$$\sqrt{\varepsilon} = 4.70V^3 - 6.40V^2 + 6.40V + 1.07 \tag{2.4}$$

where V is the sensor output voltage. The linear relationship is used for calibrations relating the dielectric constant and volumetric water content. Similarly, the ECH_2O form of the empirical calibration suggested by the manufacturer is a linear relationship between sensor output voltage and volumetric water content. GroPoint sensors are not delivered with an algorithm for calculating dielectric constant from sensor output, but a linear function is applied to the current output of the device to obtain volumetric liquid water content.

Results and Discussion

Calibrations

For all probes, excepting the Watermark, calibration curves were generated relating the gravimetrically-determined volumetric water content to sensor output over a moisture

range of $0.025 - 0.15$ m^3 m^{-3} for live moss tissue and from $0.025 - 0.20$ m^3 m^{-3} for dead

moss tissue. Figure 2.3 shows these results except for the Watermark sensor. The given

volumetric water contents range from near field capacity to air-dry values. The field

capacities for the live, dead and burnt mosses were approximately 0.15, 0.20 and 0.20 m^3

m^{-3}, respectively. The rapid change in water content on removal of the sample block from

the water hampered the determination of field capacity and of the bulk dielectric at water

contents near field capacity. In practice, the field capacity depends on the nature of the

underlying material. Least squares linear fits of the data for each of the sensors, excepting

the Watermark, were performed. Coefficients and correlation coefficients are listed in

Table 2.3, along with the probe output domain, expressed as a range of dielectric constant

or sensor output values, for each relationship.

The Watermark sensor output decreased measurably up to volumetric water contents of

5% and 7% for live and dead moss, respectively. At higher water contents, the probe

output is essentially independent of changes in water content, so that the Watermark

probe does little more than distinguish between the air-dry and near-saturated states of

the moss.

The differences between sensor outputs under similar dielectric constant conditions

suggest that the volume of sensitivity and spatial weighting within it affected sensor

output (the volume of sensitivity is defined as the volume of bulk sample over which the

probe measures a spatially weighted average dielectric constant). For all of the sensors,

sample volume proximal to the sensor tines is heavily weighted while that further away

has less influence. Sensor insertion into the sample displaces moss and compression of

the moss around the sensor causes a localized increase in bulk density proximal to the sensor tines. Although the range of tine diameters for the sensors presented here is small (2.5 to 6 mm), this increase in moss bulk density would lead to an underestimate of water content that increases with increasing tine diameter. Ferré (1996) showed that such effects are not independent of tine spacing, diameter and coating and of heterogeneities in the distribution of water around the sensor itself. Sensor dimensions play a larger role in moss than in mineral soils due to probe contact and air void effects, particularly for sensors using lower measurement frequencies than TDR, at which the apparent dielectric permittivity is more sensitive to bulk density (Hallikainen et al., 1985).

For any of these sensors, measurement uncertainty depends on the calibration method. Calibration for the specific material into which the sensor is to be installed is appropriate for permanent installation in a particular soil horizon. If the sensor is to be used in a handheld fashion in the field inserted from the surface, however, a wider range of materials will need to be included in the calibration. Yoshikawa et al. (2004) showed that vertically-oriented Theta and Vitel sensors measured relative dielectric permittivities 0.5 higher than horizontally-oriented, in a live *Sphagnum* moss horizon. Most handheld field use of these sensors also has the potential to penetrate more than one horizon of moss, introducing an additional source of variability. Based on the data presented here, we recommend separate calibrations for live and dead horizons, i.e. for differing stages of decomposition.

The feathermoss TDR calibrations presented here lie within the range of the low bulk density and organic media calibrations listed in the Introduction. The TDR graph of

Figure 2.3 includes data for a block of charred dead feathermoss. This sample was dark, brittle and dusty, with a bulk density of over 0.12 kg m^{-3} for a 0.01 m^3 sample. The TDR calibration curves suggests that burning feathermoss changes the apparent dielectric constant of the moss, presumably as a result of changes in the moss structure and perhaps the formation of carbon deposits. In this study, live and dead moss output values approached each other at low water contents, but diverged with increasing water content (not always in the same direction). Probe output, or measured dielectric constant, was lower for live feathermoss than for dead at most volumetric water contents, for all tested probes except the ECH$_2$O and the GroPoint sensors, for which sensor output values for live and dead moss were closer than ±6% (20 mV). The direction of change in sensor output with moss type is generally consistent with the observed difference in bulk densities (live 0.022; dead 0.06 kg m^{-3}).

Recommendations

We present calibration curves of volumetric moisture content versus instrument output for six sensors in live and dead feathermoss. For all six, calibration curves for the calculation of volumetric water content from measured dielectric constant or sensor output, depending on sensor type, were created for live and dead feathermoss over a volumetric water content range of approximately 0.02 to 0.2 m^3 m^{-3}. Higher volumetric moisture contents generally exceed field capacity, and moisture contents above this level are highly transient under laboratory conditions in which the moss is allowed to drain

after saturation. Calibration in multiple samples of the medium in which each sensor is to be used is advocated, whereby the uncertainty in the calibration is probably affected by spatial variability of the moss bulk density. The selection of samples for calibration should be determined by the intended use of the sensor. Sensor output in live and dead feathermoss layers at the same volumetric water content differ by more than 10% measured water content. Site-specific calibrations must therefore also record the horizons in which the sensors are being used, a consideration relevant to measurements made from the ground surface.

Acknowledgements

References for Chapter 2

Campbell Scientific, Inc., 1996. CS615 Water Content Reflectometer Instruction Manual, Version 8221-07. Campbell Scientific, Inc., Edmonton, Canada.

Dasberg, S., Hopmans, J. W., 1992. Time domain reflectometry calibration for uniformly and nonuniformly wetted sandy and clayey loam soils. Soil Science Society of America Journal 56: 1341-1345.

Ferré, P. A., Rudolph, D. L., Kachanoski, R. G., 1996. Spatial averaging of water content by time domain reflectometry: Implications for twin rod probes with and without dielectric coatings. Water Resources Research 32(2): 271-279.

Gray, A. N., Spies, T. A., 1995. Water content measurement in forest soils and decayed wood using time domain reflectometry. Canadian Journal of Forest Research 25: 376-385.

Hallikainen, M. T., Ulaby, F. T., Dobson, M. C., El-Rayes, M. A., Wu, L.-K., 1985. Microwave dielectric behavior of wet soil – Part I: Empirical models and experimental observations. IEEE Trans. Geoscientific Remote Sensing GE-23(1): 25-34.

Harden, J.W., Neff, J.C., Sandberg, D.V., Gleixner, G., 2004. Chemistry of burning the forest floor during the FROSTFIRE experimental burn, interior Alaska, 1999. Global Biogeochemical Cycles 18: doi:10.1029/2003GB002194.

Heimovaara, T. J., Bouten, W., 1990. A computer-controlled 36-channel time domain reflectometry system for monitoring soil water contents. Water Resources Research 26(10): 2311-2316.

Herkelrath, W. N., Hamburg, S. P., Murphy, F., 1991. Automatic, real-time monitoring of soil moisture in a remote field area with time domain reflectometry. Water Resources Research 27(5): 857-864.

Hinkel, K. M., Paetzold, R. F., Nelson, F. E., Bockheim, J. G., 2001. Patterns of soil temperature and moisture in the active layer and upper permafrost at Barrow, Alaska: 1993–1999. Global and Planetary Change 29: 293–309.

Jacobsen, O. H., Schønning, P., 1995. Proceedings of the symposium: time domain reflectometry applications in soil science. SP Rapport (0908-2581), nr. 11, pp. 25-33.

Kane, D. L., Seifert, R. D., and Taylor, G. S. 1978. Hydrologic properties of subarctic organic soils. University of Alaska Fairbanks, Institute of Water Resources Report No. IWR-88.

King, S., Harden, J. W., Manies, K. L., Munster, J., White, L. D., 2002. Fate of carbon in Alaskan landscape project - database for soils from eddy covariance tower sites, Delta Junction, AK. U.S. Geological Survey Open File Report 02-62. 45 pages.

Knight, J. H., 1992. The sensitivity of time domain reflectometry measurements to lateral variations in soil water content. Water Resources Research 28: 2345–2352.

Ledieu, J., Ridder, P. de, Clerck, P. de, Dautrebande, S., 1986. A method of measuring soil moisture by time-domain reflectometry. Journal of Hydrology 88: 319-328.

Malicki, M. A., Skierucha, W. M., 1989. A manually controlled TDR soil moisture meter operating with 300 ps rise-time needle pulse. Irrigation Science 10: 153-163.

Manies, K. L. Harden, J. W. 2004. Soil data from Picea mariana stands near Delta Junction, AK of different ages and soil drainage type. U.S. Geological Survey Open File Report 2004-1271. 19 pages.

Miller, J. D., Gaskin, G. J., 1999. Theta Probe ML2x: Principles of operation and applications. Macaulay Land Use Reseach Institute Technical Note (2nd ed.), Aberdeen, Scotland.

Myllys, M., Simojoki, A., 1996. Calibration of time domain reflectometry (TDR) for soil moisture measurements in cultivated peat soils. Suo 47(1): 1-6.

Nadler, A., Dasberg, S., Lapid, I., 1991. Time domain reflectometry measurements of water content and electrical conductivity of layered soil columns. Soil Science Society of America Journal 55: 938-943.

Nissen, H. H., Ferré, P. A., Moldrup, P., 2003. Metal-coated printed circuit board time domain reflectometry probes for measuring water and solute transport in soil. Water Resources Research 39(7): 1184.

O'Neill, K. P., Harden, J. W., Trumbore, S. E., 1995. Boreal-ecosystem atmosphere study (BOREAS): 1993 laboratory data and notes: Thompson, Manitoba. USGS Open File Report 95-488.

Pepin, S., Plamondon, A. P., Stein J., 1992. Peat water content measurement using time domain reflectometry. Canadian Journal of Forest Research 22: 532-540.

Romanovsky, V. E., Osterkamp, T. E. 2000. Effects of unfrozen water on heat and mass transport processes in the active layer and permafrost. Permafrost and Periglacial Processes 11: 219-239.

Roth, K., Schulin, R., Fluehler, H., Attinger, W., 1990. Calibration of time domain reflectometry for water content measurement using a composite dielectric approach. Water Resources Research 26: 2267-2273.

Roth, C. H., Malicki, M. A., Plagge, R., 1992. Empirical evaluation of the relationship between soil dielectric constant and volumetric water content as the basis for calibrating soil moisture measurements by TDR. Journal of Soil Science 43: 1-13.

Schaap, M. G., Lange, L. D., Heimovaara, T. J., 1996. TDR calibration of the organic forest floor material. Soil Technology 11: 205-217.

Stein, J., Kane, D. L., 1983. Monitoring the unfrozen water content of soil and snow using time domain reflectometry. Water Resources Research 19: 1573-1584.

Toikka, M. V., Hallikainen, M., 1989. A practical electric instrument for *in situ* measurements of peat properties. In: Dodd, V. A., Grace, P. M. (eds) Land and Water Use, pp. 101-105, Balkema, Rotterdam.

Topp, G. C., Davis, J. L. Annan, A. P., 1980. Electromagnetic determination of soil water content: measurements in coaxial transmission lines. Water Resources Research 16: 574-582.

Trumbore, S.E., Bubier, J. Harden, J.W., Crill, P.M., 1999. Carbon cycling in boreal wetlands: a comparison of three approaches. Journal of Geophysical Research: Atmosphere 104: 27 673-27 682.

Yoshikawa, K., Bolton, W. R., Romanovsky, V. E., Fukuda, M., Hinzman, L. D., 2003. Impacts of wildfire on the permafrost in the boreal forests of interior Alaska. Journal of Geophysical Research 108(D1): 8148-8161.

Yoshikawa, K., Overduin, P. P., Harden, J., 2004. Moisture content measurements of moss (*Sphagnum* spp.) layers using recently developed sensors. Permafrost and Periglacial Processes 15: 309-318.

Zegelin, S. J., White, I., Jenkins, D. R., 1989. Improved field probes for soil water content and electrical conductivity measurement using time domain reflectometry. Water Resources Research 25(11): 2367-2376.

Table 2.1. Bulk density ranges for feather and *Sphagnum* mosses from the literature.

sample	Bulk density [kg m^{-3}]	
	live (# samples)	dead (# samples)
Feather moss species dry bulk density	0.013 (6)[†]	0.049 (6) [†]
	0.019 (6) [‡]	0.041 (8) [‡]
	0.040 (27) [§]	0.092 (7) [§]
	0.022 (23) [¶]	0.06 (1) [¶]
Sphagnum moss species dry bulk density	---	0.108[#]
	---	0.8 – 100[‡‡]
	0.0129 - 0.0314[§§]	
	0.0168 - 0.0406 [§§] (capitulum)	
	0.019 – 1.40 (corresponding to mat thicknesses of 3 – 47 cm) [§§]	

† – Trumbore et al. (1999); ‡ – King et al. (2002); § – O'Neill et al. (1995); ¶ – this study; # – Yoshikawa et al. (2004); ‡‡ – Yoshikawa et al. (2003); §§ – Kane et al. (1978).

Table 2.2. The physical and operating characteristics of the sensors (see also Figure 2.2).

type	Sensor	Characteristics frequency [MHz]	wave shape	sensor output	Dimensions [mm] sensor length	tine diameter	tine spacing (#)
Time Domain	**GroPoint**	2 (0.5 microns)	pulse	1 current [0-5 mA]	205	6	25 (2)
	TDR100	3000 (130 ps)	pulse	waveform voltage *vs.* time	300	4.8	22 (3)
Frequency Domain	**CS615**	55.5	sine	1 pulse [700 - 1400 ms]	288	3.2	28.5 (2)
	ECH₂O	2 (pulse)/6 (sine)	pulse/sine	1 voltage [400-1000 mV]	200	2.5/7.5	6 (3)
	Theta	100 MHz	sine	1 voltage [<1000 mV]	59	3.2	10 (2)
	Vitel	50 MHz	sine	4 voltages [<2500 mV]	57	4	8.6 (4)
Electrical Resistance	**Watermark**	DC	---	1 resistance [0.1-500 kΩ]	70	22.5	---

33

Table 2.3. Calibration coefficients for relating sensor output or measured dielectric to volumetric water content in live and dead feathermoss. The coefficients for the expression:

volumetric water content = a x + b,

are given, where x is either sensor output or the square root of the dielectric constant, as listed in Table 2.2. The range of sensor output or dielectric constant for which the sensors were calibrated in feathermoss is given the rightmost columns (units are listed in Table 2.2).

sensor	moss	coefficients			output domain[†]	
		a	b	R^2	x_{min}	x_{max}
CS615	dead	4.31×10^{-2}	-3.05×10^{-2}	0.981	1.18	1.58
	live	7.36×10^{-2}	-6.27×10^{-2}	0.966	1.14	2.63
ECH$_2$O	dead	5.00×10^{-1}	2.58×10^{-1}	0.937	270	357
	live	6.58×10^{-1}	2.52×10^{-1}	0.975	264	384
GroPoint	dead	5.92×10^{0}	1.00×10^{-2}	0.996	0.02	1.70
	live	6.69×10^{0}	8.08×10^{-2}	0.994	0.02	1.55
TDR	dead	1.55×10^{1}	6.83×10^{-1}	0.997	1.04	1.96
	live	8.05×10^{0}	7.46×10^{-1}	0.929	1.02	3.67
	burnt	2.69×10^{0}	1.77×10^{0}	0.983	1.86	2.34
Theta	dead	1.90×10^{1}	5.80×10^{-1}	0.995	2.40	5.80
	live	9.22×10^{0}	1.10×10^{0}	0.998	1.18	16.8
Vitel	dead	1.31×10^{1}	8.98×10^{-1}	0.993	1.70	2.43
	live	8.05×10^{0}	1.32×10^{0}	0.989	1.37	3.39

† – sensor outputs and units are listed in Table 2.2.
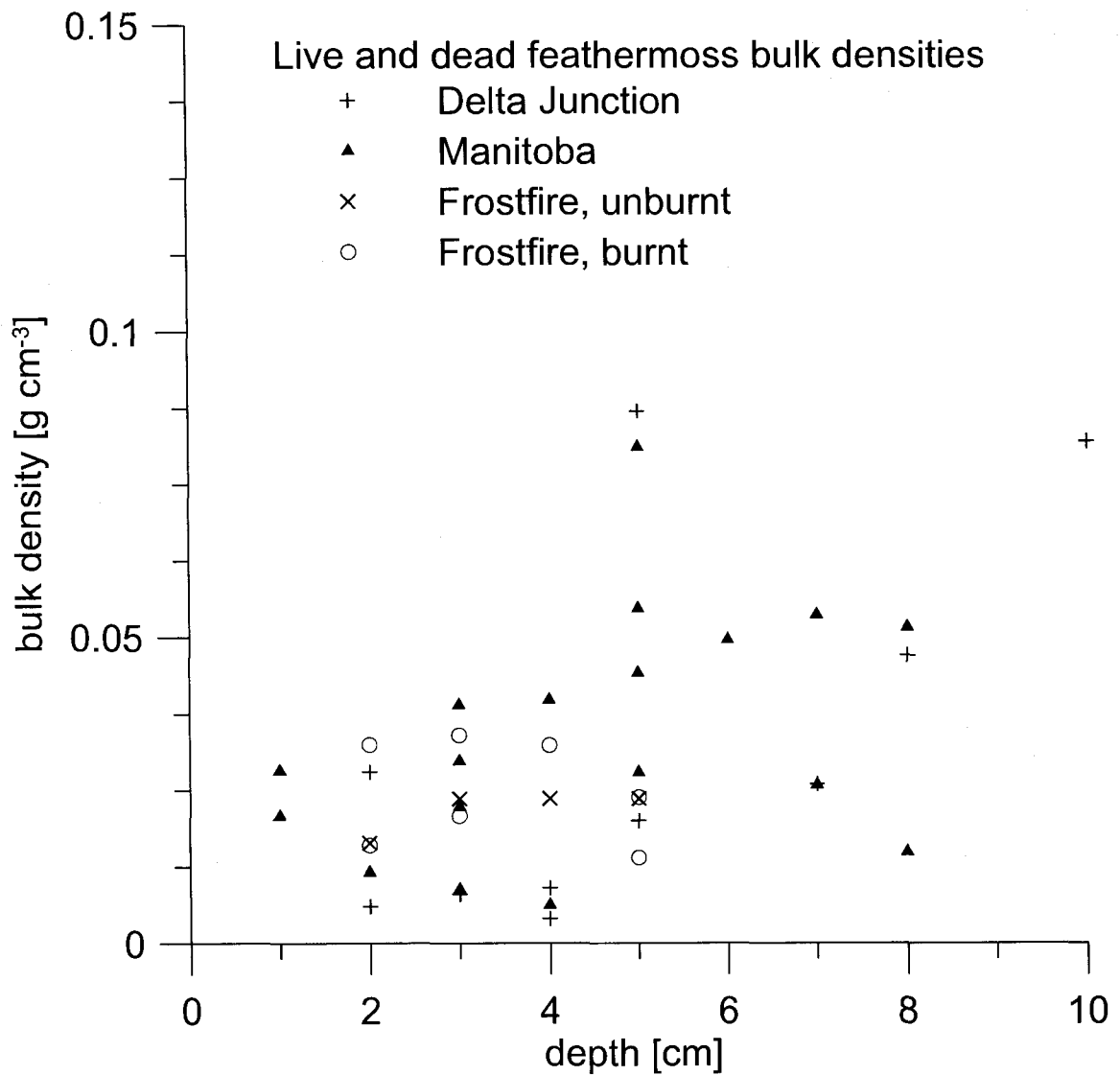
Figure 2.1. Bulk density as a function of depth for live and dead feathermoss layers from Delta Junction, Alaska - Manies and Harden (2004); Manitoba, Canada - O'Neill et al., (1995) and the Frostfire experiment in Alaska - Harden et al., (2004).
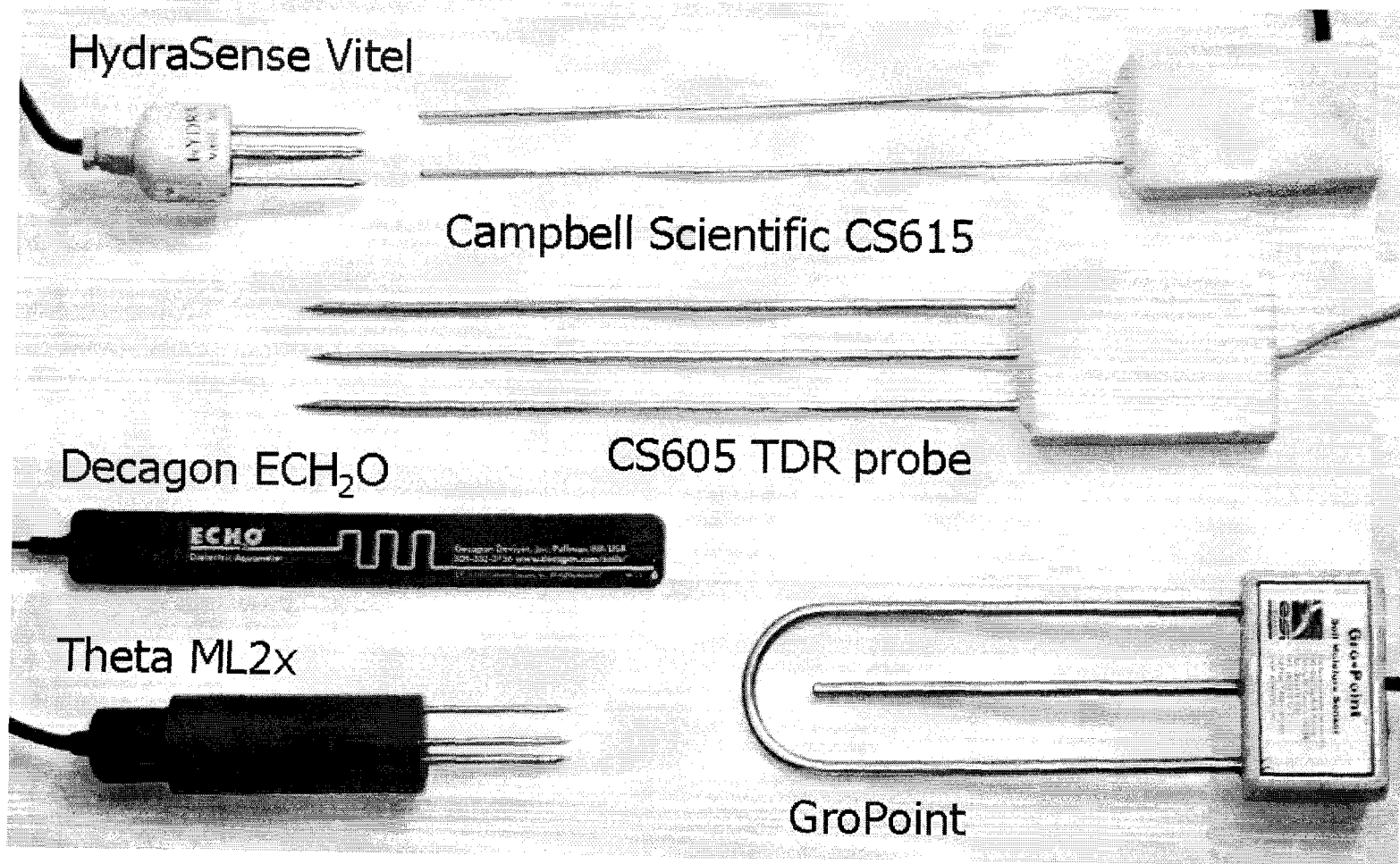
Figure 2.2. Six of the seven sensors analysed are shown at the same scale. The Watermark sensor (not shown) is a small, white, porous cylinder 70 mm long and 22.5 mm in diameter.

Feather Moss

+ dead moss
○ live moss
♦ burnt moss
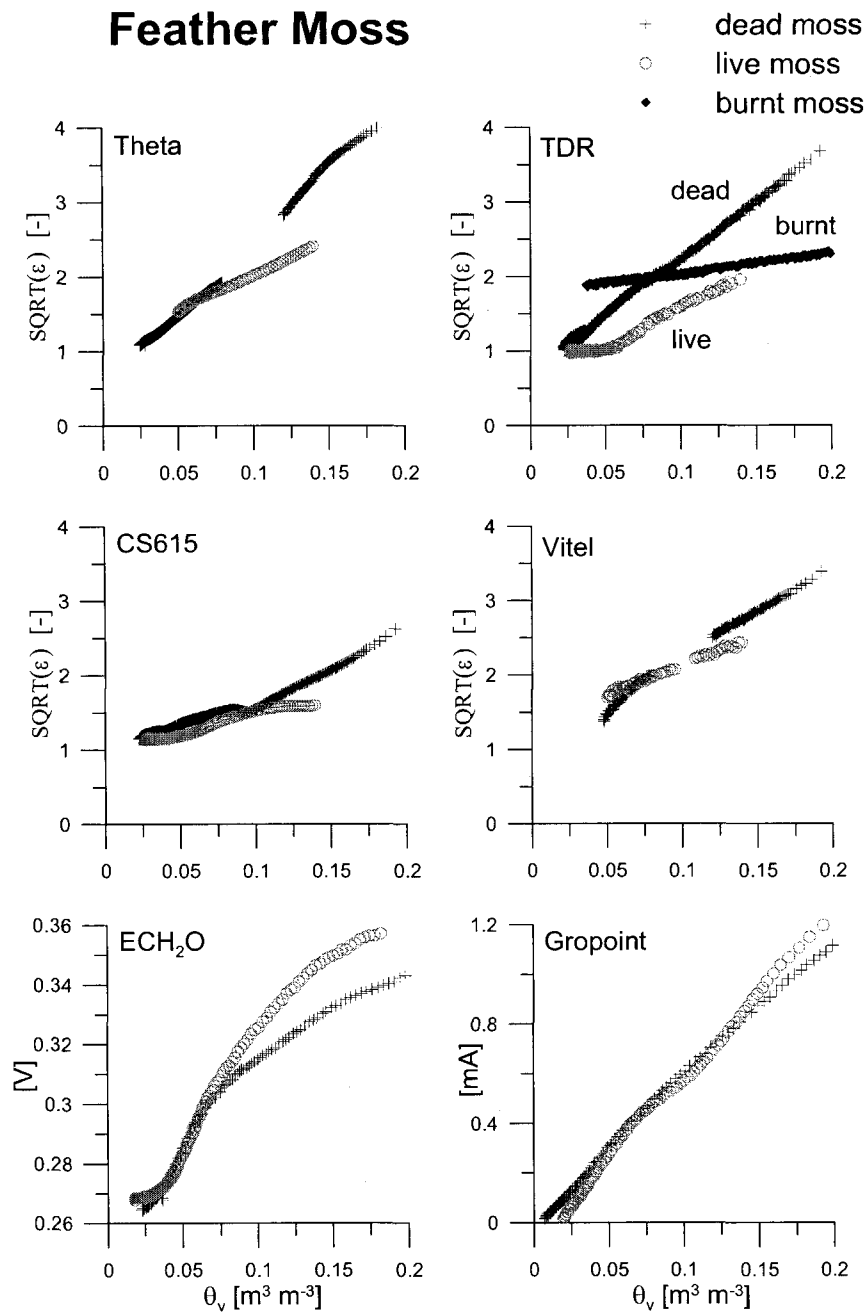
Figure 2.3. Variation in measured dielectric constant (CS615, TDR, Theta and Vitel sensors) or sensor output (ECH₂O and GroPoint) with volumetric soil water content for six sensors for live and dead feathermoss. The TDR graph (upper right) shows additional data from a sample of charred feathermoss.

Chapter 3 - Measuring thermal conductivity in freezing and thawing soil using the soil temperature response to heating[*]

Abstract

The thermal conductivity of the thin seasonally freezing and thawing soil layer in permafrost landscapes (known as the active layer) exerts considerable control over the sensitivity of the permafrost to energy and mass exchanges at the surface. At the same time, the thermal conductivity is sensitive to the state of the soil, varying, for example, by up to two orders of magnitude with varying water contents. *In situ* measurement techniques perturb the soil thermally and are affected by changes in soil composition, for example through variations in thermal contact resistance between sensor and soil. The design of a thermal conductivity sensor for measuring the temperature of the soil rather than the axial heating wire temperature has consequences for the modeling of heat flow. We introduce an approximation of heat flow from a heated cylinder with thermal contact resistance between the cylinder and the surrounding medium. This approximation is compared to the standard line source approximation, and both are applied to data measured over a one-year period in northern Alaska. Comparisons of thermal conductivity values determined numerically using the line source solution, line source approximation and the analytical form of the heated cylinder model fall within 10% of

accepted values, except for measurements made in pure ice, for which all methods of calculation under-predicted the thermal conductivity. Field data collected from a complete freeze-thaw cycle in silty clay show a seasonally bimodal apparent thermal conductivity, with a sharp transition between frozen and thawed values during thaw, but a three-month transition period during freezing. The use of soil composition data to account for changes in heat flow due to the effect of latent heat during phase change results in a relationship between soil thermal conductivity and temperature.

Introduction

The seasonal depth and duration of the active layer in permafrost regions is critical for biological, hydrological and mineralogical processes, as are the intensity and frequency of freezing and thawing events. The thermal conductivity of the shallow surface layer, which thaws and freezes seasonally, is used in the determination of surface heat balance. Various models use the thermal property of conductivity to predict the depth of thaw or freezing of the active layer by assuming a bimodal relationship of winter and summer thermal conductivity values. Such models predict heat transfer, freeze/thaw depth and permafrost stability using these thermal conductivities. Treatment of geothermal data to recover heat flux histories also benefits from observed thermal conductivity data (Beltrami, 2001). Since spatial and temporal variations in soil thermal properties are dramatic (Hinzman et al., 1991; Putkonen, 1998), they must be understood to adequately model physical processes.

Estimates of soil thermal conductivity are based either on models, summarized by

Farouki (1981) or on experimental data (Kersten, 1949). Goodrich (1986) measured the

thermal conductivity of active layer soils at four Canadian locations using a transient heat

pulse probe. His data indicated that this bimodal model is too simple and that the thermal

conductivity values in such diverse soil materials as peat and gravel do not show the

expected seasonal variation in thermal response. He concluded that, at depths shallower

than about 1.0 m, estimates of thermal conductivity based on a simple bimodal, frozen-

thawed model could be grossly in error, while interannual seasonal variations in thermal

conductivity are probably acceptable below a depth of about 0.5 to 1.0 m. Smith and

Riseborough (1985) investigated the effect of assuming a single frozen thermal

conductivity value on the predicted temperature of the subsurface and found that it led to

an over-prediction of the phase change boundary depth. The thermal conductivities of the

shallow surface layers are highly dependent on the composition and state of the soil and

vegetation. Changes in water and ice content produce the greatest changes in thermal

conductivity temporally, which can be of factor ten or more (Yoshikawa et al., 2003) and

generally correspond to drying/wetting or freezing/thawing events. Soil composition in

the periglacial landscape is highly variable spatially due to the agency of cryoturbation.

There remains a need for *in situ* measurements of thermal conductivity in these soils to

determine the influence of water and ice dynamics on the thermal conductivity. Our

objective is to present an improved model for heat flow around a linear heat source in

which the radial temperature difference between two points in the soil is measured. We

demonstrate the use of this model in the laboratory and for field measurements at temperatures close to phase change in freezing and thawing soils.

Models of transient methods for measuring thermal conductivity

Heat transfer model

Transient methods for the measurement of thermal conductivity have a long history (e.g. van der Held and van Drunen, 1949). Most field measurements of thermal conductivity are made using heated wire or needle probes modeled as perfect line conductors. The heat flux can be represented as a solution to the conduction equation in radial coordinates:

$$\frac{\partial^2 T}{\partial r^2} + \frac{1}{r}\frac{\partial T}{\partial r} = \frac{1}{\kappa}\frac{\partial T}{\partial t}, \qquad b < r < \infty \qquad (3.1)$$

where r is the radial dimension, b is the radius of the linear heat source, t is time, T is the temperature of the medium, κ is the thermal diffusivity. Solutions are subject to the conditions:

$$T(r,0) = T_s(r,0) = 0\,^{\circ}\text{C}, \qquad t = 0 \qquad (3.2)$$

where T_s is the temperature of the sensor. For a cylindrical region within in a medium, the heat flux across the cylinder surface is equal to the heat flux leaving the cylinder surface:

$$-k\frac{\partial T}{\partial r} = H(T_s - T), \qquad r = b, t > 0 \qquad (3.3)$$

where we have introduced the thermal conductivity, k, of the region $r > b$, and H, the thermal surface conductance at $r = b$. The heat flux into the medium must be given by:

$$-k\frac{\partial T_s}{\partial r}(2\pi b) = q - C_s\frac{\partial T}{\partial t}, \qquad\qquad r = b, t > 0 \qquad (3.4)$$

where the heat produced within the cylinder per unit length and time is given by q and the heat capacity of the cylinder per unit length is given by C_s.

Line source solution

Data from heated wire or needle probes are usually modeled on a solution for an infinite line heat source (Lachenbruch, 1957) in a homogeneous, isotropic medium. For a continuous line source, the measured temperature difference between two radial points r_1 and r_2 is given by:

$$\Delta T(t) = \frac{q}{4\pi k \Delta r}\int\limits_{r_1^2/4\kappa t}^{r_2^2/4\kappa t}\frac{e^{-u}}{u}du \qquad\qquad (3.5)$$

where q is the heat production of the central heating wire [W m^{-1}], k is the thermal conductivity of the medium [W m^{-1} K^{-1}], Δr is the radial distance over which the temperature difference is measured [m], κ is the thermal diffusivity of the medium [m^2 s^{-1}] and u is an integration variable. In most field measurements in soil, a needle probe with a thermistor or thermocouple embedded in the probe is heated with some known power, and the temperature response of the probe is measured as a function of time. An approximation of the solution is usually used to treat data for the heating curve of the needle:

$$T(r,t) = \frac{q}{4\pi\lambda}\left\{\ln\left(\frac{4\kappa}{\gamma b^2}\right) + \ln t + \frac{1}{1 \cdot 1!}\frac{b^2}{4\kappa t} - \frac{1}{2 \cdot 2!}\left(\frac{b^2}{4\kappa t}\right)^2 + O(t^{-3})\right\}$$

(3.6)

where γ is Euler'sconstant (0.5772156649) and the Landau symbol, $O(t^{-3})$, indicates that

the absolute value of the error in the approximation is less than some constant times t^{-3} at

large enough t. At large times, it is assumed that $b^2/_{4\kappa t}$ is sufficiently small to lead to a

linear dependence on $\ln t$:

$$T(r,t) = \frac{q}{4\pi k}\ln t + c(r)$$

(3.7)

Since the measurement takes place at a fixed position the second-term function, $c(r)$, can

be treated as a constant. Applied to the radial temperature difference,this assumption

results in an expression independent of time for the heating curve:

$$\Delta T = \frac{q}{2\pi k}\ln(r_2/r_1), \qquad r_{1,2}^2/_{4\kappa t} \ll 1$$

(3.8)

the expression for the cooling curve becomes:

$$\Delta T(t > t_s) = \frac{q}{16\pi k \kappa}(r_1^2 - r_2^2)\frac{t_s}{t(t_s - t)}, \qquad r_{1,2}^2/_{4\kappa(t - t_s)} \ll 1$$

(3.9)

where $t = t_s$ is the time at which power to the heating wire is switched off. For both

approximations, the terms in $r^2/4\kappa t$ must be small.

Medium bounded internally by cylindrical region

Relevant analytic solutions are also available for a region bounded internally by a

cylinder (Carslaw and Jaeger, 1990), and for a region bounded internally by a cylinder

with contact resistance (Kristiansen, 1982). Generally only the temperature of the cylinder is considered, reflecting the usual sensor design. The heated cylinder is assumed to be of infinite length (heat flow is restricted to the radial direction) and to act as a perfect conductor (no axial effects of heating). Jaeger (1956) provides solutions for a number of scenarios and investigates the effect of thermal contact resistance on the temperature of the cylinder. Blackwell (1954) examined the effect of contact resistance between the sensor and the medium, but also restricted his analysis to the temperature of the heat source. Van Loon et al. (1989) presents second order time correction to the needle probe model that better describe its behavior at short times. For any system measuring the temperature of the medium, expressions for T rather than T_s are required. The temperature of the medium is determined under the conditions $T(r, 0) = T_0$ and a constant heat supply to the region $r < b$ for times $t > 0$. Based on Blackwell's work, Kristiansen (1982) provided a solution for the temperature field in the medium:

$$T(r,t) = \frac{\alpha q b^2}{k} \int_0^\infty \left(1 - e^{\tau u^2}\right) \frac{\left(R J_0(u\eta) - P Y_0(u\eta)\right)}{u^2(P^2 + R^2)} du \tag{3.10}$$

where u is the integration variable, exp is the exponential function and

$$P = u J_0(u) + k\left(hu^2 - \alpha\right) J_1(u) \tag{3.11a}$$

$$R = u Y_0(u) + k\left(hu^2 - \alpha\right) Y_1(u) \tag{3.11b}$$

where J_z and Y_z are the zth order Bessel functions of the first and second kinds, respectively. We have introduced the dimensionless parameters:

$$h = k/bH \tag{3.12a}$$

$$\eta = r/b \tag{3.12b}$$

$$\tau = 4\kappa t/b^2 \tag{3.12c}$$

$$\alpha = 2\pi b^2 \rho C/S \tag{3.12d}$$

where h is a contact resistance term, η is the dimensionless radius, τ is the dimensionless time and α is twice the ratio of the volumetric heat capacity of the medium, ρC, to that of the sensor, $S/\pi b^2$, where ρ and S are the density of the medium and the heat capacity of the sensor per unit length. As H takes on large values, the solution reduces to that of the heated cylinder without thermal contact resistance. The temperature distribution in the medium depends in a non-linear fashion on the physical parameters. Its integral form requires numerical solution, although DeVries and Peck (1958a) provided a long time approximation that is considered below.

Large time approximation of the medium temperature

DeVries and Peck (1958b) applied Blackwell's (1954) approach to generate a large-time approximation for the temperature of the medium:

$$T(\tau,\eta) - T_0 = \left(\frac{q}{4\pi k}\right)\left[\ln\tau - 2\ln\eta - \gamma + \frac{2}{\tau}(\ln\tau - \gamma) + \frac{1}{\tau}\left(1 - 2\ln\eta + \eta^2\right) + O(\tau^{-2})\right] \tag{3.13}$$

The assumptions that no phase change occurs and that no thermally induced migration of water or vapor occur are implicit. For application to the sensor that we use, expressions for the temperature difference between $\eta_1 = r_1/b$ and $\eta_2 = r_2/b$ are obtained for the heating curve

$$\Delta T(t) = \left(\frac{q}{4\pi k}\right)\left(2\ln\frac{\eta_1}{\eta_2} + \frac{1}{\tau}\left(2\ln\frac{\eta_2}{\eta_1} + \eta_1^2 - \eta_2^2\right)\right) \quad (3.14)$$

After τ_s heating is switched off. The corresponding cooling curve reads as:

$$\Delta T(t) = \left(\frac{q}{4\pi k}\right)\left(\frac{\tau_s}{\tau(\tau_s - \tau)}\left(2\ln\frac{\eta_2}{\eta_1} + \eta_1^2 - \eta_2^2\right)\right) \quad (3.15)$$

For this approximation to order τ^{-2}, dependence of the temperature response on the thermal contact resistance disappears (DeVries and Peck, 1958a). As the thermal heat capacity of the medium or the effective sensor radius approach zero, these solutions reduce to the solutions given by the line source approximation. For the heating curve, we can reformulate the temperature difference as:

$$\Delta T(t) = A\frac{1}{t} + B \quad (3.16)$$

where:

$$A = \frac{qb^2}{16\pi k\kappa}\left(2\ln\frac{\eta_2}{\eta_1} + \eta_1^2 - \eta_2^2\right) \text{ and } B = \frac{q}{2\pi k}\ln\left(\frac{\eta_2}{\eta_1}\right) \quad (3.17)$$

so that a means of calibrating for the effective sensor properties using measurements in materials of known thermal properties is provided. For the cooling curve, the same A appears in the temperature drop:

$$\Delta T(t) = A\frac{t_s}{t(t - t_s)} \quad (3.18)$$

As for the line source approximation, the use of the medium temperature results in the cancellation of terms in the ratio of radial distances for the cooling curve.

Sensitivity

To evaluate the sensitivity of sensor output to changes in parameter values, we express the temperature of the medium (equation 3.10) in a form corresponding to the sensor output as a function of time only:

$$\Delta T(t) = \frac{\alpha q}{\pi b^2 k} \int_0^\infty \left(1 - e^{\pi u^2}\right)\left(R\Delta_J - P\Delta_Y\right)\left(u^2(P^2 + R^2)\right)^{-1} du \qquad (3.19)$$

where:

$$\begin{aligned}\Delta_J &= J_0(u\eta_1) - J_0(u\eta_2) \\ \Delta_Y &= Y_0(u\eta_1) - Y_0(u\eta_2)\end{aligned} \qquad (3.20)$$

The sensitivity of the temperature to its ith parameter, β_i, is given as:

$$\chi_i = \beta_i \frac{\partial T(t, \beta_1, \beta_2 \dots \beta_n)}{\partial \beta_i} \qquad (3.21)$$

where the parameter set from equation 3.19 is $\{\beta_1, \beta_2, \beta_3, \beta_4, \beta_5\} = \{k, \kappa, S, b, H\}$. For surface conductance, the sensitivity is expressed as:

$$\begin{aligned}\chi_H &= H \frac{\partial T}{\partial H} \\ &= \frac{-2q\alpha}{\pi b H^2} \int_0^\infty \left(1 - e^{\frac{\kappa \pi u^2}{b^2}}\right)\left(\frac{\Delta_J Y_1(u) - \Delta_Y J_1(u)}{(P^2 + R^2)} - \frac{2R\Delta_J - 2P\Delta_Y}{(P^2 + R^2)^2}\right)du\end{aligned} \qquad (3.22)$$

and η_1 and η_2 are the dimensionless radii at which temperature difference is measured. The condition for the simultaneous identification of parameter values from a time series of temperature data is the linear independence of the sensitivities over the time period (Beck and Arnold, 1977). The analytical solution is non-linearly dependent on the

parameters, β_i, and a condition for identifiability is not evident. We calculated the sensitivity of the temperature gradient numerically for the five parameters, b, S, H, k, and κ, as a function of time since the start of heating using the adaptive Lobatto quadrature technique and integration limits of 1×10^{-3} and 10. The oscillatory nature of the integrands required a maximum function count limit of at least 1×10^6 to prevent early termination of the integration (Gander and Gautschi, 1998). For the probe radius, heat capacity and heat production used here ($b = 8 \times 10^{-5}$ m, $S = 131$ J m^{-1} K^{-1}, $q = 1.5$ W m^{-1}), with the parameter values of $k = 0.3$ W m^{-1} K^{-1}, and $\kappa = 2.5 \times 10^{-7}$ m^2 s^{-1}, the temperature gradient is less sensitive to contact resistance or probe radius and thermal mass than to medium thermal conductivity or diffusivity by a factor of over 100 as time approaches 180 s (Figure 3.1). H^{-1} was set to zero in Equation 3.21 for the other five sensitivities, and to 3000 W K^{-1} for χ_H. Parameter values were chosen to match sensor characteristics. The magnitude and the general shape of the sensitivities do not change over a range of k, κ and H values extending beyond that encountered in the soil. Increases in thermal diffusivity and thermal surface conductance both increase the temperature gradient at short times (< 10 s). Thus, large changes in H and small changes in κ will affect the shape of the temperature gradient response to heating in a similar fashion. The thermal conductivity influences the temperature gradient most at longer times, in a near linear fashion. The large time approximation can be expected to deliver thermal conductivity, but does not contain recoverable information on the probe characteristics or thermal surface conductance. Repeated numerical solution of the integral solution is

computationally costly. In the following, we compare use of the large time

approximations for the line source and heated cylinder solutions.

Methods

Radial and axial temperature measurements

Transient heat pulse sensors of any design share some basic characteristics. Simultaneous

measurements of the heating power and either the axial temperature, the medium

temperature at some radial distance or the temperature drop between radial positions over

time are compared to some model for heat flow, making it possible to calculate the

effective thermal properties of the medium. For all designs, power requirements are

theoretically adjustable, and modest enough to permit battery operation over long

periods, an advantage for remote sites. The radial sensor also differs from axial probes in

that the temperature around the heat source is monitored rather than the temperature of

the heat source. This design confers the advantage that less power is required since

thermopile sensitivity to small variations in thermal gradient is greater than most

thermistor or thermocouple resolutions. By measuring the temperature difference

between two points, higher accuracy and lower susceptibility to drift can be achieved

than for absolute temperature measurements. The thermopile also averages the radial

temperature gradient over some axial length (and for the sensor we use, over two angular

directions), minimizing the influence of localized heterogeneities on heat flow. For axial

sensors, a thermal contact resistance is created when the temperature sensor is embedded within the heat source (Cull, 1978). Measuring the temperature of the medium at some distance from the heat source partially avoids this problem, and provides a wider range of scales over which the thermal conductivity may be measured. Disadvantages include the enhanced potential for contact resistance between the sensor and the medium, since the sensor's area is quite large compared to the more common needle probe, and a reduced ruggedness, since the film containing the thermopile must necessarily have low thermal conductivity and heat capacity.

The transient sensor

We use the TP01 sensor manufactured by Hukseflux Thermal Sensors, which consists of a doubled heating element (diameter: 2×10^{-5} m; length: 0.06 m) embedded in a thin film, in which a radially-oriented thermopile has also been integrated (Figure 3.2). The heating wire extends 20 mm beyond the thermopile in both axial directions to ensure radial heat flow across the thermopile. The thermopile measures the difference in temperature between two points 1 and 5 mm from the line source, averaged over 20 mm. Averaging also occurs over thermopiles on either side of the heating wire.

The difference in temperatures is related to the thermopile output by a calibration factor determined via a one-point calibration in an agar-water solution, in which the agar gel prevents convective heat transfer. The modeled temperature holds under the assumptions that the medium is well characterized by a thermal conductivity at the measurement scale, isotropic and homogeneous; that heat flow is steady, conductive and radial, and is not

subject to any contact resistance at the sensor-medium interface. A typical calibration factor is 6.3×10^{-5} V K^{-1} (Hukseflux, 2000). The CR10X datalogger has a 1 µV resolution, which corresponds to a temperature gradient resolution of about 4 K m^{-1}. This corresponds to a mean uncertainty in k of 0.01 W m^{-1} K^{-1} over the k range of 0.3 to 4.0 W m^{-1} K^{-1}, assuming that uncertainties in heat production, thermopile position and measurement times are negligible. The thin film encasing the sensor's heating wire and thermopile introduces a minimum thermal surface conductance. It has a thermal conductivity of 0.2 W m^{-1} K^{-1} and is about 1.5×10^{-4} m thick, leading to a conductance of at most $H = 3000$ W m^{-2}. The temperature dependencies of both the heating wire resistance and thermopile output are possible sources of systematic error. The heating wire resistance varies less than 0.04 % K^{-1} over the temperature range -20 to 20 °C and is neglected. We assume that the opposition of the warm and cold junctions compensates for the first order temperature dependency of the thermopile.

To estimate the thermal conductivity of a sample, the sensor is installed in the sample and a current of measured voltage flows through the heating wire for a period sufficient to establish a "steady" reading. Thermopile output is measured before, during and after heating. In soils, heating typically lasts for 180 s and the temperature gradient is monitored for an additional 180 s after heating ceases. This produces a time series of data during heating and cooling, both of which can be used to estimate soil thermal properties.

Field methods

We have collected data from a site in the northern foothills of the Brooks Range in Alaska (68° 29′ N, 149° 29′ W). The site lies in the Galbraith Lake valley, and is located in lacustrine deposits partially reworked by streams draining into Galbraith Lake as the shoreline receded. The site is thus poorly drained and the water table is within 20 cm of the ground surface during the growing season. The soil is assumed to remain saturated during freezing and thawing. Landcover type is classified as moist non-acidic tundra, the soil pedon is classified as a cryaquept and the soil horizons are contorted by cryoturbation (Ping et al., 1998). Permafrost temperatures at 20 m are about –5 °C (Osterkamp 2003). Installation of sensors followed careful excavation of a soilpit. Soil was removed by horizon, and replaced and compacted to close to the original density. Sensors were installed in undisturbed soil in the pit wall. The thin film thermal conductivity sensors installed here require careful insertion; we used a thin knife blade to insert the sensor into the soil, a method which has the potential to create gaps around the sensor. The soil here is subject to frost heave, and since data were collected after one complete freeze-thaw cycle, it is assumed that the soil has compacted around the sensor. Measurements considered in this study were taken from sensors installed in a silty clay soil at 0.37 m below the ground surface. Soil at this location had an oven-dry (105 °C) bulk density of 0.5 g cm^{-3}, with less than 3% carbon content and particle size percentages by weight of 42% clay, 45% silt and 13% sand (Soil Survey Staff, 2005).

For this field deployment, a datalogger (CR10X, Campbell Scientific Inc.) controlled the relays connecting the heating wire to the power source. In these remote field installations, a 12 V battery, recharged continuously by a 50 W solar panel, is used as the electrical power source for the heating wires. The power required for frequent measurements were met by this system (including a meteorological station with TDR unit); enough reserve power was produced to continue measuring through the winter darkness (November-February). The datalogger also measures heating power and thermopile voltage. Data in the field were analyzed using the line source approximation, following the manufacturer's recommendations, and cooling curves were recorded for later reference, whereas in the laboratory, the heating and cooling curves were saved for post-processing.

Soil state

Two thermistors measured temperature proximal to the thermal sensors on an hourly basis. The thermistors were calibrated using a de-ionized water-ice mixture, from which a thermistor-specific offset, δ_o, for the Steinhardt-Hart equation was generated:

$$1/T = 1.28 \times 10^{-3} + 2.37 \times 10^{-4} \left(\ln\left(R_T - \delta_o\right)\right) + 9.06 \times 10^{-8} \left(\ln\left(R_T - \delta_o\right)\right)^3 \qquad (3.23)$$

where R_T is the measured resistance and δ_o is the resistance offset at 0 °C. A linear interpolation of the soil temperatures was performed to estimate the temperature at the sensor location. The thermistors were located 0.05 and 0.12 m from the thermal conductivity sensor. Liquid water content was also measured proximal to the thermal sensors on an hourly basis using time domain reflectometry to measure the bulk apparent dielectric constant of the soil. Topp et al.'s equation (1980) was used to calculate

volumetric liquid water contents in thawed soil. Van Loon et al. (1991) showed that Smith and Tice's (1988) empirical frozen soil calibration could be explained by assigning a lower relative dielectric permittivity to the unfrozen water remaining in the frozen soil. We use their relationship here to calculate the unfrozen water content of the frozen soil. TDR accuracy for volumetric water content is estimated to be better than 5% following Roth and Boike (2001).

Data analysis

In the following, sensor output is referred to as the temperature gradient. For both of the large time approximations, it is assumed that $t \gg r^2/4\kappa$. Soil κ values are expected to vary between 1.2×10^{-7} and 1.4×10^{-6} m^2 s^{-1} (Yershov, 1990), so that $t \gg 2$ to 0.2 s for r_1 = 0.001 m. We consider this condition to be satisfied at $t > 100$ s. Field data are analyzed using the line source approximation, and the heated cylinder approximation. For the latter, the slope of the temperature drop data against inverse time is found:

$$A = \frac{qb^2 C_{app}}{16\pi k_{app}^2}\left(2\ln\frac{\eta_2}{\eta_1} + \eta_1^2 - \eta_2^2\right)$$

(3.24)

The probe-dependent terms are collected to provide:

$$A = E_s \frac{q C_{app}}{k_{app}^2}$$

(3.25)

where

$$E_s = \frac{b^2}{16\pi}\left(2\ln\frac{\eta_2}{\eta_1} + \eta_1^2 - \eta_2^2\right)$$

(3.26)

is an effective probe constant. Estimates of the apparent heat capacity of the soil, C_{app}, at the time of measurement are generated from field soil composition data:

$$C_{app} = \rho C + L_f \rho_w \frac{d\theta_w}{dT} \tag{3.27}$$

where ρC is the thermal heat capacity of the soil (Kay et al., 1981), and is calculated as the sum of the relative volumetric fraction-weighted heat capacity over the three phases ice, water and soil matrix (i, w, s):

$$\rho C = \sum_{n=i,w,s} \rho_n C_n \theta_n \tag{3.28}$$

where ρ_n, C_n and θ_n are the density, specific heat capacity and volumetric fraction of the nth soil phase. θ_i was estimated based on porosity and changes in liquid water content during and after freezing. In doing so, we implicitly assume that ice segregation and moisture redistribution has a negligible effect on the composition of the measurement volume. This soil is susceptible to considerable heave due to ice segregation so this assumption is probably not reasonable, but the bulk thermal heat capacity is only weakly dependent on composition, and moisture redistribution leading to a local 50% increase in ice content leads to less than 5% change in bulk heat capacity. Volumetric liquid water content was calculated as described in the methods section, and the soil matrix volume fraction was assumed to be equal to (1 - θ_{sat}), where the latter term is the volumetric liquid water content at saturation. The analytical solution to the heat flow equation (equations 3.5 and 3.10) cannot be used to measure the apparent thermal conductivity when the apparent thermal conductivity is strongly temperature dependent (Kay et al.,

1981). This occurs when the liquid water content is strongly temperature dependent, generally at temperatures between -0.5 and 0 °C. The rate of change in liquid water content with temperature for both the freezing and thawing arms of the freezing characteristic curve can be given by an empirical relationship of the form:

$$\theta_w = D|T|^E + F \tag{3.29}$$

where D, E and F are constants (the offset, F, is introduced to better represent the freezing data). These values were used to calculate the release and consumption of latent heat as a function of soil temperature.

Results and Discussions

Sensor calibration

The radial temperature differences measured by the sensor while embedded in ice from degassed, distilled water, in agar gel, in moist clay and in dry sand are plotted as a function of time since the beginning of heating in Figure 3.3. For all four materials, the thermal gradient continues to increase with time throughout heating and its magnitude at long times is inversely proportional to the thermal conductivity of the medium. For high thermal conductivity materials, the thermal gradient approaches a linear rate of increase more rapidly during heating. The thermal gradient falls very rapidly for high k values and slower for low k values within three seconds of the cessation of heating and approaches zero as time increases. The manufacturer's suggestions recommend using the thermal

gradient before and after 180 s of heating, $\Delta T(180)$ - $\Delta T(0)$, for the determination of thermal conductivity (Hukseflux, 2000). Use of the $\Delta T(0)$ term accounts for any extant thermal gradients at the onset of heating. This corresponds to the line source approximation, which represents a constant thermal gradient at large times. Thermal conductivity values calculated for the sand, clay, ice and agar are shown in Table 3.1. The probe constant, E_o, for the heated cylinder is calculated using equation 3.26 and the accepted values for water and agar. This value is used to calculate the thermal conductivity for the other three materials. A manufacturer-supplied probe constant is applied for the line source approximation and line source fit.

The heating curves of the same data are plotted in Figure 3.4 as a function of t^{-1}. Black symbols mark those values used to calculate the linear approximation for long times, gray values are those neglected in the least squares fit. Large time values were chosen to maximize the coefficient of determination. More values are included for high thermal conductivity materials since the thermal gradient resolution decreases with increasing thermal conductivity and since materials higher in thermal diffusivity approach linearity as a function of the inverse time more rapidly. Thermal conductivity values using these methods, as well as the least squares fit to the line source model, and the large time approximation of the heated cylinder, are presented in Table 3.1. The line source solution values are found via least squares curve-fitting to numerical calculations of equation 3.5 with thermal conductivity as the fitting parameter. All methods of determination give values for the porous materials within the accepted range. Values for agar and for ice

show greater deviation from the accepted values. The line source performs best for the agar, while the heated cylinder approximation comes closest to the ice value. The maximum deviation for the agar value is 7%, and 17% for the ice.

Field Data

Least squares fits of equation 3.29 to freezing and thawing data collected over three freezing and thawing cycles from late summer 2001 until summer 2004 are shown in Figure 3.5. Coefficient values are found using least-squares fitting (freezing: {D, E, F} = {0.253, -0.572, 0.051}, $r^2 = 0.98$; thawing: {D, E, F} = {0.169, -0.168, 0}, $r^2 = 0.93$). Hysteresis affects the water content at temperatures above -10 °C and may be result of at least three processes: solute exclusion from the forming ice increases the concentration of solutes in the remaining liquid water, depressing its freezing point; capillarity and the irregularity of the pore space cause hysteresis in a fashion analogous to that of wetting and drying curves and the soil solution may also super-cool before nucleation (Bittelli et al., 2003). The steeper slope of the thawing arm of the freezing characteristic curve close to the freezing point indicates a higher rate of heat consumption with temperature change than during freezing. This results in higher apparent thermal conductivities of thawing soils than for those freezing at the same temperature close to the freezing point. Figure 3.6 shows the soil temperature (at the ground surface and at the thermal conductivity sensor depth), volumetric liquid water content, apparent thermal heat capacity and apparent thermal conductivity as a function of time. The soil temperature at 0.32 m depth has begun to decrease by the beginning of September. The soil reaches a

temperature close to 0 °C by September 12th and remains within 0.5 degrees of 0 °C for more than one month. During this period, warming of the air temperature between October 2nd and 10th lead to an increase of liquid water content relative to the pre-freezing saturation water content of 0.48 $m^3 m^{-3}$.

Bulk soil thermal heat capacity values between 2.2 and 3.0 MJ m^{-3} K^{-1}were calculated, which lie within the range for silty and sandy soils given by Yershov (1990; 1.2 to 3 MJ $m^{-3} K^{-1}$). The apparent thermal heat capacity is shown in Figure 3.6, truncated to a maximum value of 6 MJ m^{-3} K^{-1}. During fall freezing, C_{app} increases to over 800 MJ m^{-3} K^{-1}, due to the fact that measurement times were coincident with the soil having reached the melting point. Putkonen (2003) observed similar values in thermal heat capacity as a function of temperature, with values increasing rapidly as the temperature approached the melting point.

The apparent thermal conductivity (Figure 3.6) of the soil shows a roughly bimodal seasonal variation, with lower values in thawed soil than in frozen. This is expected, as the thermal conductivity of ice is four times as high as that of water. Global climate models that incorporate permafrost usually estimate thaw depth based on bimodal seasonal variation in thermal conductivity between a thawed and frozen value. Laboratory measurements of thermal conductivity presented by Yershov (1990) and Hinzman et al. (1998) show higher values (by factors from 0 to 2, depending on material and ice and water content) for frozen soils than thawed soils for a wide range of soil types, including silt, clays, sands and peats. The thermal conductivity of the soil close to the freezing point is usually assumed to take values close to those that may be

interpolated from the frozen and thawed values at the same total water content (Hinzman et al., 1991). For our observed data, soil thermal conductivity values above 0 °C and below −10 °C are weakly dependent on temperature (Figure 3.7b), primarily as a result of the temperature dependence of the thermal conductivity of water (for positive temperatures) and ice (for negative temperatures). Between −10 and 0 °C, a transition from a stable frozen to a stable thawed thermal conductivity value occurs over a range of sub-zero temperatures. Except for observed large values during phase change, this transition is gradual.

Spikes in the apparent thermal conductivity occur both during spring thaw (2004) and during fall freezing (2003; Figure 3.6), during which values increase from 1.4 and 1.0 W $m^{-1} K^{-1}$ to 2.8 and 1.3 W $m^{-1} K^{-1}$, respectively. The fall spike is more easily recognized in the line source thermal conductivity. These spikes are observed in other years and for other sensors, and the spring peak is usually greater in magnitude than the fall peak. Since the soil is not in thermal equilibrium during freezing and thawing, the frequency and timing of measurement can affect the magnitude of the spike. With a mean 12-hour measurement period, there is a sharp discontinuity in the time series of apparent thermal conductivity, so that the duration of this spike can be estimated. It lasts 6 and 11 days in the spring and fall, respectively. In the fall, the spike occurs between temperatures of -0.5 and -1.1 °C, with liquid water contents between 0.2 and 0.3. During thawing, the spike begins at -1.9 °C and returns to a stable thawed value after soil temperatures reach 1.1 °C. Thawing occurs over a shorter time span than freezing. The soil temperature increases from -0.5 to +0.5 °C in less than one week, while the decrease from +0.5 to -0.5 °C

occurs over more than one month. At this soil depth, the mean volume-normalized rate of freezing is -1.3 MJ d^{-1} over an 80-day period while the mean rate of thawing is 5.0 MJ d^{-1} over a 22-day period. Apart from the influence of different energy balances at the surface, soil warming is speeded relative to freezing by the infiltration and refreezing of melt water from shallower horizons, and by the absence of an insulating snow layer.

The line source approximation gives greater values of apparent thermal conductivity during phase change (Figure 3.6, bottom graph) in the periods after the fall freezing spike and before the spring thawing one. The difference between the two approximations reaches 0.6 and 1 W m^{-1} K^{-1} in the fall and spring, respectively. We expect the soil near the surface to saturate before thawing in the spring, but cannot make assertions about the total volumetric moisture content during the fall, when sublimation or vapour transport may be active processes. The heated cylinder approximation values in the spring follow the expected means between frozen and thawed values. The fall values for the heated cylinder approximation, however, decrease slightly during freezing, from 1.2 to 0.7 W m^{-1} K^{-1}, before increasing to winter values, whereas the line source model shows a gradual increase to winter values from thawed values.

Figure 3.7 shows the variation in apparent thermal conductivity calculated with the line source (a) and heated cylinder (b) models using the cooling curve data and the apparent heat capacity calculated via equation 3.27 as a function of soil temperature during two freezing and three thawing periods from May 18, 2002 until July 21, 2004. Cooling (grey circles) and warming periods (black crosses) are differentiated on the figure. The relatively stable apparent thermal conductivities calculated via the heated cylinder

approximation when the soil was below -5 °C in the winters of 2002/2003 and 2003/2004 vary between 1.2 and 1.6 W m^{-1} K^{-1}. Both winters produce similar values as a function of temperature. The values calculated via the line source approximation vary as a result of varying temperature differences after 180 s of heating. Warming values above 0 °C in 2002 lie between 0.65 and 0.90 and increase to the range 0.90 to 1.05 W m^{-1} K^{-1} in the summer of 2004. The apparent thermal conductivity of the freezing and frozen soil changes slowly over time. The hysteresis-like difference between cooling and warming periods of the line source data is not directly related to the liquid water content of the soil, which is similar during the winters of 2002/2003 and 2003/2004. Both approximations result in slight increases in thermal conductivity with decreasing temperature below −10 °C, corresponding to increases in ice content. The rate of increase (0.009 W m^{-1} K^{-2}) in the heated cylinder thermal conductivity is somewhat lower than the rate of decrease in thermal conductivity of pure ice with temperature (0.011 W m^{-1} K^{-2}), probably as a result of the composite nature of the soil. Since ice segregation proximal to the sensor or an increase in contact resistance would lead to higher estimates of k at these temperatures, we suggest that this serves as indication that neither of these processes are operative. The freezing and thawing arms of the apparent thermal conductivity as calculated with the line source approximation (Figure 3.7a) converge to a narrower range of values as a function of temperature in the range (-10, 0 °C) for the heated cylinder approximation (Figure 3.7b). This suggests that the influence of non-conductive processes on the heat flux within the measurement volume can be compensated by accounting for the latent heat change associated with freezing of soil water and melting of ice. The thermal

conductivity values calculated within this temperature range are therefore likely to be close to the true values.

Conclusions

We develop a large time approximation for the radial temperature gradient in a medium surrounding a cylinder with heat production. This approximation is used to model heat flow from a transient heat pulse thermal conductivity sensor while using a time series of heating data to calculate the apparent thermal conductivity of the soil. A commercially available sensor measuring the radial temperature gradient produced results comparable to the line source model. Based on the form of the heated cylinder model, thermal conductivity sensors that measure the radial temperature gradient, rather than the axial temperature, should be operated in a heating, rather than cooling mode. By including only first order terms in time, terms with thermal surface conductance between the sensor and the soil cancel out for the radial temperature difference, suggesting an improvement over axial temperature measurements. Thermal conductivity calculated over a freeze-thaw cycle in the field showed roughly bimodal seasonal variation, with winter thermal conductivities 50 % higher than summer values. Using soil composition data to account for latent heat effects on thermal conductivity measurements leads to convergence of the freezing and thawing arms of the thermal conductivity data, suggesting that the values so obtained represent the actual bulk thermal conductivity of the soil.

This work underscores the importance of recording data on the composition of the soil in parallel with soil temperature, particularly at temperatures close to the freezing point. Soils in most permafrost landscapes typically spend well over a quarter of the year at temperatures between -5 and 0 °C, and this period is critical for many processes in the active layer (carbon release, for example). The relationship between the bulk thermal properties of the soil and the temperature and moisture content of the soil will play a role in determining changes to the soil and permafrost as the climate changes. There remains a need for more thermal conductivity measurements under field conditions.

Acknowledgements

References for Chapter 3

Beck, J. V., Arnold, K. J., 1977. Parameter Estimation. Wiley Sciences.

Beltrami, H., 2001. Surface heat flux histories from inversion of geothermal data: Energy balance at the Earth's surface. Journal of Geophysical Research 10(B10): 21 979-21 993.

Bittelli, B., Flury, M., Gaylon S. C., 2003. A thermodielectric analyzer to measure the freezing and moisture characteristic of porous media. Water Resources Research 39(2): , doi:10.1029/2001wr000930.

Blackwell, J.H., 1954. A transient flow method for determination of thermal constants of insulating materials in bulk. Journal of Applied Physics 25: 137-144.

Carslaw, H. S., Jaeger, J. C., 1990. Conduction of Heat in Solids, 2nd ed. Clarendon Press, Oxford.

Cull, J. P., 1978. Thermal contact resistance in transient conductivity measurements. Journal of Physics 11: 323-326.

DeVries, D. A., Peck, A. J., 1958a. On the cylindrical probe method of measuring thermal conductivity with special reference to soils. I Extension of theory and discussion of probe characteristics. Australian Journal of Physics 11: 255-271.

DeVries, D. A., Peck, A. J., 1958b. On the cylindrical probe method of measuring thermal conductivity with special reference to soils. II Analysis of moisture effects. Australian Journal of Physics 11: 409-423.

Farouki, O. T., 1981. Thermal properties of soils. Cold Region Research and Engineering Laboratory (CRREL) Monograph 81-1.

Gander, W., Gautschi, W., 1998. Adaptive Quadrature – Revisited. Eidgenössiche Technische Hochschule, Zürich, Report 40: 84-101.

Goodrich, L. E., 1986. Field Measurements of Soil Thermal Conductivity. Canadian Geotechnical Journal 23: 51-59.

Held, E. F. M. van der, Drunen, F. G. van, 1949. A method of measuring the thermal conductivity of liquids. Physica. 15:865-881.

Hinzman, L. D., Kane, D. L., Gieck, R. E., Everett, K. R., 1991. Hydrologic and thermal properties of the active layer in the Alaskan Arctic. Cold Regions Science and Technology 19(2): 95-110.

Hinzman, L. D., Goering, D. J., Kane, D. L., 1998. A distributed thermal model for calculating soil temperature profiles and depth of thaw in permafrost regions. Journal of Geophysical Research 103(D22): 28 975-28 991.

Hukseflux Thermal Sensors, 2000. TP01: Thermal Properties Sensor. Delft, Netherlands.

Jaeger, J. C., 1956. Conduction of heat in an infinite region bounded internally by a circular cylinder of a perfect conductor. Australian Journal of Physics 9: 167-169.

Kay, B. D., Fukuda, M., Izuta, H., Sheppard, M. I., 1981. The importance of water migration in the measurement of the thermal conductivity of unsaturated frozen soils. Cold Regions Science and Technology. 5: 95-106.

Kersten, M., 1949. Laboratory research for the determination of the thermal properties of soils. University of Minnesota, Engineering Experimental Station, Bulletin 28.

Kristiansen, J. I., 1982. The transient cylindrical probe method for determination of thermal parameters of earth materials. Geoskrifter 18: 1-154.

Lachenbruch, A., 1957. Measurement of thermal conductivity of frozen soils. Transactions of the American Geophysical Union. 38(5): 691-697.

Lide, D. R., ed., 2005. CRC Handbook of Chemistry and Physics, CRC Press, Florida.

Loon, W. K. P. van, Perfect, E., Groenevelt, P. H., Kay, B. D., 1991. Application of dispersion theory to time-domain reflectometry. Transport in Porous Media 6: 391-406.

Loon, W. K. P. van, Haneghem, I. A. van, Schenk, J., 1989. A new model for the non-steady-state probe method to measure thermal properties of porous materials. International Journal of Heat and Mass Transfer 32: 1473-1481.

Osterkamp, T. E., 2003. A thermal history of permafrost in Alaska. In: Proceedings of the Eighth International Conference on Permafrost, 21–25 July 2003, Balkema Publishers, Zurich, Switzerland, pp. 863–868.

Ping, C. L., Bockheim, J.G., Kimble, J.M., Michaelson, G.J., Walker, D. A., 1998. Characteristics of cryogenic soils along a latitudinal transect in arctic Alaska. Journal of Geophysical Research, 103(D22): 28 917-28 928.

Putkonen, J., 1998. Soil thermal properties and heat transfer processes near Ny Alesund, Northwestern Spitsbergen, Svalbard. Polar Research, 17(2): 165-179.

Putkonen, J., 2003. Determination of frozen soil thermal properties by heated needle probe. Permafrost and Periglacial Processes 14: 343-347.

Roth, K., Boike, J., 2001. Quantifying the thermal dynamics of a permafrost site near Ny-Ålesund, Svalbard, Water Resources Research, 37(12): 2901-2914. doi: 10.1029/2000WR000163.

Smith, M. W., Riseborough, D. W., 1985. The sensitivity of thermal predictions to assumptions in soil properties. In: Fourth International Symposium on Ground Freezing, Sapporo, Japan, August 5-7, 1985, pp. 17-23.

Smith, M.W., Tice, A.R., 1988. Measurement of the unfrozen water content of soils-comparison of NMR and TDR methods. CRREL Report, vol. 88-18. US Army Cold Regions Research and Engineering Laboratory (CRREL).

Soil Survey Staff, 2005. National Soil Survey Characterization Data, Soil Survey Laboratory, National Soil Survey Center, USDA-NRCS - Lincoln, NE.

Topp, G. C., Davis, J. L., Annan, A. P., 1980. Electromagnetic determination of soil water content: Measurement in coaxial transmission lines. Water Resources Research, 16:574-582.

Yershov, E. D., 1990, General Geocryology. Cambridge University Press, 580 pp.

Yoshikawa, K., Bolton, W. R., Romanovsky, V. E., Fukuda, M., Hinzman, L. D., 2003. Impacts of wildfire on the permafrost in the boreal forests of Interior Alaska. Journal of Geophysical Research, 108(D1): 8148, doi:10.1029/2001jd000438.

Table 3.1. Calculated thermal conductivities [W m⁻¹ K⁻¹].

Thermal conductivity [$W\,m^{-1}\,K^{-1}$]		Moist Clay (21 °C)	Dry Sand (21 °C)	Ice (-5 °C)	Water and agar gel (21 °C)
Accepted[a]		1.2 – 1.4	0.3 – 0.35	2.38	0.60
Line source approximation		1.36	0.32	1.98	0.59
Line source model [b]		1.31	0.31	1.97	0.53
Heated cylinder approximation	*slope*	1.33 [c]	0.30 [c]	2.08	—[d]
	intercept	1.45	0.34	2.09	—[d]

a – from Yershov (1990) for sand,, clay and water; from Lide (2005) for ice; b – the parameter η_1/η_2 is estimated from the manufacturer-provided sensor calibrations; c – estimated thermal heat capacities of 1.25 MJ m⁻³ K⁻¹ and 2.8 MJ m⁻³ K⁻¹ for dry sand and moist clay were taken from Yershov (1990); d – used to calculate sensor constant.

Table 3.2: List of Symbols for Chapter 3.

A	constant	--
B	constant	--
C	heat capacity	J kg^{-1} K^{-1}
D	constant used in freezing characteristic curve	--
E	constant used in freezing characteristic curve	--
F	constant used in freezing characteristic curve	--
E_S	effective sensor constant	K s m^{-2}
H	surface thermal conductance	W m^{-2} K^{-1}
J_z	Bessel function of the 1st kind, zth order	--
L_f	latent heat of fusion	J kg^{-1}
P	$= uJ_0(u) + k(hu^2 - \alpha)J_1(u)$	--
Q	heat produced per length of source	W m^{-3}
R	$= uY_0(u) + k(hu^2 - \alpha)Y_1(u)$	--
R_T	thermistor resistance	Ω
S	heat capacity of the heating wire	J m^{-1} K^{-1}
T	temperature of the medium	°C
T_s	heating wire temperature	°C
Y_z	Bessel function of the 2nd kind, zth order	--
b	heat source radius	m
h	Biot number	--
k	thermal conductivity	W m^{-1} K^{-1}
q	heat production per unit length	W m^{-1}
r	radius	m
t	time	s
t_s	time at which heat production ceases	s
u	integration variable	--
z	order, Bessel function	--
ΔT	radial temperature gradient	K m^{-1}
Δ_J	$= J_0(u\eta_1) - J_0(u\eta_2)$	--
Δ_Y	$= Y_0(u\eta_1) - Y_0(u\eta_2)$	--
α	twice the ratio of medium to sensor heat capacities	--
β_i	ith parameter in parameter set	i-dependent
χ_i	sensitivity to ith parameter	i-dependent
δ_o	resistance offset (thermistors)	Ω
γ	Euler's constant, (0.5772156649)	--
η	ratio of radial position to cylinder radius, b	--
κ	medium thermal diffusivity	m^2 s^{-1}

Table 3.2 (continued): List of Symbols for Chapter 3.

π	pi	--
θ_i	volumetric content of soil component i	$m^3\,m^{-3}$
ρ	density	$kg\,m^{-3}$
τ	Fourier number	--
τ_s	dimensionless time at cessation of heat production	--

Subscripts

1, 2	radial positions
app	apparent
i	ice
O	sensor
s	soil
S	sensor
w	water
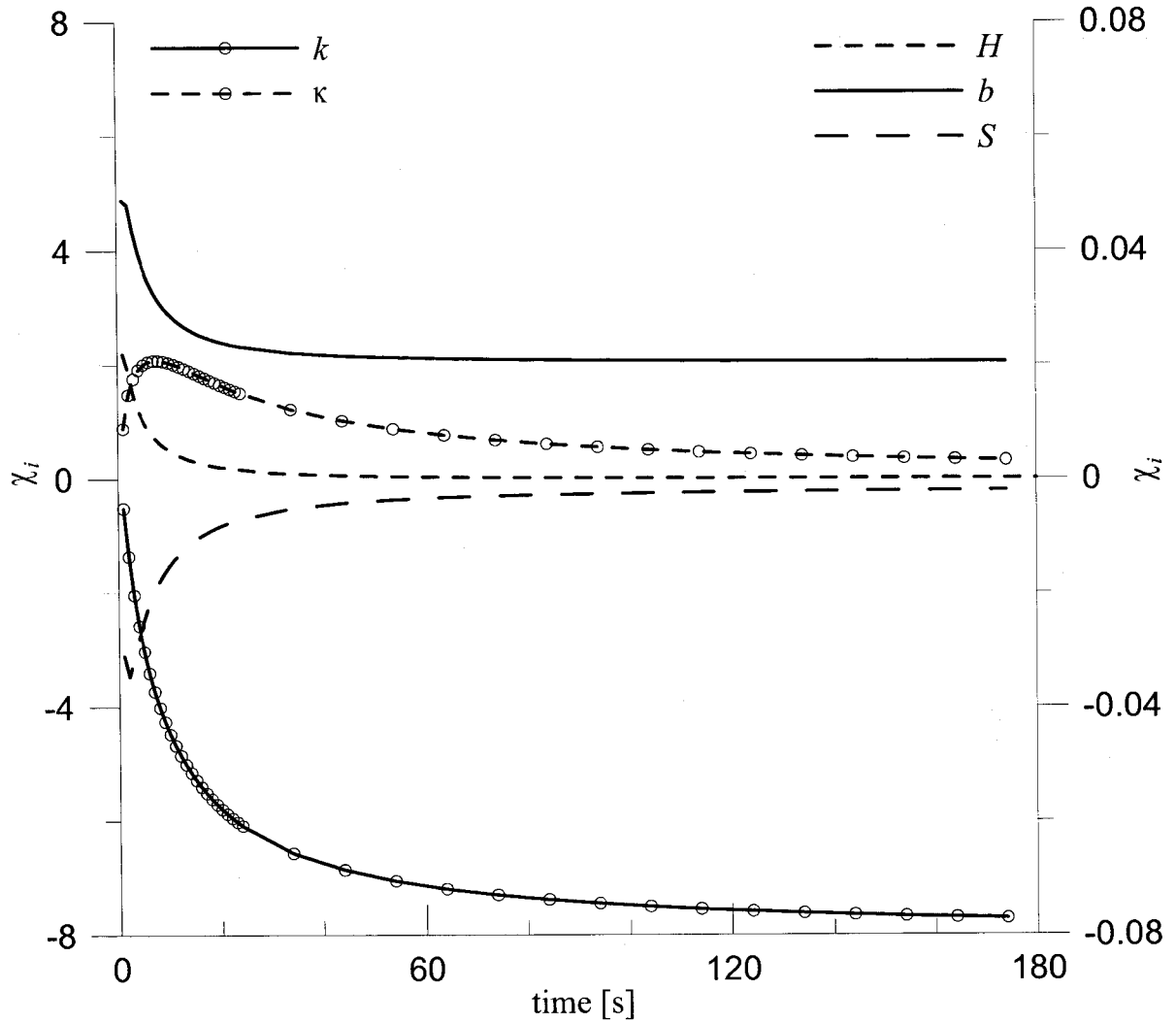
Figure 3.1. Sensitivities of the radial temperature gradient to the parameters for values $b = 8 \times 10^{-5}$ m, $S = 131$ J $m^{-1} K^{-1}$, $q = 1.5$ W m^{-1}, $k = 0.3$ W $m^{-1} K^{-1}$, and $\kappa = 2.5 \times 10^{-7}$ $m^2 s^{-1}$, as a function of time since the beginning of heating. χ_i is defined in the text (equation 3.21). The left hand axis is for k and κ, the right hand axis for H, b and S. H^{-1} was set to zero for the other five sensitivities, and to 3000 W K^{-1} for χ_H. The units of χ_i depend on i.
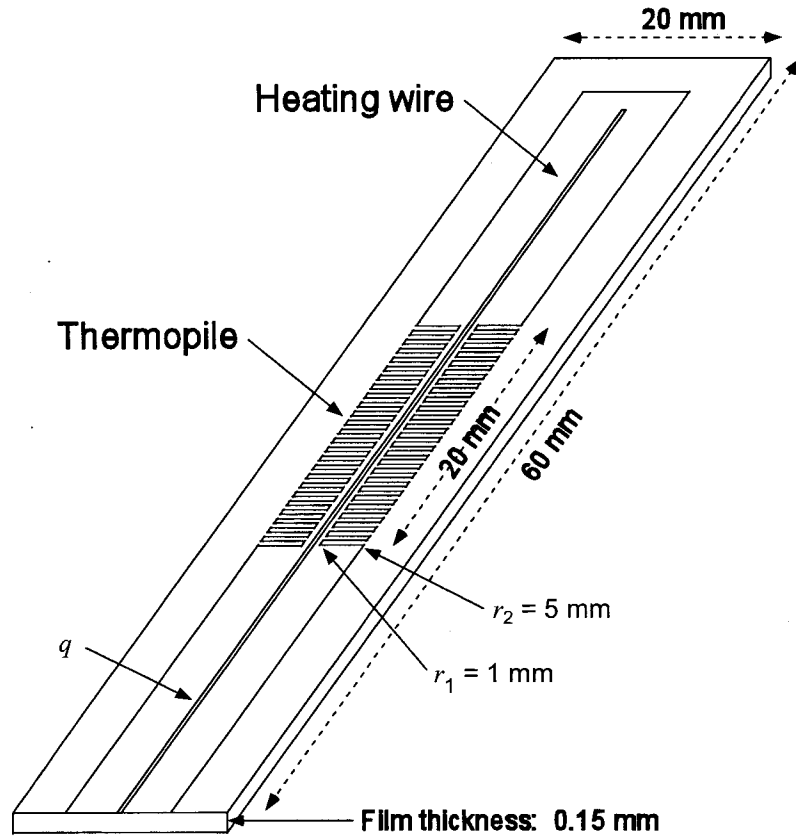
Figure 3.2. Oblique-view schematic diagram of the Hukseflux TP01 thermal properties sensor. The sensor produces a known amount of heat, q, per unit time and length of heating wire along the central heating wire. The temperature difference is measured between radial distances of 1 (r_1) and 5 mm (r_2) from the central heating wire (indicated by q). This temperature difference is averaged over the central 20 mm of the heating wire (longitudinally) and over two angular directions in the plane of the sensor.
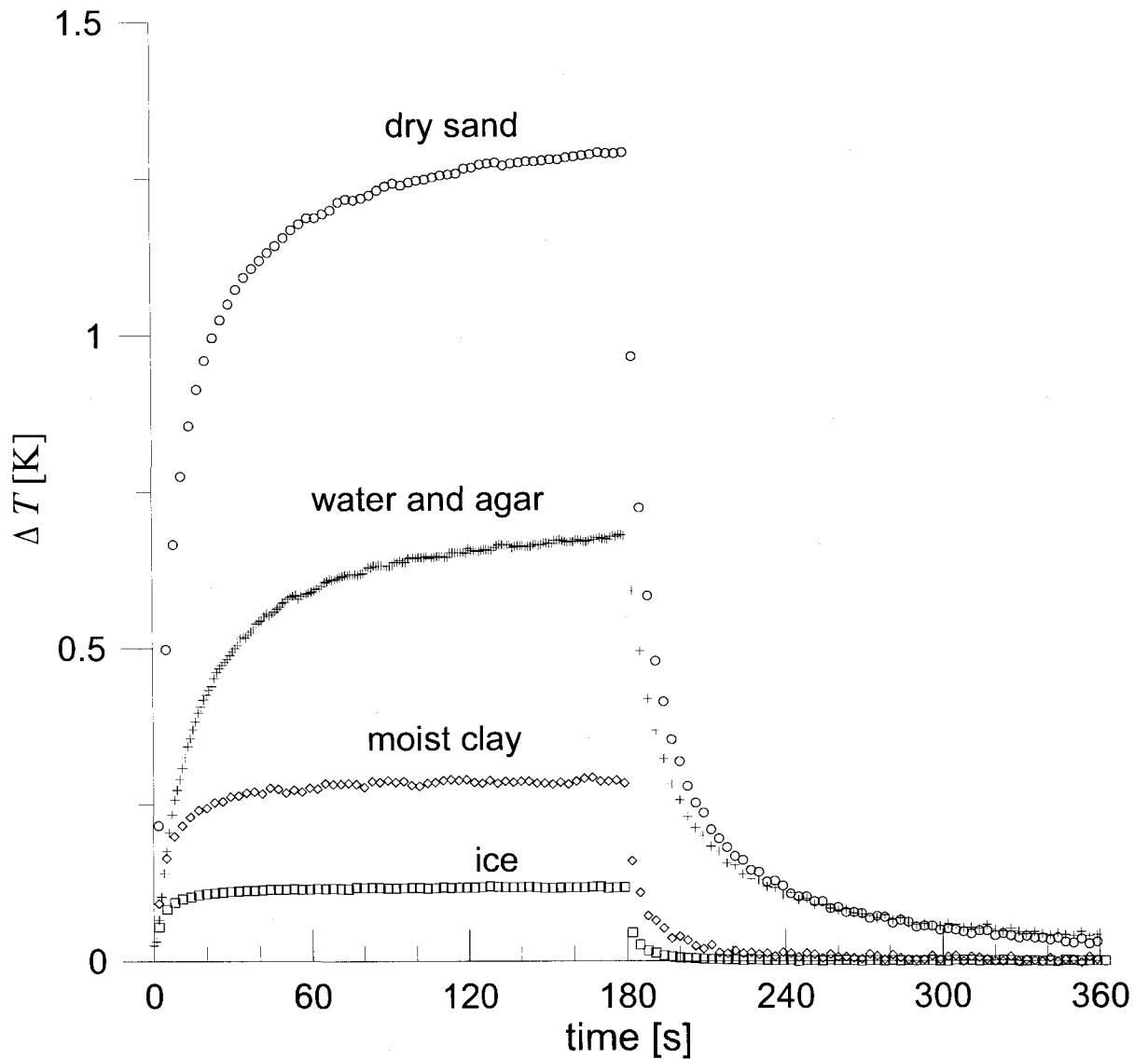
Figure 3.3. The radial temperature difference as a function of time for the first 180 s of heating and then the next 180 s of cooling in four materials is shown. Thermopile and heater voltages are recorded with a datalogger. The former is related to the radial temperature by the thermopile's Seebeck coefficient. Heat production by the heating wire is related to the resistance of the heating wire, the voltage across it and its length.
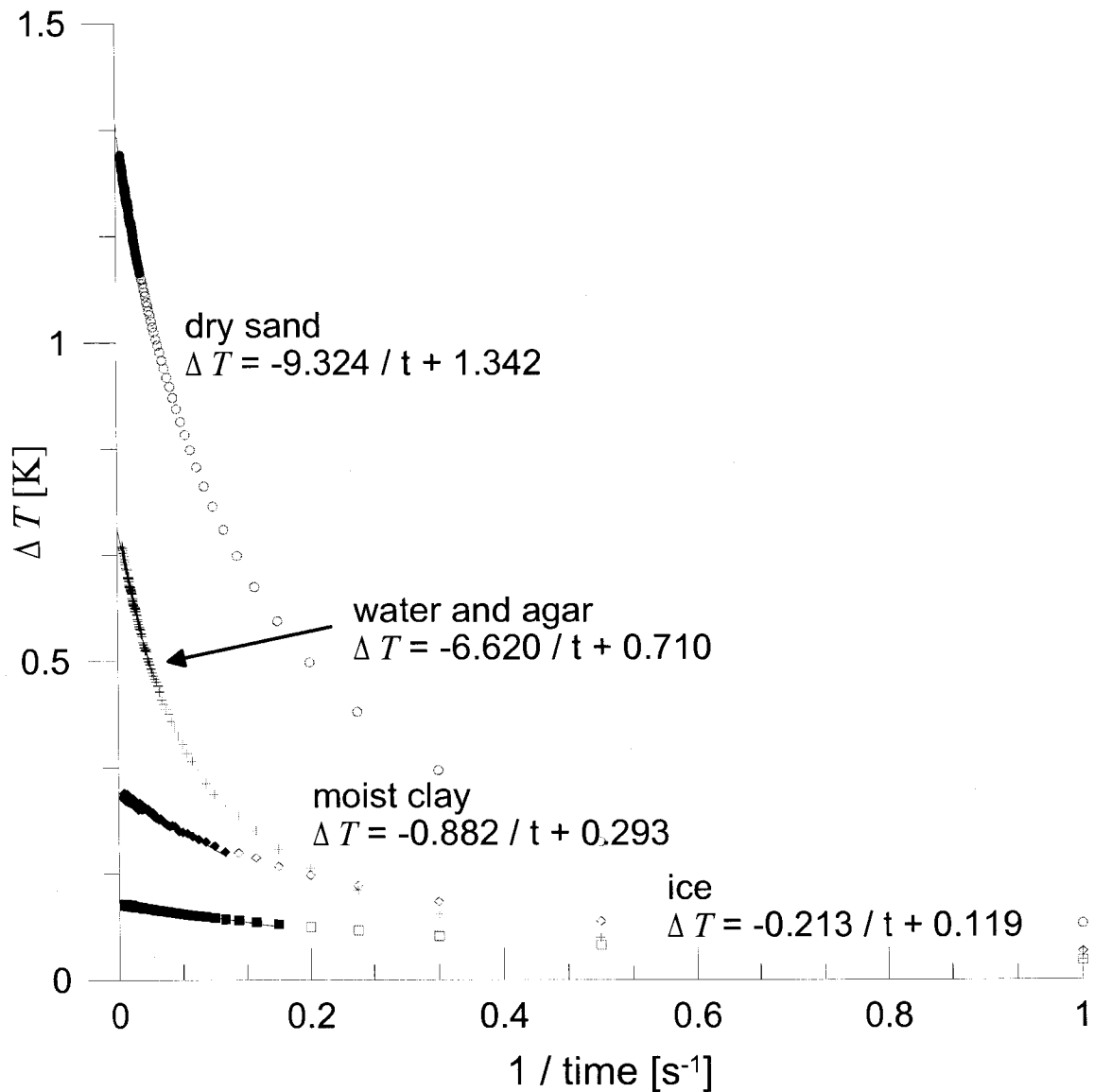
Figure 3.4. The radial temperature difference for times $t < 180$ s from Figure 3.3 is plotted here against the inverse of time. Black values are used for the least squares linear fits shown and were selected by calculating the minimum absolute change in correlation coefficient with the addition of each point. The gray points are not used in the linear fit.
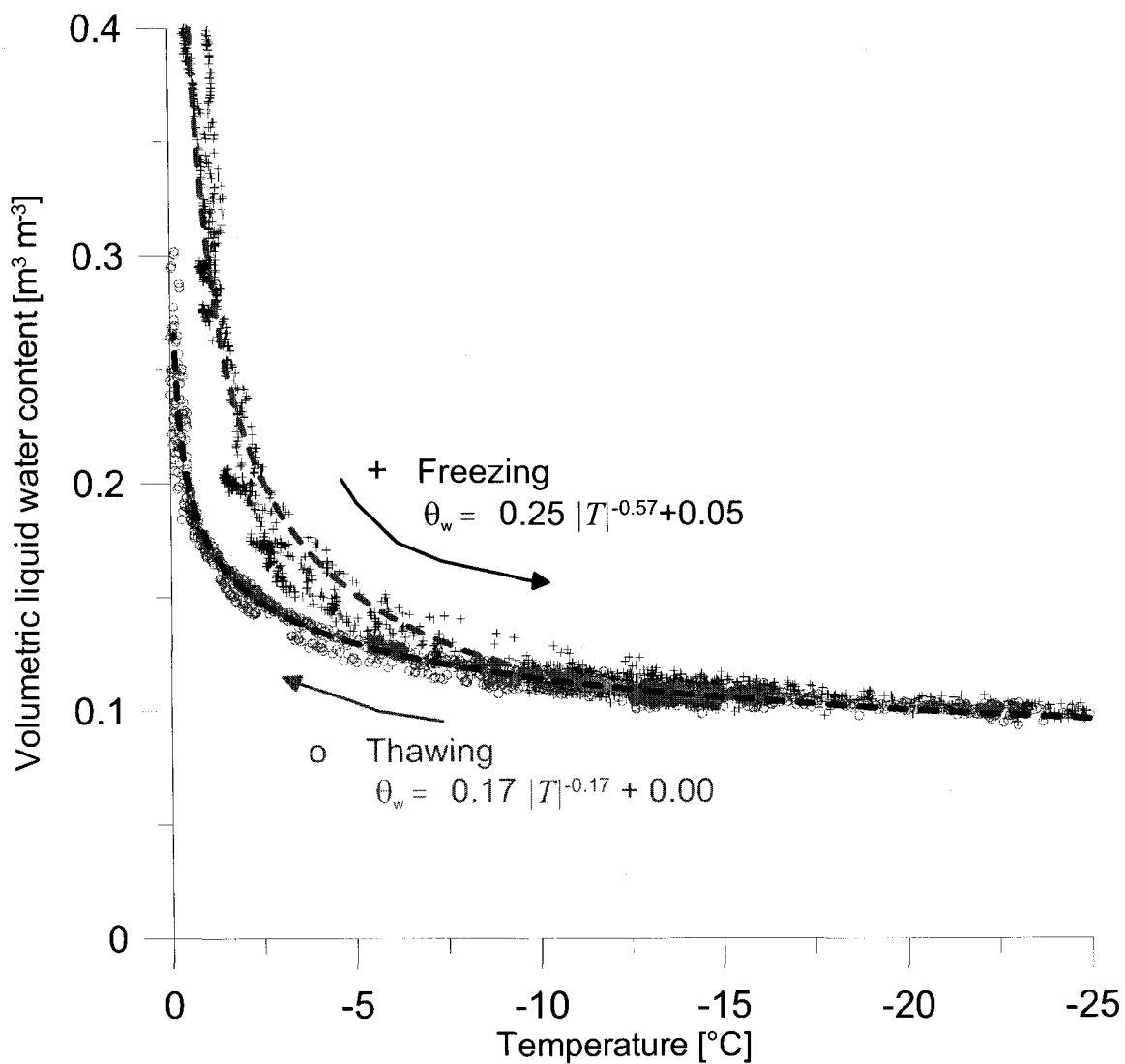
Figure 3.5. Freezing characteristic curve generated using a time domain reflectometry volumetric water content sensor and a temperature sensor proximal to the thermal conductivity sensor discussed here. Data are from a three-year period, 2002-2004, and include three freezing and thawing cycles. Least-square linear fits to the data are shown on the graph; there is no offset for the thawing curve.
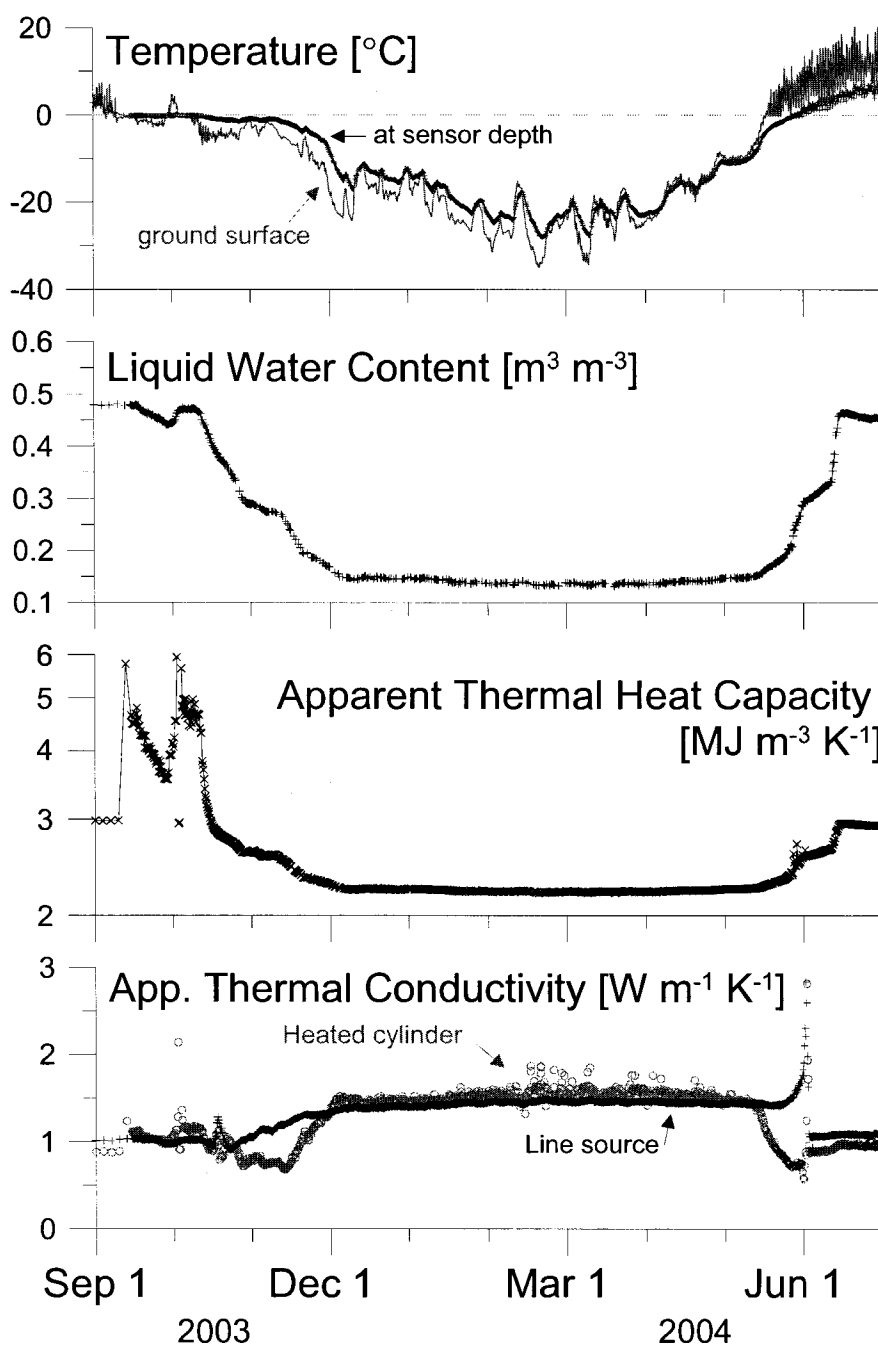
Figure 3.6. The soil temperature [°C] near the ground surface and at the thermal conductivity sensor depth (0.32 m) is shown in the top graph. Fractional volumetric water content is shown in the second graph from the top [-]. The third graph down shows apparent heat capacity, truncated to 6 MJ m^{-3} K^{-1}, calculated using equation 3.27. The lowest graph shows the apparent thermal conductivity calculated using large times approximations for the line source solution (black), and for the heated cylinder solution (grey).
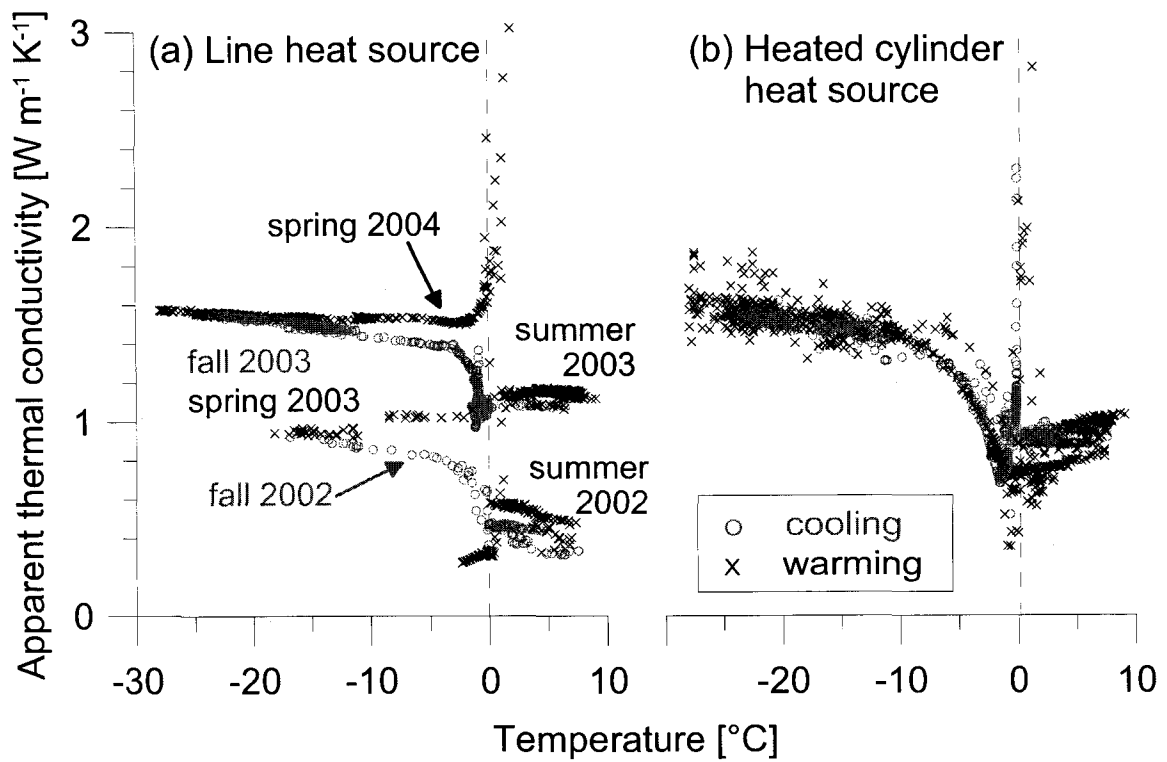
Figure 3.7. The apparent thermal conductivities (W m^{-1} K^{-1}) calculated using both the line source approximation (left) and the heated cylinder approximation (right) plotted against soil temperature (°C) from May 18, 2002 until July 21, 2004. Black crosses denote measurements made between February 1 and July 31, while grey circles indicate measurements between August 1 and January 31.

Chapter 4 - Frost boils, soil ice content and apparent thermal diffusivity[*]

Abstract

Cryoturbation in continuous permafrost regions often results in a visually striking mixing of soil horizons or materials. We are studying frost boils that formed in lacustrine sediments in the Galbraith Lake area, north of Alaska's Brooks Range, and the heat transfer and phase change dynamics that maintain these features through seasonal cycles. These frost boils are distinctly visible at the ground surface, and are silty-clay upwellings that penetrate the surrounding organic soil. Sensors were installed in a vertical plane from the frost boil's center outward to measure soil temperature, thermal diffusivity, liquid water content and thermal conductivity. The temperature field, water content and thermal properties during freezing and the concomitant changes in ice content are examined and discussed with respect to frost boil mechanics. Preliminary data suggest that ice content changes and differential snow cover dynamics are important in the maintenance of the frost boil structure over many freeze-thaw cycles.

Introduction

A frost boil is a roughly radially symmetric discontinuity in soil horizons and surface characteristics. Frost boils are often associated with sorting of soil materials based on grain size (Washburn, 1956). They can be the result of convection cell like cryoturbation, diapir formation or upwellings of lower soil horizons under pressure. Given the dependence of their distribution on climate, repeated freeze and thaw events are a factor required for their formation (Yershov, 1998). Frost boils are generally recognized at the surface by the lack or difference in vegetation. Cryoturbation subsumes material at the surface faster than pioneer species can establish themselves. In the case of plug formation or pressure upwellings, however, the unvegetated surface is the result of a change in surface characteristics that renders the environment inhospitable. Such boils can appear sorted if the upwelling soil horizon has a particle size distinct from that of the surface layers. The centers of frost boils are usually higher than their margins as a result of the upper movement of material beneath the center. The center may be higher or lower than the vegetated periphery.

Kessler et al. (2001) created a mechanical model of the spontaneous formation of sorted circles from two layers distinct in particle size. In their model, and in conceptual models mentioned elsewhere (French, 1996; Washburn, 1956), frost heave has both a vertical and horizontal component. The horizontal component in the upper horizons is directed radially outward during freezing. During subsequent thawing, however, consolidation occurs vertically. The cumulative effect over a number of freeze-thaw cycles is an

upwelling of material in the center of the boil and its subsumption at the edges. Thermal

expansion and changes in total moisture content are factors in this type of cryoturbation.

MacKay & MacKay (1976), however, concluded in their study of mud hummocks that

most mass displacement occurred not during freezing but during the summer.

Nonetheless, water migration during freezing will lead to the differences in heave

observed between the center of the frost boil and its edge. This study seeks to quantify

these differences and their influence on cryoturbation and thermal dynamics.

Methods

A frost boil in the Galbraith Lake basin (68°28.890'N, 149°28.744'W) was excavated

and instrumented in the fall of 2001, when the active layer was at a maximum thaw depth

for that year. Many frost boils exist in the area of the excavation and they share a number

of characteristics. They have developed in poorly to imperfectly drained soils on a flat

lacustrine and perhaps fluvial deposit. The frost boils are visible at the surface as roughly

circular patches of vegetation free soil, 0.2 to 1.5 m in diameter (most are 0.8 to 1.0 m),

that are cracked vertically in a columnar fashion to a depth of up to 0.2 m (Figure 4.1).

Their distribution is for the most part random, but some groups of boils lie along straight

lines extending for up to 10 m. In a few cases, these boils are not circular but oblong.

Care was taken during excavation to organize soil removed from the pit and to minimize

disturbance to the profile on restoring the excavated soil. The pit was 1.5 m deep and

transected the boil from its center to a point 1 m distant. An additional pit was excavated

2 m from the center. The frost table was encountered at 0.84 m beneath the boil and at less than 0.7 m beneath the tundra adjacent to the boil. Samples were taken from the profile and soil characteristics are discussed in Ping et al. (2003) and in Chapter 5 (Table 5.1) of this dissertation. Three sets of temperature, water content (time domain reflectometry) and non-steady state thermal probes were installed at about 0.25 m beneath the surface in a transect from the frost boil center to a point 2 m from the center and 1.5 m from its edge (Figure 4.2). The data from September 2001 until February of 2002 are presented here. Thermistors were calibrated in an ice bath and measured relative to a high precision reference resistor. Time domain reflectometry probes were calibrated using a two-point method and have a precision of +/- 0.03 $m^3 m^{-3}$. As an initial assessment of water content, Topp's equation (Topp et al., 1980) for relating soil dielectric values to water content was used. The non-steady state heat diffusion sensors consist of a 0.001 x 0.06 m heat supply mounted between thermopiles in a thin film. By measuring the response of the thermal gradient to heating, the thermal conductivity and diffusivity of the medium in which the probe is inserted can be measured. The probes have been calibrated for the range 0.3 to 4.0 W m^{-1} K^{-1}. Snow depth was measured daily less than 2m from the frost boil using a sonic distance sensor mounted on a meteorological tower. Snow depth data was corroborated via snow pits excavated at three times during the winter, in each case at and adjacent to a frost boil.

Results

Temperature

Surface temperatures at the site decreased from mean values of 5 °C in September to less than −15 °C by mid-February. Snowfall began in September and accumulated to a depth of 0.18 m over the regions surrounding the frost boils by February (Figure 4.3). Thaw depth was 0.14 m greater beneath the center of the boil than beneath the organic layer and vegetation surrounding the boil in September 2001. Freezing in the exposed mineral soil of the center was more complex than in the vegetated boundary, and characterized by frequent diurnal freeze-thaw cycles down to 0.2 m between September 12 and October 5. During this period, the temperature fluctuations at the same depth beneath the organic horizon were insufficient to cause phase change, but both profiles lost energy and became isothermal around September 19. The descent of the freezing front progressed more rapidly beneath the center of the boil.

Snow

The exposed mineral soil of the frost boil remained snow free later in the fall than the vegetated area surrounding the boil. The slight elevation of the frost boil apex above the surrounding tundra and differences in vapour transport through the soil into the snow pack resulted in differences in snow morphology as well. The frost boil is not as susceptible to wind slab formation as the surrounding tundra and snow above the boil remains thinner and less dense. By February 2002, the vegetated surface snow profile

contained a layer of wind slab underlain by hoar frost and overlain of recent snow. Over the frost boils, however, there was no identifiable wind slab, and less snow. Although no longer visible at the snow surface, the frost boils could be identified underfoot by these differences in snow character.

Moisture Content

Figures 4.4 and 4.5 show unfrozen moisture content as a function of time and temperature. The frost boil center, edge and vegetated surface layers (at depths of 0.30, 0.25, 0.25 m, respectively) had high moisture contents, indicative of near saturation, before freezing (Figure 4.4). The soil began freezing in the mineral soil on September 17 and almost a week later in the organic horizon at 0.25 m depth. Two weeks after freezing began, the unfrozen water content in the vegetated soil dropped by 0.45 and in the center of the boil by less than 0.15 $m^3 m^{-3}$. The freezing point lay between 0 and -0.05 °C for all three locations (Figure 4.5).

Thermal Properties

Effective thermal properties (conductivity and diffusivity) were measured using transient heat pulse probes during freezing. Measurements were made every three days for two weeks in early September and from December through February. Effective volumetric heat capacity was calculated based on measured thermal conductivity and diffusivity values:

$$C_{eff} = \frac{K_{eff}}{\alpha_{eff}}$$

(4.1)

where K_{eff} = effective thermal conductivity and α_{eff} = effective thermal diffusivity. The

effective volumetric heat capacity of the soil changed during freezing (from September to

December.) by 1.2, -1.2 and -1.9 x 10^5 J m^{-3} K^{-1} for the frost boil center, boundary and

tundra sensors (at depths of 0.29, 0.28 and 0.32 m), respectively (Figure 4.6),

corresponding to unfrozen water content decreases of 0.30, 0.31 and 0.52 (Figure 4.5).

Discussion

The freezing front descent in the frost boil is faster than in the vegetated area around the

boil. The shallower and later snow pack on the exposed mineral soil, and the lack of an

organic horizon, expose it to steeper temperature gradients at the surface, and the heat

flux out of the soil is greater. Temperatures fall more slowly beneath the vegetation than

beneath the frost boil. The measured thermal conductivity (Figure 4.6) of the thawed frost

boil center is much lower (at 0.3 W m^{-1} K^{-1}) than that for the vegetated soil (0.7 to 1.2

Wm^{-1} K^{-1}), so that the more rapid penetration of the freezing front beneath the boil cannot

be the result of conductive processes alone. The thawed frost boil center value is much

lower than it subsequent frozen value (around 1.3 W m^{-1} K^{-1}) and much lower than values

quoted in the literature for unfrozen silty clays (Farouki, 1981; Yershov, 1998; these

measurements are further discussed in Appendix B). The lower pre-freezing liquid water

contents in the frost boil require less latent heat removal from the soil than wetter

vegetated soils, and partially explain the difference in freezing rates. The heat capacity of the organic horizon drops with unfrozen water content (Figures 4.5 and 4.7). The vegetated temperature profile cools more rapidly above 1 m after November 1 than the frost boil profile. By the end of November, the temperature distributions at both locations are very similar (Figure 4.3).

Hinzman et al. (1991) observed effective thermal conductivity values in the range of 0.2 to 1.6 W m^{-1} K^{-1} for soils from the foothills of the Brooks Range, in dry organic soils to saturated mineral soils. Decreased temperature resulted in increases in thermal conductivity proportional to total water content. Thermal conductivity values in the frost boil center increased from 0.3 to 1.3 W m^{-1} K^{-1} (cf. Hinzman et al., 1991, who observed changes in thermal conductivity from 0.9 to 1.3 W m^{-1} K^{-1} for a saturated mineral soil). In this study, the thermal conductivity in the boundary and inter-boil soil fell during freezing, indicating either drying or a drop in ice content during this period. Goodrich (1986) recorded seasonal variations in thermal conductivity of a variety of soils, but saw changes smaller than those recorded here (maximum of 0.8 W m^{-1} K^{-1} for organic soils). He attributed differences between thermal conductivity of similar materials to differences in total moisture content. Nakano and Brown (1972) reported that effective thermal conductivities of organic and mineral soils behaved oppositely on freezing. Their frozen organic soils had higher conductivities than unfrozen by a factor of 2 to 3, whereas the mineral soils tended to decrease in conductivity on freezing. Our thermal conductivity values do not fit with any of these observations, since the thawed thermal conductivities of the mineral soil are lower than tabulated literature values. In addition, our frozen

organic soils had thermal conductivities lower than or close to their thawed values. The latter observations can be explained only by a loss of moisture from the soil during freezing, either by migration or phase change.

In this study, heat capacity is calculated from measurements made of diffusivity and thermal conductivity (equation 4.1). The thermal conductivity of soil is dependent, in a complicated fashion, on soil composition and geometry (Farouki, 1981), but heat capacity varies with composition only.:

$$\Delta C = \sum_{n=a,w,i,s} C_n \Delta \theta_n \tag{4.2}$$

where C_i = volumetric heat capacity of phase i; and θ_i = volumetric content of the same phase in the soil and subscripts a, w, i and s refer to air, water, ice and solid, respectively. Since the soil is near saturation before freezing, changes in gas volume are assumed to be negligible. We also assume that ice replaces water during phase change, with negligible changes in soil volume. Changes in ice content can then be estimated based on changes in volumetric heat capacity. Ice lens formation during freezing produces inhomogeneities in phase concentration and increases the ice content beyond that predicted by saturated liquid water content. These effects are ignored, and changes in ice content are given by:

$$\Delta \theta_i = \frac{1}{C_i} \left(\Delta C_{eff} - C_w \Delta \theta_w \right) \tag{4.3}$$

yielding changes in volumetric ice content of 0.6, 0.7 and 1.0 $m^3\,m^{-3}$ for the frost boil center, edge and vegetated region, respectively. These are larger than the porosity determined as liquid water content at saturation via time domain reflectometry. Since

water's heat capacity is more than double that of ice, phase change from liquid water to ice can be expected to decrease the effective heat capacity of the soil. The heat capacity of the frost boil center, however, increased during freezing. This increase may be an artefact of the use of Equation 4.1 and the anomalously low thermal conductivity measured in the frost boil center, and is difficult to explain physically. In general, however, the effects of snow cover, vegetation absence or presence and increases in thermal conductivity create differences in the temperature field and thermal properties between the frost boil and the surrounding soil during freezing.

Conclusions

On the basis of this preliminary physical data, the deformation of soil horizons by a frost boil results in localized changes in surface characteristics and material properties. The energy exchange at the surface is affected and the thermal dynamics of the soil change. The frost boil center freezes more quickly, thaws deeper and is subject to more diurnal freezing and thawing cycles than the surrounding vegetated soil. Differences in material properties lead to lower saturated water contents near the surface of the frost boil than adjacent to it. Changes in water content during freezing are smaller in the frost boil center than for the surrounding organic soil, and heave must be explained through lateral migration of water in the freezing soil. Despite the saturation of the soil prior to freezing, changes in thermal conductivity for soils close to 0.25 m depth are not directly related to phase change of the soil constituents. Heat capacity at 0.25 m depth in the center of the

frost boil increased during freezing, but fell at edge of the boil, following similar changes in thermal conductivity. This suggests that ice content increased substantially within the frost boil but not at its edge. These results suggest improved conditions for water movement to the freezing front exist in the frost boil center relative to its margins.

Acknowledgements

References for Chapter 4

Farouki, O. T., 1981. Thermal properties of soils. Cold Regions Research and Engineering Laboratory Monograph 81-1. Cold Regions Research and Engineering Laboratory, Hanover, NH.

French, H. M., 1996. The periglacial environment 2nd ed., Longman, White Plains, NY.

Goodrich, L. E., 1986. Field measurements of soil thermal conductivity. Canadian Geotechnical Journal. 23: 51-59.

Hinzman, L. D., Kane, D. L., Gieck, R. E. & Everett, K. R., 1991. Hydrologic and thermal properties of the active layer in the Alaskan Arctic. Cold Regions Science and Technology, 19: 95-110.

Kessler, M. A., Murray, A. B., Werner, B. T. and Hallet, B., 2001. A model for sorted circles as self-organized patterns. Journal of Geophysical Research. 106(B7): 13287-13306.

MacKay, J. R. & MacKay, D. K., 1976. Cryostatic pressures in nonsorted circles (mud Hummocks), Inuvik, Northwest Territories. Canadian Journal of Earth Sciences, 13: 889-897.

Nakano, Y. and Brown, J., 1972. Mathematical modelling and validation of the thermal regime in tundra soils, Barrow, Alaska. Arctic and Alpine Research, 4(1): 19-38.

Ping, C.-L., Michaelson, G. J., Overduin, P. P. & Stiles, C. A., 2003. Morphogenesis of Frostboils in the Galbraith Lake area, Arctic Alaska. In: Proceedings of the Eighth International Conference on Permafrost, 21–25 July 2003, Balkema Publishers, Zurich, Switzerland, pp. 897-900.

Topp, G. C., Davis, J. L., Annan, A. P., 1980. Electromagnetic determination of soil water content: Measurement in coaxial transmission lines. Water Resources Research, 16:574-582.

Washburn, A. L., 1956. Classification of patterned ground and review of suggested origins. Bulletin of the Geological Society of America. 67: 823-866.

Yershov, E. D., 1998. General Geocryology. Studies in Polar Research Cambridge University Press, Cambridge, UK.

Figure 4.1. A Galbraith Lake frost boil is shown in the upper image. The field book is 12 cm wide. Excavation bisected the frost boil and extended below the frost table (lower image). The scale shown is in cm. Segregated ice lenses are visible below 70 cm.
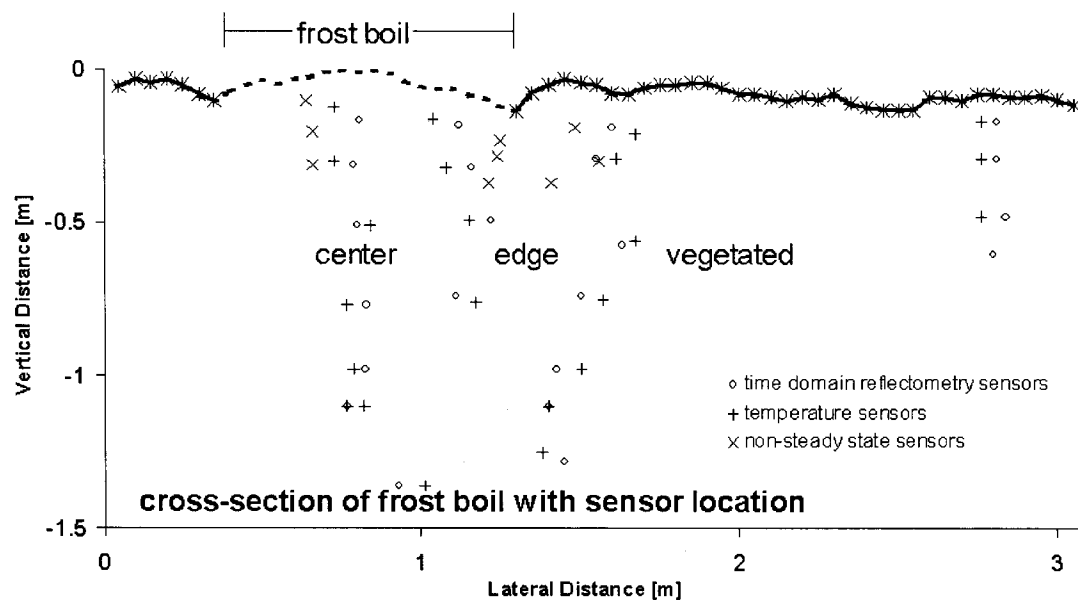
Figure 4.2. A cross-section of the instrumented frost boil with the positions of some of the instruments. The frost boil itself is indicated above and is 1 m in diameter at the surface and vegetation-free. Non-steady state sensors measure effective soil thermal properties by creating a transient heat pulse and monitoring soil temperature response.
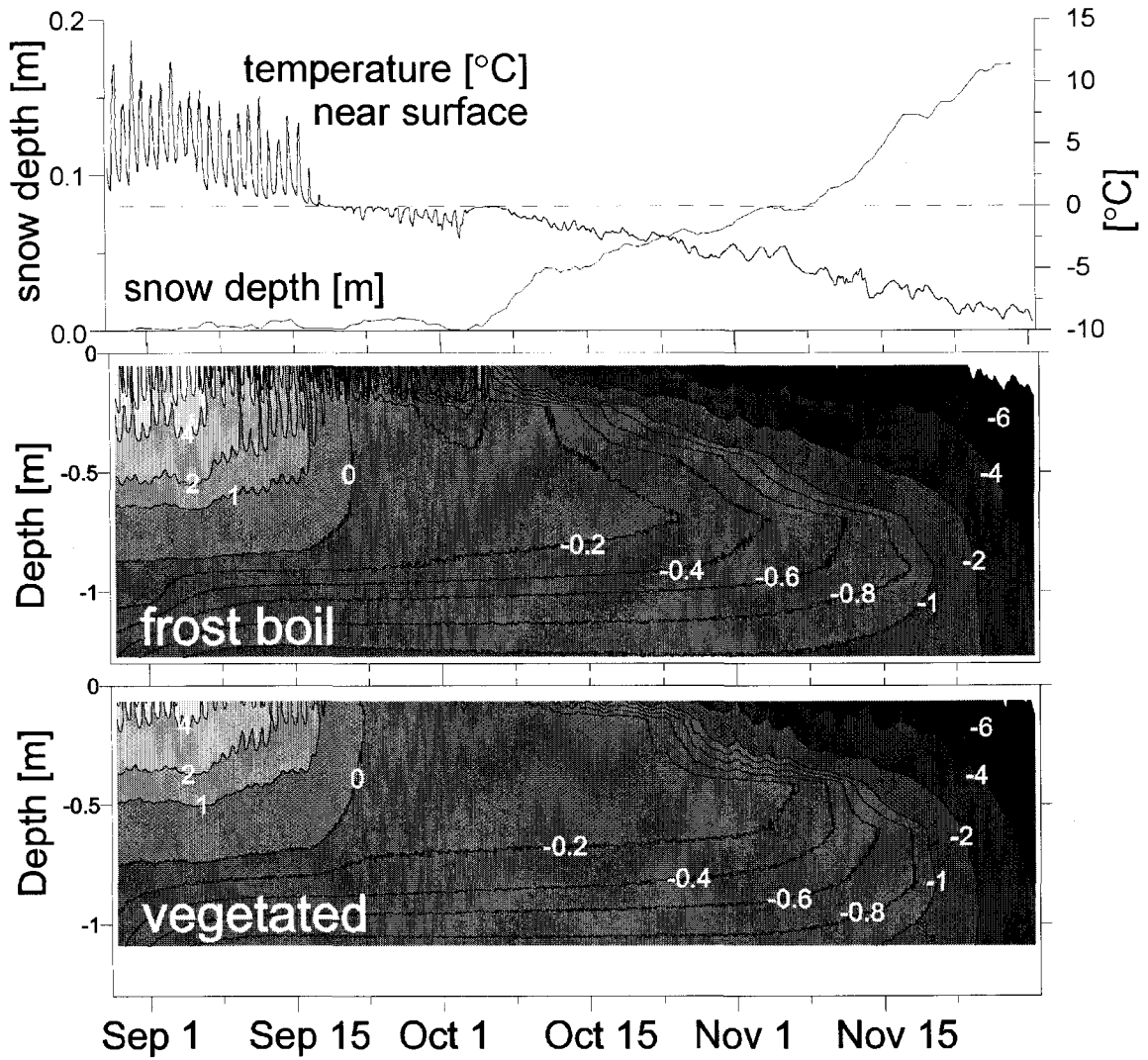
Figure 4.3. Surface temperature and snow depth in the vegetated region surrounding the frost boil are shown in the top graph. The temperature fields are for the frost boil center and the vegetated profile adjacent to the frost boil.
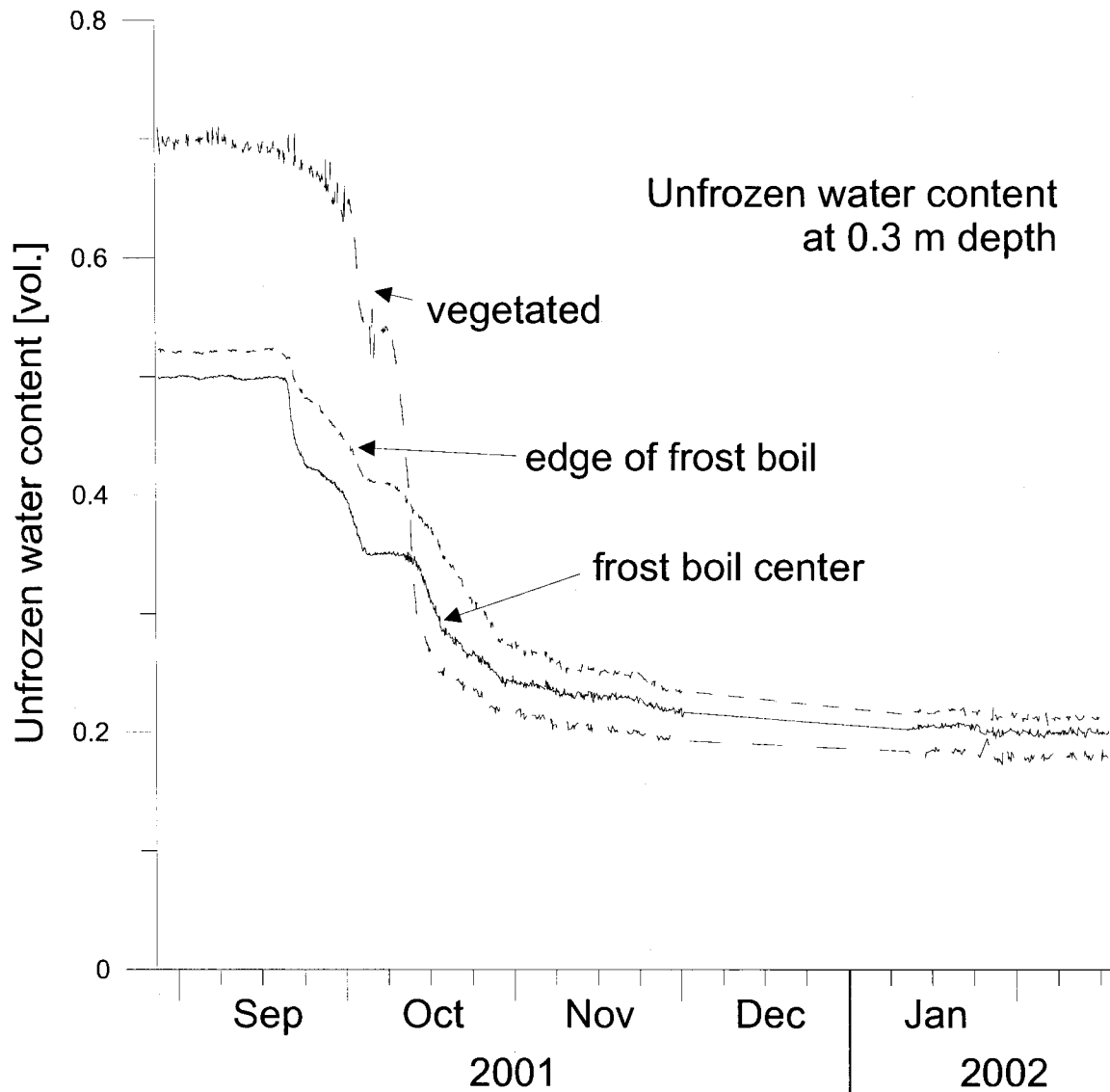
Figure 4.4. Decrease in unfrozen water content associated with fall freezing for three sensors at 0.30, 0.25 and 0.25 m depth, at the frost boil center, edge and at 1.3 m from its center, respectively.
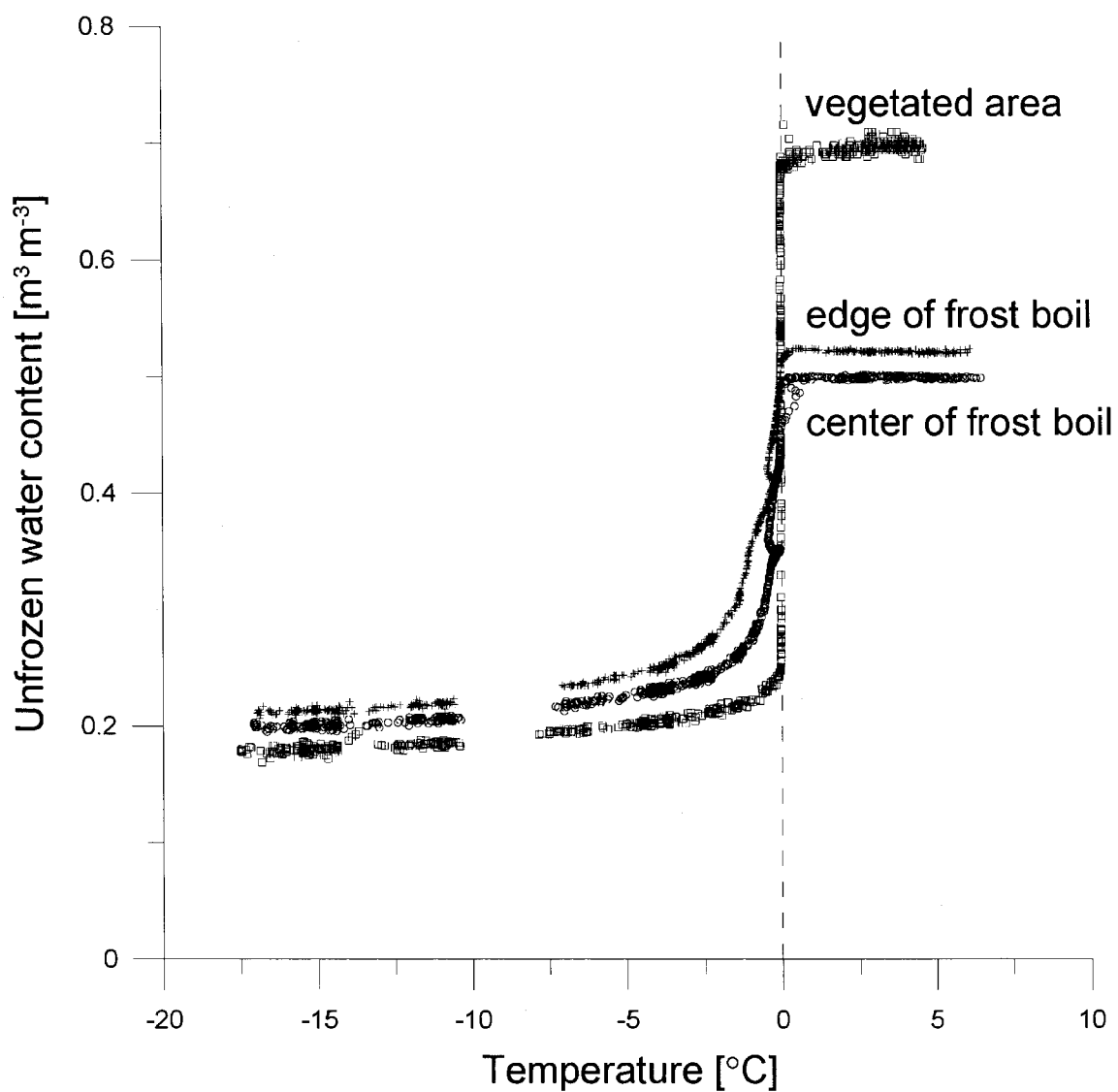
Figure 4.5. Freezing characteristic curves for the same locations as in Figure 4.3. The stable water contents above 0 °C reflect saturated moisture levels before freezing.
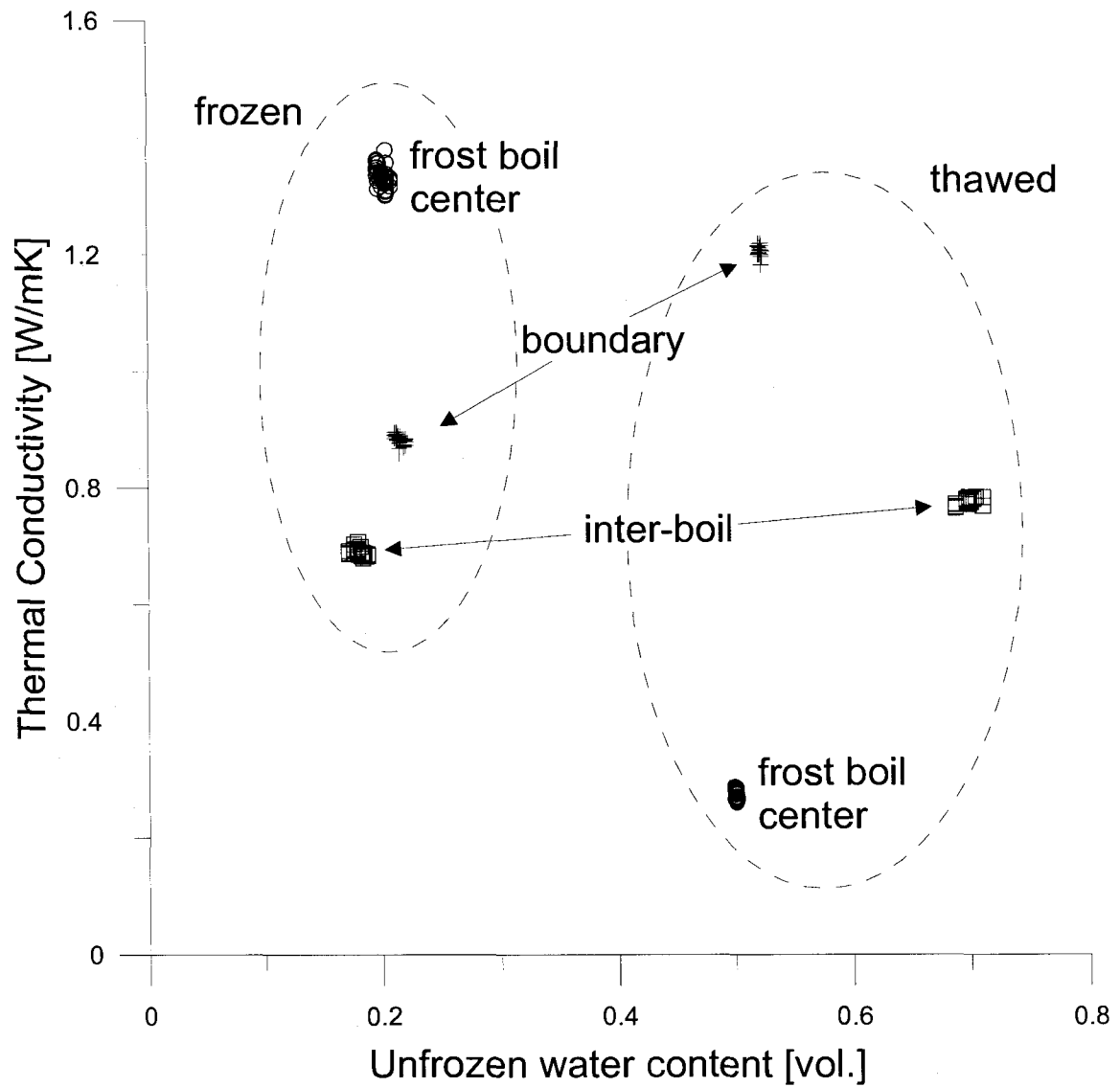
Figure 4.6. Thermal conductivity values before (September 2001) and after (December to February 2002) freezing measured at depths of 0.29, 0.28 and 0.32 m beneath the frost boil center, edge and 1.3 m from its center. The frost boil center's mineral soil increases in conductivity during freezing.
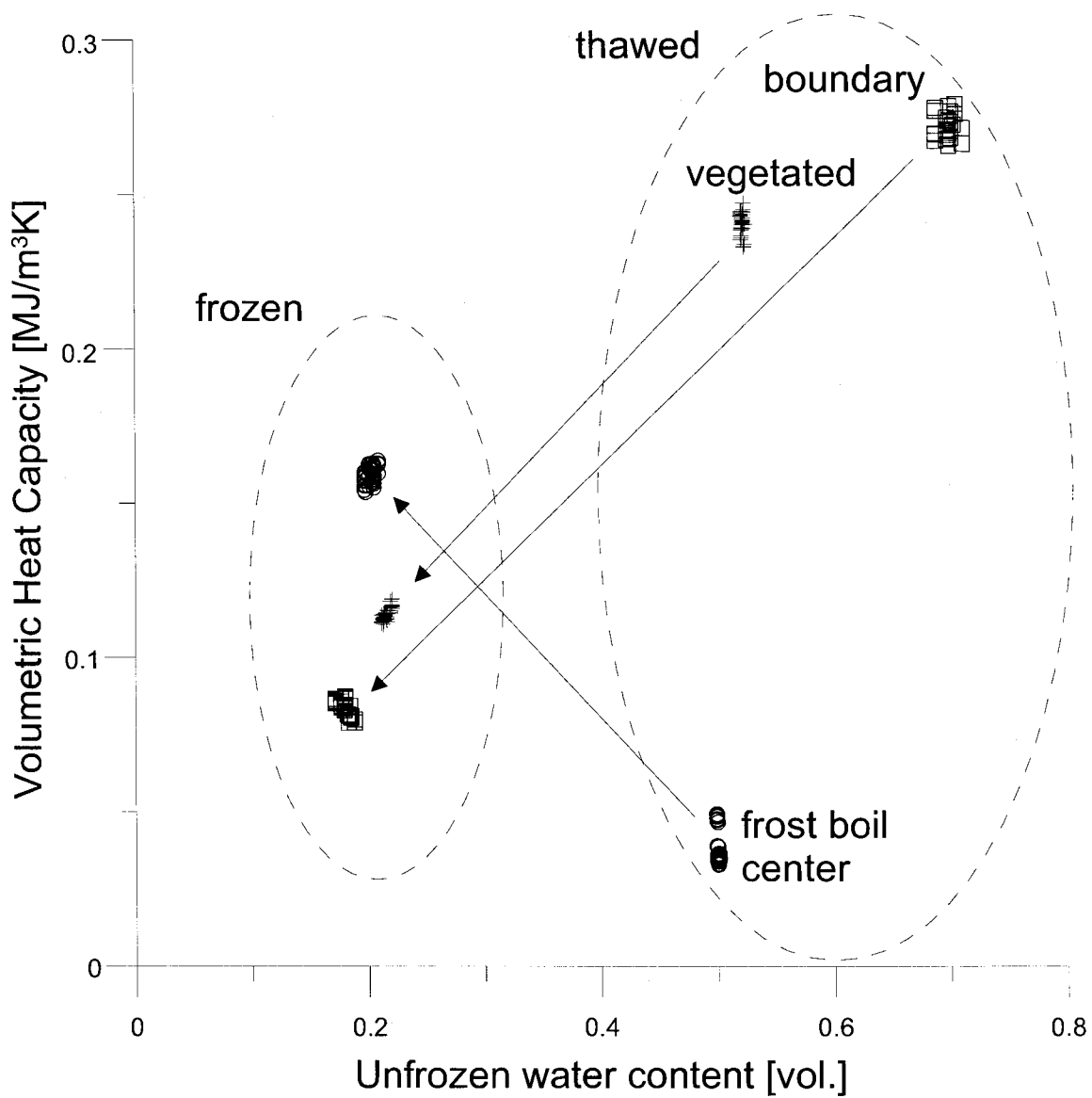
Figure 4.7. Volumetric heat capacity values calculated from measured thermal conductivity and diffusivity values.

Chapter 5 - Ice content and frost boils: Field observations[*]

Abstract

Frost boils at Galbraith Lake in the northern foothills of the Brooks Range of Alaska are a conundrum of periglacial geomorphology, appearing at the surface to result from convection cell-like movement of soil material but with no evidence of cyclic soil movement in sub-surface soil horizons. Our aim is to measure and explain the seasonal changes in soil ice content in these frost boils. Soil samples were collected from an excavated frost boil, and instruments were installed to monitor changes in the soil. Ground surface position was measured over a three-year period. By comparing the subsidence and thaw rates, we calculate the soil ice content as a function of depth. This data is compared to bulk thermal diffusivity data. The frost boils heave during freezing and settle during thaw while the surrounding tundra heaves negligibly. For these frost boils, ice distribution over depth depends on winter conditions rather than on freezing rate. The low interannual variability in heave suggests that the frost boils are stable features. We distinguish between near-surface segregated ice that may disappear depending on winter conditions, and segregated ice that forms at the last depth to freeze in the fall.

---

[*] submitted as: Overduin, P. P., Kane, D. L., 2005. *Ice content and frost boils: Field Observations.* Permafrost and Periglacial Processes.

Introduction

The formation of ice in soil lies at the heart of many processes unique to permafrost regions. Changes in ice content during freezing and thawing drive differential heave and the formation of patterned ground.

The damping effect of the release of latent heat of fusion due to penetration of the freezing front leads to soil conditions favourable to microbial activity long after the world above the ground surface has frozen solid. The formation of ice can act as a seal on the unfrozen active layer, creating peculiar redox (Overduin and Young, 1997) and pressure environments (Oechel et al., 1993). In their study of solifluction, Harris and Smith (2003) shows that increasing soil ice content decreases the effective stress, leading to plastic flow of the soil, primarily during freezing.

Frost heave is a common phenomenon in some soils subject to seasonal freezing and thawing. Ice is less dense than water, resulting in soil expansion due to freezing of liquid water. How much water freezes depends on the soil characteristics. Moisture migration during freezing can lead to additional expansion of the soil. In freezing soils, water moves towards the freezing front following the local temperature gradient. The segregation of ice in the freezing soil results in additional heave referred to as the secondary mode of heave (O'Neill and Miller, 1985). Taber (1929) showed that secondary frost heave also occurred for substances with higher solid phase density, and it has since been demonstrated for such materials as argon (Zhu et al., 2000) and helium (Mizusaki and Hiroi, 1995). Rempel et al. (2004) present a model of frost heave showing

that liquid water exists at cryotic temperature as a result of curved boundaries between phases and because of long-range intermolecular forces. The latter create the suction required to bring moisture to the freezing front for ice segregation by virtue of their inverse variance with temperature. Heave is permitted when the combined maximum frost-heaving pressure and hydraulic pressure exceed the overburden pressure (Wettlaufer and Worster, in review). Frost heave is therefore dependent on the rate of freezing and the overburden pressure. Both are related to the character of the soil, which may change over short spatial scales, both vertically and horizontally. The differential heave that results from lateral changes in soil character is invoked as the main mechanism for formation of a landform common in periglacial environments, the frost boil.

This study focuses on frost boils located at Galbraith Lake, in the northern foothills of the Brooks Range of Alaska. Vliet-Lanoë (1991) reviewed the plausible mechanisms of formation of frost-boils. Of the 19 mechanisms originally proposed by Washburn (1956), two mechanisms emerged as the most plausible: convection-cell like cryoturbation and load casting. Recent support for the former mechanism came in the form of a simulation of the creation of sorted circles, stripes and polygons based on the sorting of material by grain-size in the presence of an inclined frost table (Kessler and Werner, 2003). Heave acts normal to the frost front, so that an inclined frost front moves soil material in a direction with a lateral component. Subsidence occurring during thaw is assumed to act vertically, resulting in a net lateral displacement and convection-cell like movement of material over multiple freeze-thaw cycles. The regular size and spacing of most frost boils result from appropriate parameter choices in their model (Kessler and Werner,

2003). Walker et al. (2004) mention numerous mechanisms, including frost cracking, heave, mass displacement and sorting, at work in the creation of the frost boils they study in northern Alaska and arctic Canada.

Based on the observed soil horizon morphology at Galbraith Lake, however, Ping et al. (2003) suggested that their genesis was probably linked to a single extrusion of lower soil horizons through structural weaknesses in the overlying horizons, for example through frost cracks. The vegetation-free frost boil center, on the other hand, suggests that outward spreading of the exposed mineral material is actively occurring and there are roots that have been exposed at the surface and stretched by soil movement. No subsumed organic material beneath the frost boil boundaries was found, however. The role of differential frost heave in creating and maintaining these features is unclear; what additional processes are involved if differential frost heave is not responsible for their formation is also unclear. Based on Vliet-Lanoë's (1991) analysis, however, it is clear that ice dynamics play a central role in the formation and maintenance of these periglacial features.

Measuring the volumetric ice content in the soil is not trivial, however, even by destructive sampling methods. It is further complicated by the fact that ice segregation in the active layer and upper permafrost can lead to highly variable spatial concentrations of ice at a variety of scales. Methods that have been used for ice content include: gravimetric; radar, either as ground-based or remote techniques; acoustics; neutron absorption for the determination of total water content; dielectric methods (Bittelli et al., 2003) and volumetric methods. We use the changes in volume and thermal properties

during freezing to infer changes in ice volume. Our objectives are to describe the heave dynamics of a field of frost-boils and to quantify the role of seasonal ice dynamics in these features and evaluate the role of ice formation and segregation in differential frost heave at this site.

Methods

Site

Galbraith Lake is about 3 km long located at the west end of Atigun Gorge on the north side of the Brooks Range, Alaska (68°28.890'N, 149°28.744'W). Water enters the lake through a tributary at its northern end and through an alluvial fan that forms its western shore. It drains into the Sagavnirktok River, which flows across the North Slope of Alaska into the Arctic Ocean. Aerial photographs show evidence of a series of old shorelines beyond the northern end of the lake. Within this region of exposed and reworked lake bed, a mixture of lacustrine and fluvially deposited sediments form a flat basin between outwash fans of streams into the valley from the west, and bluffs on the east. At present, there is a small airstrip located on the west side of the plain. The Dalton highway and the Trans-Alaska Pipeline run north to south along the east side of the valley. The site is poorly drained and the water table is within 20 cm of the ground surface during the growing season. Land-cover type is classified as moist non-acidic tundra. The frost boil soil is classified as Aquic Haploturbels and in the surrounding

tundra as Histic Aquorthels according to the soil taxonomy (Soil Survey Staff, 2005). In the frost boils, the soil horizons are contorted by cryoturbation but in the tundra, the soil horizons are flat (Ping et al., 2003). Permafrost temperatures at 20 m are about –5 °C (Osterkamp, 2003).

Visual and near infrared band images of the site were collected using the Bi-camera Observation Blimp (BOB) low-altitude aerial photography system (Harris, 2005). Ground features were used to georectify the images, which have a resolution of better than 0.07 m. The site is shown (Figure 5.1) in a normalized difference image of the reflected near infrared and red bands. The only features devoid of vegetation in the field of view are the frost boils, water surfaces and some humans, which appear darker than the vegetated surfaces.

Instruments

Installation of sensors followed careful excavation of a soil pit roughly bisecting a frost boil. Soil was removed by horizon with consideration for the three-dimensional structure of the horizons, and replaced and compacted to original bulk density. Sensors were installed in the soil pit wall between the surface of the soil and 1.36 m depth (Figure 5.2). Temperatures were measured hourly using a vertical array of thermistors. The thermistors were calibrated using a de-ionized water-ice mixture, from which a thermistor-specific offset, δ_o, for the Steinhardt-Hart equation was generated:

$$T^{-1} = 1.28 \times 10^{-3} + 2.37 \times 10^{-4} \left(\ln\left(R_T - \delta_o \right) \right) + 9.06 \times 10^{-8} \left(\ln\left(R_T - \delta_o \right) \right)^3 \tag{5.1}$$

where R_T is the measured resistance and δ_o is the resistance offset at 0 °C.

Time domain reflectometry sensors (Campbell Scientific CS605) connected to a

reflectometer and datalogger (Campbell Scientific TDR100 and CR10X) were used to

record the apparent sensor length at one-hour intervals. In addition, the entire reflected

waveform for each sensor was measured once per week. These waveforms were used to

verify the TDR100 waveform analysis algorithm, and to provide an alternate time series.

The TDR100 algorithm sometimes failed during phase change and in the frozen soil,

associated with temperature-induced changes in the cable length. This problem was

solved by trial and error determination of two cable lengths in the datalogger program,

one for thawed soil and one for frozen soils. The sensors had been previously calibrated

in the laboratory using water and air as reference materials following the method of

Heimovaara et al. (1995). The bulk relative dielectric permittivity data was used to

calculate liquid water content using Roth et al.'s (1990) mixing model for mineral

horizons and an empirical relationship for organic horizons (Overduin et al., 2005). The

accuracy of the method is estimated to be better than 0.05 m^3 m^{-3} (Heimovaara et al.,

1995).

Thermal diffusivity is calculated as the ratio of thermal conductivity and heat capacity:

$$D = \frac{k}{\rho C} \qquad (5.2)$$

where D, k, ρ and C are the bulk thermal diffusivity, conductivity, density and heat

capacities of the soil, respectively. Thermal conductivity was measured using Hukseflux

TP01 transient heat pulse sensor installed at 0.1 and 0.2 m depth beneath the center of the

frost boil. The radial temperature difference following heating for 180 s was measured

and analyzed following Overduin et al. (in review). Thermal diffusivity was calculated from measured thermal conductivity values and from calculated volumetric heat capacity. Volumetric heat capacity is calculated from measured soil composition. The dependence of the bulk heat capacity on composition is the volumetric fraction-weighted arithmetic mean of the soil components:

$$\rho C = \sum_{n=a,i,w,s} \rho_n C_n \theta_n \tag{5.3}$$

where ρ is the soil bulk density, and ρ_n is the density, C_n the heat capacity by mass, and θ_n the volumetric fraction of soil component n. The subscripts refer to air (a), ice (i), water (w) and soil (s). The volumetric heat capacities of ice, water and soil that result are 1.93, 4.18, and 1.88 MJ m^{-3} K^{-1}, respectively, while that of air was neglected. The volumetric liquid water content was taken from the TDR measurements, and ice content was estimated as the difference between pre-freeze fall liquid water content and the measured volumetric liquid water content in the frozen soil. This method implicitly assumes that water migration during and after freezing is negligible, probably not a valid assumption for frost boils, in which freezing can occur over a long period (> 2 months) of time. The heat capacity is linearly dependent on estimates in soil component fractions, however, and the thermal diffusivity is thus less sensitive to changes in heat capacity than in thermal conductivity.

Thaw depth

Thaw depth is estimated using the depth of the TDR sensors and the timing of phase change at each sensor. Phase change is identified as the point of inflection in the time series of soil liquid water content, which gives a more precise indication of phase change temporally than temperature changes, which are attenuated by latent heat release, particularly in the fall. To interpolate between sensor depths, these data were fit to the solution to the Stefan problem:

$$z = A\sqrt{t_d \sum \left| \overline{T} - T_f \right|} + B \tag{5.4}$$

where t_d is the number of seconds per day, T is the mean daily temperature of the ith day since the initiation of thawing or freezing, T_f is the freezing point and A and B are constants. The term within the square root is referred to as the degree-days of freezing or thawing (Yershov, 1990). The coefficients A and B are specific to a freeze or thaw season, and were used to predict thaw based on air temperatures. They also change substantially from site to site, but only the frost boil center is considered here.

Frost heave

By comparing soil volumes in the thawed and frozen states, changes in the volumetric fractions of water and ice may be inferred. Heave was measured in two ways. For the excavated site, fibreglass rods 1.22 m long and 3 mm in diameter were anchored in the permafrost at depths between 0.7 and 1 m and extended vertically above the ground surface. The rods were distributed in a line from the approximate center of the frost boil

to a point 2.47 m away (Figure 5.2). Small metal washers were free to slide along the rods and rested on the ground surface. The rod length exposed above the metal washer was measured at irregular intervals throughout the year. At a second frost boil, five ultrasonic distance sensors were mounted on a horizontal rod supported by two vertical members, which were anchored in the permafrost at a depth of over 1.5 m and encased in tubing that extended over the active layer depth. The sensors have a resolution of 0.1 mm and an accuracy of +/-0.01 m. The sensors record the signal from the nearest target in their approximately 22° field of view. They are thus affected by the presence of snow and vegetation. The values used here are from the vegetation-free frost boil during snow-free periods only.

Following the suggestions by Burn (1998), we define the active layer depth as the penetration depth of the 0 °C Celsius isotherm. To calculate the rate of thawing in spring, the position of the 0 °C isotherm from sensors at 0.12 to 1.36 m was linearly interpolated over depth and time from temperature data. We assume that daily subsidence at the surface is due to daily ice melting at the thaw front and that sensor position relative to the surface changes negligibly with time. Although uncertainty in settling rates over short time scales is high, the correspondence between the rates of subsidence and thaw suggests that our assumption is reasonable. We define the vertical positions of the ground surface $z_0(t)$, and the phase change boundary, $z_{ft}(t)$, relative the ground surface at the start of thawing or freezing. Settling is ascribed to the melting of ice in the soil to the depth z_{ft}. Accounting for the difference in ice and water densities, the mean segregated ice content over the profile from z_0 to z_{ft} before thawing is then given by:

$$\theta_i'' = \frac{\Delta z_0}{\Delta z_{ft}} - \theta_w \frac{\rho_w}{\rho_i} \frac{\Delta z_{ft} - \Delta z_0}{\Delta z_{ft}} \tag{5.5}$$

where $\rho_w = 917.0$ kg m^{-3} and $\rho_i = 999.8$ kg m^{-3} for the densities of water and ice, respectively. We assume that the bowl-shaped depression in the frost table beneath the frost boil and the low hydraulic conductivity of the soil limit drainage of water from the soil volume after thawing.

Volumetric latent heat production

Changes in ice content can also be inferred from latent heat production and consumption in the frozen ground (Roth and Boike, 2001). Conservation of energy and Fourier's law lead to the heat diffusion equation in one dimension:

$$\frac{\partial}{\partial t}(\rho C T) = r_h + \frac{\partial}{\partial z}\left(k\frac{\partial T}{\partial z}\right) \tag{5.6}$$

where r_h is the heat production or consumption per unit volume. The temperature distribution in the soil is used to estimate the heat production or consumption in the soil by integrating over each soil layer between sensors at depths z and z^+, and between observation time steps t and t^+, where the +-sign denotes subsequency:

$$
\begin{aligned}
r_{est} &= \frac{1}{(z^+ - z)(t^+ - t)} \int_z^{z^+} \int_t^{t^+} r_h(t,z)\, dt\, dz \\
&= \frac{1}{(z^+ - z)(t^+ - t)}\left[\rho C \int_z^{z^+} T(t^+,z) - T(t,z)\, dz - k \int_t^{t^+} \frac{\partial T(t,z^+)}{\partial z} - \frac{\partial T(t,z)}{\partial z}\, dt\right]
\end{aligned} \tag{5.7}
$$

Integrals are approximated using the trapezoidal rule and the partial derivative of temperature is estimated using a central finite difference. A constant value for ρC is

applied (2×10^6 J m^{-3} K^{-1}) following Roth and Boike (2001), and a time-independent k value is calculated using equation 5.2 and the thermal diffusivity for each soil layer (described in the next section).

Using temperature to estimate thermal diffusivity

Estimations of the thermal diffusivity (D) of the profile are based on the propagation of near-surface soil temperatures during the winter using a solution to the diffusion equation in a one-dimensional, homogeneous medium with no internal heat sources (Carslaw and Jaeger, 1990, Chapter II, Section 2.5). The convolution integral gives the temperature of a semi-infinite medium with initial temperature zero as:

$$T(z,t) = \int T(0,\tau) f_\tau(t-\tau,z) d\tau \tag{5.8}$$

where

$$f_\tau(t,z) = \frac{z}{2\sqrt{\pi D t^3}} e^{-z^2/4Dt} \tag{5.9}$$

Using this solution, Roth and Boike (2001) demonstrated that temperatures throughout the active layer during the frozen state can be accurately predicted from measured temperatures at shallow depths. Following suggestions in Carslaw and Jaeger (1990), we use this solution in an inverse sense to fit a mean apparent thermal diffusivity to the soil profile between the shallowest temperature sensor and each temperature sensor depth. The shallowest measured soil temperature is propagated downwards using two parameters as fitting constants: the bulk thermal diffusivity of the soil, which is assumed to be invariant with depth between the shallowest sensor and deeper sensors; and a

temperature offset that accounts for differences in initial conditions between the shallow sensor and deeper sensor. Fitting is optimized in a least squares sense.

These estimates are valid only under the assumption that heat transfer is conductive and yield integrated values for the soil profile between a near-surface temperature sensor and the depth to which the signal is propagated. The soil is saturated at the time of freezing, and we restrict estimation to the cold winter period, after the zero curtain has been lifted. Conductive heat transfer is the dominant mode of heat transfer and latent heat effects are likely to be small.

For each sensor depth, an estimate of the thermal diffusivity, $\underline{D}_j$, of the soil profile between the sensor at depth z_j and the shallowest sensor is obtained. We assume that the apparent thermal diffusivity of the profile is the arithmetic mean of the diffusivities of the individual layers, which is reasonable for the center of the frost boil, where soil horizons are parallel to the ground surface. The influence of the horizon interfaces is unlikely to be important since there is little physical difference between soil layers. This leads to:

$$\underline{D}_j = \sum_{k=2}^{j} D_k \frac{z_k - z_{k-1}}{z_j} \tag{5.10}$$

where $\underline{D}_j$ is the profile apparent thermal diffusivity from the shallowest sensor (z_1) to the jth sensor, and D_k is the diffusivity for the layer from depth z_{k-1} to z_k. Given j values for the layers beneath the uppermost temperature sensor ($k = 1$), the diffusivity for the jth individual layer can be calculated from the series of values above it:

$$D_j = \left(\frac{1}{z_j - z_{j-1}}\right)\left(\underline{D}_j z_j - \sum_{k=2}^{j-1} D_k (z_k - z_{k-1})\right) \tag{5.11}$$

The spatial resolution is limited by the spacing of the temperature sensors, and because we use the shallowest temperature sensor to propagate the temperature signal, the thermal diffusivity of the soil between the ground surface and the shallowest sensor is not estimated.

Results and Discussions

Frost boil morphology

Frost boils at Galbraith Lake are identified at the ground surface as roughly circular areas free of vegetation and between 0.5 and 1.5 m in diameter. In some cases, several frost boils appear to have developed close enough to one another to form linear regions of frost boils up to 3 m long. The vegetation cover of the surrounding tundra is complete, and the frost boils thus have well-defined boundaries (Figure 5.1, inset). Based on the positions of 110 frost boils identified in Figure 5.1 (C), the mean distance between frost boil centers is 5.6 ± 0.6 m. They are not uniformly distributed, as the terrain is also the site of other periglacial features, including ice-cored mounds (A), thermokarst ponds (B) and ice wedges (D), that are found throughout the image. Dark spots just below and to the right of the upper ice mound (A) are people, and a 1 m quadrant can be identified. Frost boils are also found in the surrounding tundra, outside of the old lake bed region, but tend to be covered with vegetation to some degree, and are smaller with less distinct boundaries.

The Galbraith Lake frost boils appear to have undergone sorting, with silty-clay mineral material in the frost boil center and sandy soil underlying the vegetated margins and surrounding tundra of the boils. The surfaces of the frost boils are cracked in a columnar structure, and a crust has developed. They are slightly domed, and their elevation relative to the surrounding tundra varies with the time of year, which is examined in the section on frost heave, below. Ping et al. (2003) concluded that the soil profile morphology showed extrusion of clayey material from below into a surrounding sandy matrix, creating a textural differentiation between soils under the tundra and within the frost boil. Beneath the center of the frost boil there is little change in soil composition with depth. All sampled horizons were mineral with organic contents of less than 3% by weight, had bulk densities in the range of 1.62 to 1.76 g cm^{-3} and saturated soil-paste pHs of 8 to 8.2 (Table 5.1). Little difference was observed in soil texture variation with depth, down to 0.73 m. The soil pit was excavated to a depth of 1.3 m and the frost table beneath the center of the frost boil was encountered at 0.73 m. The thaw depth below the frost boil exceeded the thaw depth immediately adjacent to and at a distance of 2.5 m from the boil by over 0.22 m. Many ice lenses were encountered between 0.75 to 0.83 m, running parallel to the frost table and containing ice lenses up to 7 mm thick. They were angled upwards below the margin of the frost boil and not found beneath the adjacent tundra, which has a 0.05 to 0.20 m organic horizon at the surface. Below 0.83 m, ice layers of 0.02 to 0.05 m thickness were separated by thin soil layers. This ice was associated with the transition zone, the layer of soil that is usually permafrost, but is subject to infrequent

thaw during warm years. Cores were drilled into the ice layers at the bottom of the pit, which continued downwards for at least another 0.3 m below the profile.

Rates of freezing and thawing

Soil temperature and volumetric liquid water content for three hydrologic years show differences between the three winter periods (Figure 5.3). Freezing during 2001 and 2003 was rapid compared to 2002, changing from negative to positive temperatures throughout the soil profile over about 2 days (September 19-21, 2001 and September 9-11, 2003). Between 0.17 and 0.77 m, the mean freezing rates (calculated using the position of the 0 °C isotherm) in 2001, 2002 and 2003 were 7.2×10^{-1}, 1.2×10^{-2} and 2.1×10^{-1} m d^{-1}, respectively. Although the freezing rate is more rapid in 2001, it occurs ten days earlier than in 2003. The freezing rate during the fall of 2002 is more than an order of magnitude lower than in the preceding and following year and the active layer at 0.77 m depth remains unfrozen until after November 20. During the springs of 2002 and 2004, the profile thawed down to 0.12 m by May 15th. In 2003, however, thaw reaches this depth more than 2 weeks later, a reflection of differences in degree-days of thawing, which by July 18 totalled 684 °C·d in 2004 but only 469 °C·d in 2003, with thaw depths of 0.88 and 0.78 m, respectively.

For the springs of 2003 and 2004, interpolated thaw depth data are shown in Figure 5.4, along with air temperature, the timing of phase change at each TDR sensor and the position of the ground surface (automated subsidence data is not available for the spring of 2002). The ground surface and interpolated thaw depth positions are shown relative to

the permafrost. In both years, the correlation coefficient between the Stefan solution and the observed phase change was better than $R^2 = 0.99$, with coefficients $\{A, B\}$ in equation 5.4 of $\{-3.76 \times 10^{-2}, 2.64 \times 10^{-2}\}$ and $\{-3.30 \times 10^{-2}, -1.58 \times 10^{-2}\}$ for 2003 and 2004, respectively. The spring subsidence in both years was similar in timing and magnitude (Figure 5.4) and reached 2 cm and 2.2 cm by July 18 in 2003 and 2004, respectively. On Oct 1, 2002, over 0.16 m of snow accumulated (upper graph in Figure 5.5). As a result of subsequent events, the snow pack grew to 0.25 m thickness without diminishing over the course of the winter. During the following winter, snow fell between Sep 6 and Sep 26, 2003, but had disappeared from the frost boil surface by October 1, 2003. Subsequent snow covers that exceeded 0.02 m lasted for less than 20 days. We conclude that the major factor in determining the rate of freezing was the presence, thickness and duration of the snow pack. These differences led to soil temperatures colder by 5 to 20 °C for most of the winter of 2003/04 than the previous winter.

Bulk soil thermal diffusivity

Thermal diffusivities based on measured thermal conductivities yielded winter values of around 4.5 and 6 x 10^{-7} $m^2 s^{-1}$ for 2002/03 and 2003/04, respectively, at 0.2 m depth (Figure 5.5, bottom graph). Bulk thermal diffusivity values from the soil at 0.1 and 0.2 m reveal seasonal changes for both depths, with distinct thawed and frozen values. In general, the shallower soil has a lower thermal diffusivity, and smaller seasonal amplitude; these are reflections of lower water and ice contents at this depth. In the spring of 2003, snow melt infiltration and refreeze results in an increase in ice content and

thermal diffusivity at 0.1 m (Figure 5.5, middle graph). This does not occur in the following spring (2004), because the frost boil is snow-free before melt occurs. The higher moisture and ice contents at 0.2 m result in larger seasonal fluctuations in bulk thermal diffusivity.

In addition to temporal series of measured thermal diffusivity, estimates of thermal diffusivity for the soil layer between each temperature sensor and the shallowest measured soil temperature are made (Figure 5.6, left graph). Inferences can be made regarding the soil composition only if the variation in thermal diffusivity with soil composition is appropriately parameterized. The bulk thermal conductivity depends on the volumetric fractions of the soil components, their thermal conductivities and on the geometry of their arrangement (Johansen 1977). Farouki (1981) in his survey of models for thermal conductivity advocated the use of Johansen's (1977) or de Vries' (1952) models for moist, frozen soils. Johansen's model for frozen soils amounts to a geometric mean of the thermal conductivities of the soil constituents and it generally agrees well with de Vries' model for fine-grained, moist soils (Farouki, 1981). De Vries modelled the thermal conductivity of ellipsoid particles suspended in a continuous medium. Neither Johansen's nor de Vries' model explicitly permits segregated ice, which has the effect of re-structuring the geometry of the soil components. Both models predict a linear increase in D of 4 to 5 x 10^{-7} m^2 s^{-1} per unit increase in volumetric ice content until the available pore space is saturated with ice. As ice content increases beyond this saturation limit, the assumptions of both models regarding soil geometry break down.

In contrast to deVries and Johansen, Hallet and Rasmussen's (1993) idealized distribution of the air, ice, solid matrix and water in the soil resulted in an expression for the bulk thermal conductivity that allowed for the presence of segregated ice. They showed an increase in the bulk thermal conductivity until the pore capacity was saturated, at which point the conductivity peaked and decreased with the segregation of ice. This decrease in thermal conductivity translates into an even greater decrease in thermal diffusivity, since the bulk thermal heat capacity decreases with increased ice content, since ice has the lowest heat capacity of the non-gaseous soil constituents. The rate of decrease is strongly dependent on the gas content of the soil, with moderate decreases for a saturated soil. Below the maximum ice saturation, increases in ice content are expected to lead to increases in thermal diffusivity of the soil.

If we assume an increase in ice content from 0 to 0.5 $m^3 m^{-3}$ during freezing at 0.2 m depth (as suggested by the volumetric liquid water content data in Figure 5.5), the models of Johansen and de Vries predict a change in diffusivity of 2 to 2.5 x $10^{-7} m^2 s^{-1}$ on freezing. The observed diffusivities at 0.2 m increase from 2.7 x $10^{-7} m^2 s^{-1}$ in the summer to between 4 and 6.5 x $10^{-7} m^2 s^{-1}$ in the winter (Figure 5.5).

Observed winter thermal diffusivity profiles for 2001/2002 and 2002/2003 are similar to each other, with values between 3.4 x 10^{-7} and 1.6 x $10^{-6} m^2 s^{-1}$ (Figure 5.6). Yershov (1990) gives a range of 1.5 x10^{-7} for dry silty clays to 7 x $10^{-7} m^2 s^{-1}$ for frozen and saturated silty clays. Our values for most depths and years are reasonable but exceed the upper limit of the suggested range, particularly between 0.77 and 0.98 m depth, where the estimated thermal diffusivity exceeds that of ice by around 3.5 x $10^{-7} m^2 s^{-1}$ in all three

years, corresponding to the depth range for which significant segregated ice was observed during excavation. The soil profile layers above 0.77 m in 2001/2002 and 2002/2003 do not have bulk thermal diffusivities consistent with large amounts of segregated ice. The mean bulk thermal diffusivity over the depth range 0.12 to 0.51 m in the 2003/2004 profile is $8.8 \times 10^{-7} \text{ m}^2 \text{ s}^{-1}$, which corresponds to the depth range where ice content inferred from subsidence exceeds the porosity of the thawed soil by up to $0.1 \text{ m}^3 \text{ m}^{-3}$. The estimated values of 3.5 and $8.8 \times 10^{-7} \text{ m}^2 \text{ s}^{-1}$ for the shallowest soil layer, from 0.12 to 0.3 m depth, correlate with the measured values of 4.5 and $6 \times 10^{-7} \text{ m}^2 \text{ s}^{-1}$ for 2002/03 and 2003/04, respectively, at 0.2 m depth.

Volumetric latent heat production

Latent heat production (positive) or consumption (negative) for the three winter periods is presented in Figure 5.7. Lighter colours indicate the consumption of latent heat. We associate the release of latent heat under cryotic conditions with the formation of ice, since the soil is at or near saturation when freezing begins. Although it is probable that other heat producing or consuming processes are at work, such as sublimation near the ground surface or vapour transport, the scale is given in $W \text{ m}^{-3}$ and also in the rate of phase of water to ice ($kg \text{ m}^{-3} \text{ d}^{-1}$), using 333 kJ kg^{-1} as the latent heat of fusion. This follows Kane et al. (2001), who that non-conductive heat transfer processes other than solid-liquid phase change were generally much smaller in magnitude. The discontinuity in the gray scale marks the transition from a thermal energy source to a sink.

During freezing and thawing, the highest latent heat release rate is associated with volumetric water content changes between 0.2 and 0.1 m^3 m^{-3}. These high releases occur above 0.6 m in the first two winters. In the winter of 2003/04, high latent heat production during freezing occurs throughout the active layer to a depth of over 1 m. In general, the third year is characterized by greater negative and positive latent heat throughout the winter, as a result of the greater winter soil thermal gradients and lower soil temperatures. The colder soil temperatures result in uninterrupted thermal energy release between 0.6 and 0.9 m, whereas in the previous years, latent heat consumption occurred throughout the active layer during warming events.

The high, continuous rate of heat production throughout the winter of 2003/2004 around a depth of 0.65 m (up to 38 W m^{-3} versus less than 12 W m^{-3} in 2001/2002 and 2003/2003) is balanced out by the earlier occurrence of heat consumption above and below that depth at rates higher than in the previous two years. If latent heat production and consumption can be assumed to result from phase change at the liquid-solid transition, then the net change in ice content for all three years is quite similar (Figure 5.8), but the timing, distribution and intensity of phase change are different. In addition, in the low snow year, 2003/2004, latent heat consumption outpaces production by December 1, whereas in the previous two years, latent heat was produced in the active layer (between 0.3 and 1.1 m) until the ground thawed in the following spring. We suggest that the shallow and intermittent snow cover in the winter of 2003/2004 permitted relatively unimpeded sublimation and evaporation from the soil down to about 0.6 m, resulting in high thermal energy consumption.

Heave

Figure 5.2 shows three net winter heave profiles, measured between the end of summer (late August - early September) and early spring (mid-May), superimposed on the microtopography of the frost boil. The maximum net heave of around 0.12 m occurs at the frost boil boundary in all three years. Heave decrease with distance from the frost boil to close to zero at a distance of 1.6 m. Over the frost boil itself, the net heave is nearly constant (between 0.04 and 0.08 m) with horizontal position and between years. The net heave profiles for each winter are remarkably similar in magnitude, given the differences observed in freezing rates for each fall season. Maximum net winter heave thus occurs at the frost boil's margin, not at its center, in all three years.

Segregation of ice at the frost front results in heave normal to the frost front. The frost front penetrates the soil more rapidly beneath the frost boil than adjacent to it, so that heave is oriented concentrically towards the center of the boil. We had therefore expected the greatest heave to occur at the boil center. For example, interpolated temperature data show that the penetrating frost front is inclined upward at a mean angle of 20° from a point 0.45 m below the center of the frost boil to a point 0.3 m beyond its border on September 19, 2002. We explain the location of this maximum net heave in one of two ways: either (i) the shape of the freezing front, the availability of water and the relative freezing rates beneath the boil and its margin lead to greater heave at the frost boil's margin than at its center, or (ii) maximum heave does occur at the frost boil center at some time during the winter but subsequent subsidence beneath the frost boil occurs prior

to the end of snow melt (during the winter). A single winter measurement of frost heave made in November 2002 was 0.02 m higher than in the following pre-thaw May, suggesting that sublimation or evaporation processes from the bare soil of the boil's apex could have decreased the ice content over the winter. It is not clear how subsidence might occur in a frozen, desiccated soil. The microtopography, surficial cracking and heave of the boil would contribute to these processes. The frost boils at Galbraith are elevated above the surrounding tundra and the high winds in the Atigun Valley can blow the snow off the frost boils alone. Under these conditions the surface of the frost boil is desiccated. When the snow pack is sufficient to cover the frost boils, there is no indication of the location of the boils at the snow surface. The snow pack is necessarily thinner above the frost boils than over the tundra, and moisture migration into the snow pack is exacerbated at the boil by a steeper temperature gradient through the snow pack. There can be no indication for this process using volumetric liquid water content, since it is independent of total water content at cold temperatures. Since thaw begins with the infiltration of melt water, the soil is saturated before all of the ice disappears in spring. Such an invisible loss of ice to the atmosphere is consistent with the shape of the heave curves in Figure 5.2. For these three years, the recorded winter heave using the heave rods and calculated as the difference in ground surface position between the end of summer and the beginning of thaw is remarkably similar. The amount of heave depends on the freezing rate, and the dramatic difference in freezing rate between 2003 and the other two years lead us to expect differences in heave. For example, O'Neill and Miller (1985) simulated heave and observed an increase in ice segregation with a decrease in freezing rate. To explain the

similarity between years, we must either invoke processes that remove ice in late winter after a slow freeze-back, or the possibility that the heave rods shifted position during freezing. In the latter case, the heave rod position change is also invariant from year to year, however, and as difficult to account for as the lack of difference in overall heave. We examine differences between the years in ice content below.

Ice content as a function of depth

The timing of subsidence and the temperature profile during thawing are related to the distribution of ice content as a function of active layer depth. Figure 5.6 shows the variations in bulk thermal diffusivity for the soil layers indicated and the total volumetric ice content as a function of depth based on cumulative settlement and thaw in the springs of 2003 and 2004. Ice contents throughout the profile lay between 0.55 and 0.8, with lower ice content in 2002/2003 in the upper 0.76 m of the profile than in 2003/2004. Ice content exceeded the porosity in 2003/2004 over this same interval, suggesting that segregation occurred in the fall of 2003 to a greater degree than during the fall of 2002. In both years, freezing occurs via both the descent of a freezing front from the surface and an increase in the height of the frost table, although the latter process is much more pronounced in 2002/2003. The last depth to freeze in 2003/2004 is 0.79 m, which corresponds to the observed spike in ice content. There is an additional spike in ice content between 0.85 and 0.90 m in both years. The qualitative similarity between increases and decreases in ice content with depth suggest that the relative distribution of ice from year to year is stable, except for the upper portion of the active layer, which is

subject to repeated diurnal freeze-thaw cycles during freezing (Overduin et al., 2003). The spikes in ice content below 0.75 m correspond with the segregated ice observed in the field during excavation. Based on its position, this ice is probably segregated during upward movement of the frost table during freeze-back (Figures 5.3 and 5.6). Based on position, the inter-annual variability in shallow active layer ice content is determined by snow pack and heat transfer conditions at the surface, which affect post-freeze redistribution of water, rather than freezing rate. Deeper ice content does not seem to be as freezing-rate dependent, and is therefore less variable from year to year.

Conclusions

As a result of changes in ice content during freezing, frost boils at Galbraith Lake in the Brooks Range of Alaska heave during freezing up to 0.2 m at their margins, while heave of the surrounding tundra is negligible. Settling of the ground surface and the development of the active layer together permit estimation of the pre-thaw vertical distribution of ice in the active layer. The estimates of ice content are consistent with changes in the bulk thermal diffusivity of the frozen soil calculated from soil temperatures. Measurements of the volumetric liquid water content of the soil do not distinguish between drying and freezing, and are not reliable indicators of ice content changes. Thermal diffusivity measurements provide an indication of changes in ice content during snowmelt infiltration, when desiccated soil near the ground surface increases in ice content.

Subsidence at the frost boil center occurs mostly by the middle of June, so that most seasonal ice segregation occurs in the upper 0.4 m of the active layer. This was true regardless of differences in freezing front penetration rate for the prior winters. Net frost boil winter heave is lower than at the frost boil margins, which is attributed either to loss of moisture via evaporation or sublimation through the exposed mineral soil of the frost boil during the winter or to the effect of slower freezing rates beneath the frost boil margin. It is possible that low total moisture contents in the shallow soil horizons where most heave occurs results in low lateral displacement of soil during heave. Subsequent subsidence, which is assumed to have no horizontal component, would return material to its pre-heave position. Added to the low (< 0.05 m) interannual variability in heave, this suggests that these frost boils are stable features with respect to changes in fall freezing conditions.

Acknowledgements

References for Chapter 5

Bittelli, B., Flury, M., Gaylon S. C., 2003. A thermodielectric analyzer to measure the freezing and moisture characteristic of porous media. Water Resources Research 39(2), doi:10.1029/2001wr000930.

Burn, C. R., 1998. The active layer: two contrasting definitions. Permafrost and Periglacial Processes 9: 411-416.

Carslaw, H. S., Jaeger, J. C., 1990. Conduction of Heat in Solids, 2nd ed. Clarendon Press, Oxford.

de Vries, D. A, 1952. Heat transfer in soils. in: de Vries, D. A., Atgan, N. H., Heat and mass transfer in the biosphere: 1. Transfer processes in the plant environment. John Wiley and Sons, pp. 5-28.

Farouki, O. T., 1981. Thermal properties of soils. Cold Region Research and Engineering Laboratory (CRREL) Monograph 81-1.

Hallet, B., Rasmussen, L. A., 1993. Calculation of thermal conductivity of unsaturated frozen soil near the melting point. Permafrost Sixth International Conference, Proceedings July 5-9, 1993 , Beijing , China. pp. 226-231.

Harris, C., Smith, J. S., 2003. Modelling gelifluction processes: the significance of frost heave and slope gradient. Proceedings of the 8th International Conference on Permafrost, Zurich, eds. M Phillips, S M Springman and L U Arenson, Balkema, Lisse, Netherlands. pp. 355-360.

Harris, C., Helfferich, D., 2005. Who is BOB? Agroborealis 36(2): 29-32

Heimovaara, T. J., Focke, A. G., Bouten, W., Verstraten, J. M., 1995. Assessing temporal variations in soil water composition with time domain reflectometry. Soil Science Society of America Journal 59: 689-698.

Johansen, O., 1977. Thermal conductivity of soils. Draft Translation 627, U. S. Army Cold Regions Research and Engineering Laboratory (CRREL) Report, Hannover, New Hampshire, pp. 291.

Kane, D. L., Hinkel, K. M., Goering, D. J., Hinzman, L. D., Outcalt, S. I., 2001. Non-conductive heat transfer associated with frozen soils. Global and Planetary Change 29(3-4): 275-292, doi:10.1016/S0921-8181(01)00095-9.

Kessler, M. A.,Werner, B. T., 2003. Self-organization of sorted patterned ground. Science 299: 380-383.

Mizusaki, T., Hiroi, M., 1995. Frost heave in He. Physica B 210: 403-410.

Oechel, W. C., Hastings, S. J., Vourlitis, G. L., Jenkins, M., Riechers, G., Grulke, N., 1993. Recent change of arctic tundra ecosystems from a net carbon dioxide sink to a source. Nature 361: 520-523.

O'Neill, K., Miller, R. D., 1985. Exploration of a rigid ice model of frost heave. Water Resources Research 21: 281–296.

Osterkamp, T. E., 2003. A thermal history of permafrost in Alaska. in: Proceedings of the Eighth International Conference on Permafrost, 21–25 July 2003, Balkema Publishers, Zurich, Switzerland, pp. 863–868.

Overduin, P. P., Young, K. L., 1997. The Effect of Freezing on Soil Moisture and Nutrient Distribution at Levinson-Lessing Lake, Taymyr Peninsula, Siberia. Proceedings of the Symposium on the Physics, Chemistry and Ecology of Seasonally Frozen Soils, Fairbanks, Alaska, June 9–12, 1997, pp. 327-333.

Overduin, P. P., Ping, C.-L., Kane, D. L., 2003. Frost boils, soil ice content and apparent thermal diffusivity. In *Proceedings of the 8th International Conference on Permafrost, Zurich*, Phillips M, Springman SM, Arenson LU (eds). Balkema: Lisse, Netherlands, pp. 869-874.

Overduin, P. P., Yoshikawa, K., Kane, D. L., Harden, J., 2005. Comparing electronic probes for volumetric water content of low-density feathermoss. Sensor Review 25(3): 215-221.

Ping, C. L., Michaelson, G. J., Overduin, P. P., Stiles, C.A., 2003. Morphogenesis of frost boils in the Galbraith Lake area, Arctic Alaska. In: Proceedings of the 8th International Conference on Permafrost, Zurich, Phillips M, Springman SM, Arenson LU (eds). Balkema: Lisse, Netherlands; pp. 897-900.

Rempel, A. W., Wettlaufer, J. S., Worster, M. G., 2004. Premelting dynamics in a continuum model of frost heave. Journal of Fluid Mechanics 498: 227-244.

Roth, K., Schulin, R., Fluehler, H., and Attinger, W. 1990. Calibration of time domain reflectometry for water content measurement using a composite dielectric approach. Water Resources Research 26: 2267-2273.

Roth, K., Boike, J., 2001. Quantifying the thermal dynamics of a permafrost site near Ny-Ålesund, Svalbard, Water Resources Research 37(12): 2901-2914. DOI: 10.1029/2000WR000163.

Soil Survey Staff, 2005. National Soil Survey Characterization Data, Soil Survey Laboratory, National Soil Survey Center, USDA, NRCS, Lincoln, NE.

Taber, S., 1929. Frost heaving. Journal of Geology 37: 428-461.

Vliet-Lanoë, van B., 1991. Differential frost heave, load casting and convection: converging mechanisms; a discussion of the origin of cryoturbations. Permafrost and Periglacial Processes 2: 123-139.

Walker, D. A., Epstein, H. E., Gould ,W. A., Kelley, A. M., Kade, A. N., Knudson, J. A., Krantz, W. B., Michaelson, G. J., Peterson, R. A., Ping, C.-L., Raynolds, M. K., Romanovsky, V. E., Shur, Y., 2004. Frost-Boil Ecosystems: Complex Interactions between Landforms, Soils, Vegetation and Climate. Permafrost and Periglacial Processes 15: 171–188. DOI: 10.1002/ppp.487.

Washburn, A. L., 1956. Classification of patterned ground and review of suggested origins. Geological Society of America Bulletin, 67: 823-865.

Wettlaufer, J. S., Worster, M. G., in review. Premelting dynamics. Review of Fluid Mechanics.

Yershov, E. D., 1990, General Geocryology. Cambridge University Press, 580 pp.

Zhu, D.-M., Vilches, O. E., Dash, J. G., Sing, B., Wettlaufer, J. S., 2000. Frost heave in argon. Physical Review Letters 85: 4908-4911.

Table 5.1. Frost boil center soil profile properties.*

| sample depths [m]	bulk density [Mg m^{-3}]	clay, silt, sand contents [% wt.]	total carbon [% wt]	porosity [-]	C/N [-]	CEC [cmol kg^{-1}]
0.06	1.62	43.9, 44.4, 11.7	2.21	0.78	10	0.121
0.16	1.74	44.5, 44.2, 11.3	2.21	0.66	9	0.139
0.28	1.76	43.2, 43.7, 13.1	2.32	0.63	8	0.122
0.44	1.75	43.4, 43.1, 13.5	2.25	0.64	9	0.126
0.66	1.73	43.2, 45.1, 11.7	2.18	0.66	11	0.125
0.83	1.75	36.0, 38.7, 25.3	2.62	0.63	9	0.113
1.09	1.72	44.3, 43.3, 12.4	2.19	0.66	9	0.141

* data provided by the National Soil Survey, Soil Survey Laboratory, National Soil Survey Center, USDA, NRCS, Lincoln, NE.

Table 5.2: List of Symbols for Chapter 5.

A	constant	--
B	constant	--
C	heat capacity (C_n: of the nth soil component)	$\mathrm{J\ kg^{-1}\ K^{-1}}$
D	thermal diffusivity	$\mathrm{m^2\ s^{-1}}$
$\underline{D}$	mean bulk soil thermal diffusivity	$\mathrm{m^2\ s^{-1}}$
D_i	mean bulk soil thermal diffusivity of the ith soil layer	$\mathrm{m^2\ s^{-1}}$
$\underline{D}_n$	mean bulk soil thermal diffusivity to the nth sensor depth	$\mathrm{m^2\ s^{-1}}$
L_f	latent heat of fusion	$\mathrm{J\ kg^{-1}}$
R_T	thermistor resistance	Ω
T	soil temperature	$^\circ\mathrm{C}$
$\overline{T}$	mean daily soil temperature	$^\circ\mathrm{C}$
T_f	freezing temperature	$^\circ\mathrm{C}$
f_T	transfer function	$\mathrm{s^{-1}}$
k	thermal conductivity	$\mathrm{W\ m^{-1}\ K^{-1}}$
r_h	heat production (+ve) or consumption (-ve) in the soil	$\mathrm{W\ m^{-3}}$
r_{est}	estimated latent heat production (+ve) or consumption (-ve) in the soil	$\mathrm{W\ m^{-3}}$
t	time	s
t_d	number of seconds per day (86400 s)	s
z	depth below ground surface	m
Δz_0	change in ground surface position relative to permafrost	m
Δz_{ft}	change in frost table position relative to permafrost	m
δ_o	resistance offset (thermistors)	Ω
π	pi	--
θ_n	volumetric content of soil component n	$\mathrm{m^3\ m^{-3}}$
θ_i''	volumetric segregated ice content	$\mathrm{m^3\ m^{-3}}$
ρ_n	density of soil component n	$\mathrm{kg\ m^{-3}}$
τ	time offset	s

<div align="center">Subscripts</div>

|	
α	air
i	ice
j, k	sensor number, where the shallowest sensor is set to j, k = 1
n	nth soil component
w	water
s	soil
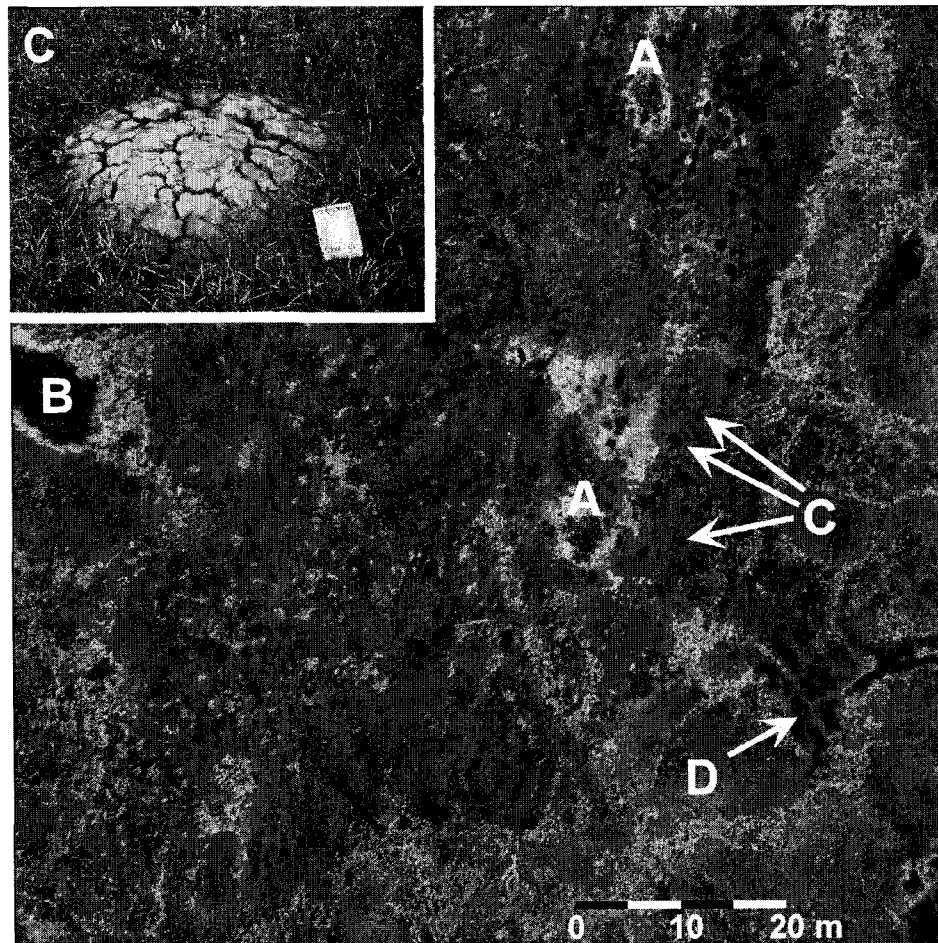
Figure 5.1. A normalized difference image of the study site using near-infrared and visible red wavelengths shows the distribution of periglacial landforms at the study site. A number of periglacial features are visible, including: A. ice, cored mounds; B. thermokarst features; C. frost boils; D. remnant polygonal ice wedges. The collection of dark spots and square at upper right are people and equipment. With the exception of the frost boils (C), vegetation cover is complete. The field book in the upper left inset image is 12 cm wide (aerial image courtesy of Dr. N. Harris, University of Alaska Fairbanks).
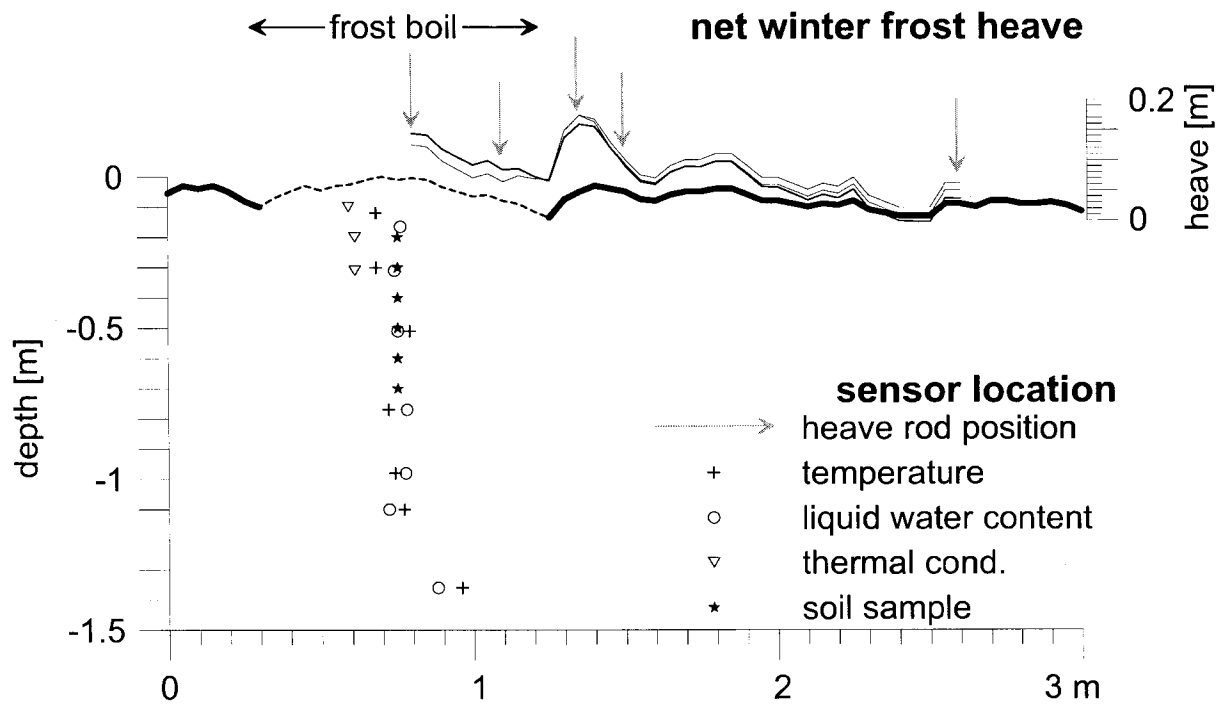
Figure 5.2. A cross-section of the frost boil (dashed line) and surrounding (thick line) microtopography measured at 0.05 m intervals on August 27, 2001, with the positions of the instruments. The three thin solid lines indicate heave superimposed on this topographic profile measured between the end of summer and the beginning of subsequent thaw for the winters of 2001/02, 2002/03 and 2003/04. The vertical scale for the heave data has been exaggerated by a factor of two (scale at right). Subsurface instruments include 0.3 m long TDR sensors for volumetric liquid water content, thermistors for soil temperature, heave rods and transient heat pulse sensors for thermal conductivity and diffusivity. Heave rods extended from anchors in the permafrost to above the ground surface.
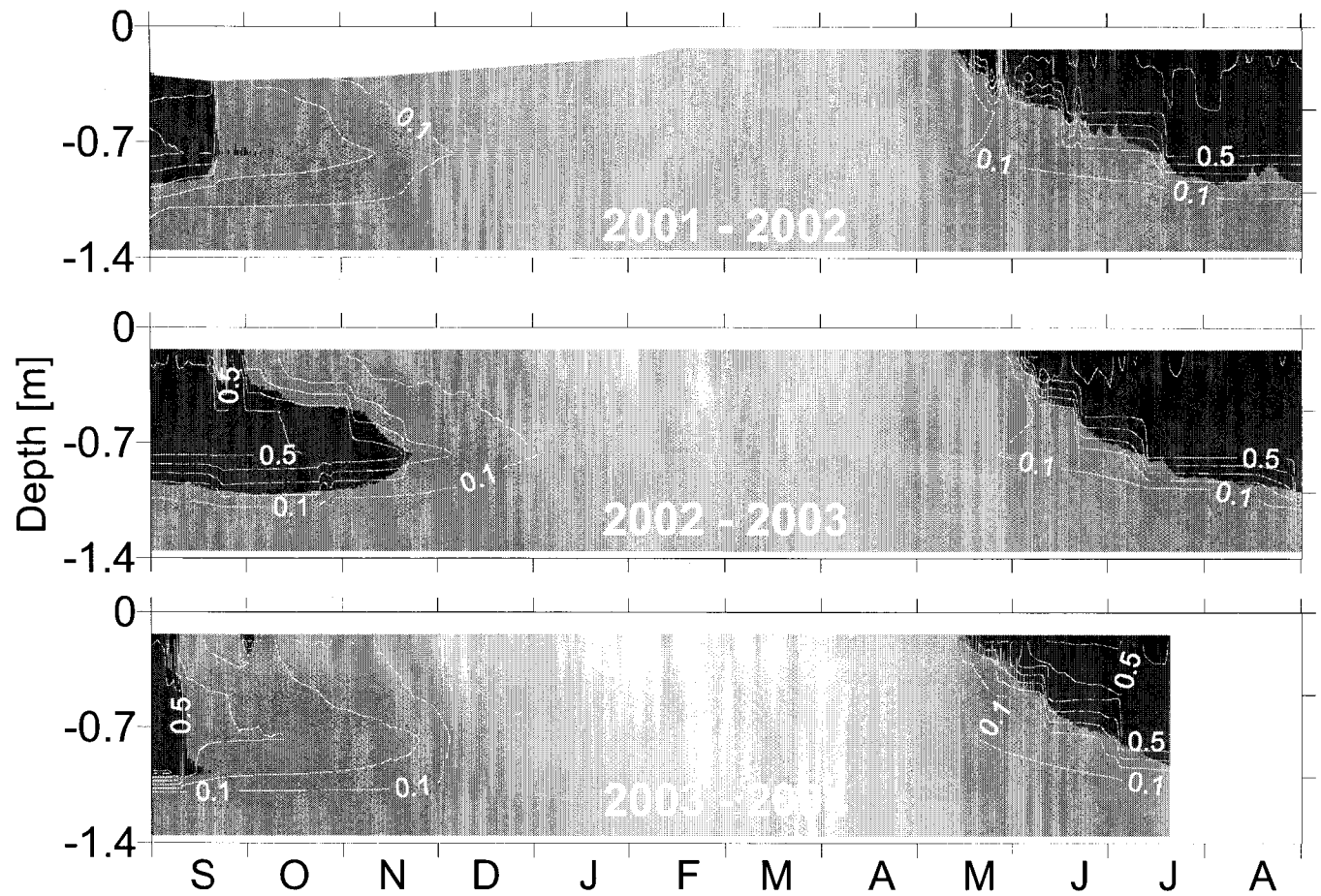
Figure 5.3. Soil temperature (grey scale at right) and soil liquid water content (contour interval of 0.1 m^3 m^{-3}) beneath the cent three hydrologic years. The shallowest water content sensor was inoperative during freezing in 2001 and data recording ended
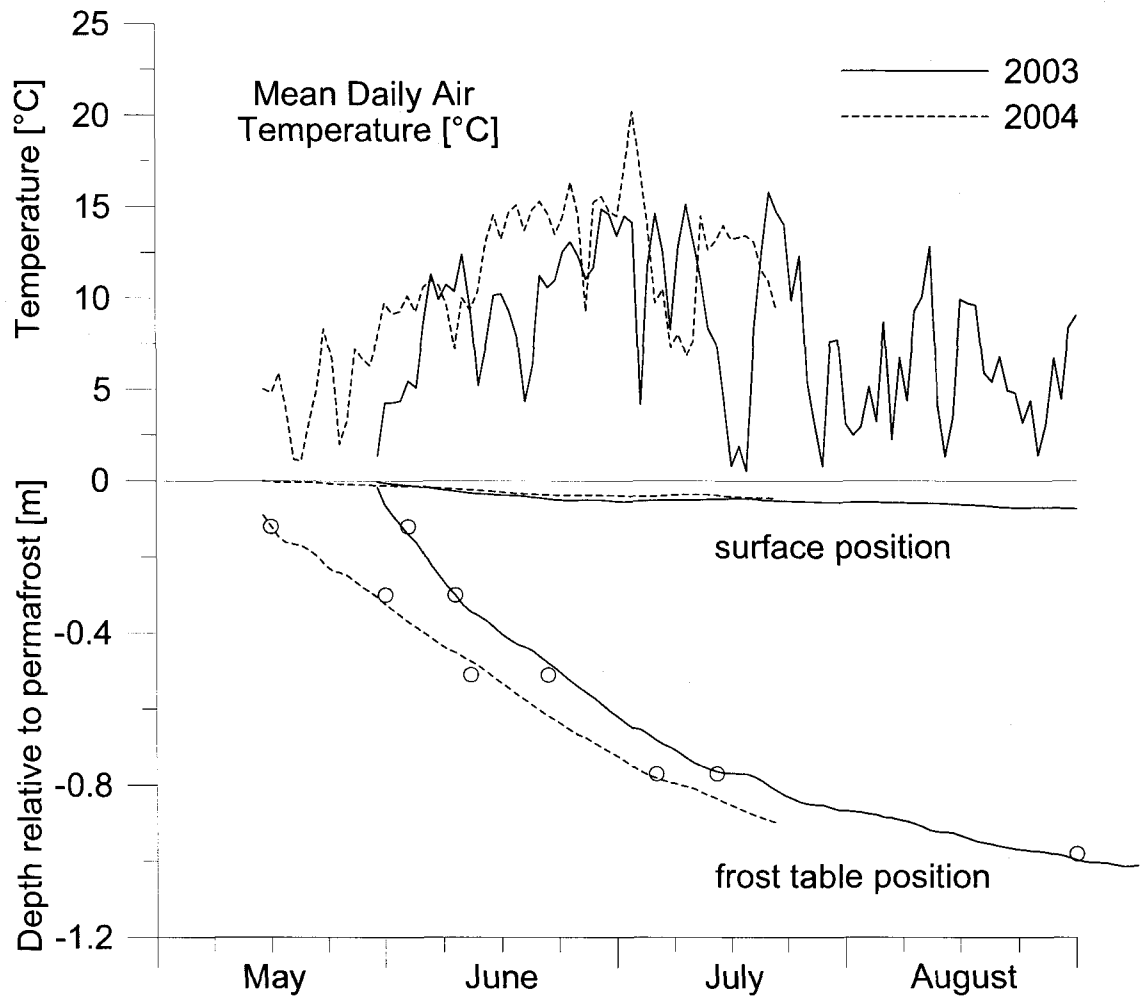
Figure 5.4. The mean daily air temperature (upper graph), the position of the ground surface and the frost table depth relative to the ground surface (at 0 m) are shown for the summers of 2003 and 2004. The frost table depth is estimated by fitting observed thaw using time domain reflectometry sensor to degree-days of thawing from the mean daily air temperature record using the Stefan solution for thaw depth. Observed thaw depths (frost table) are shown as circles for both years. Data recording did not extend beyond July 21st, 2004, and the records for that summer are truncated.
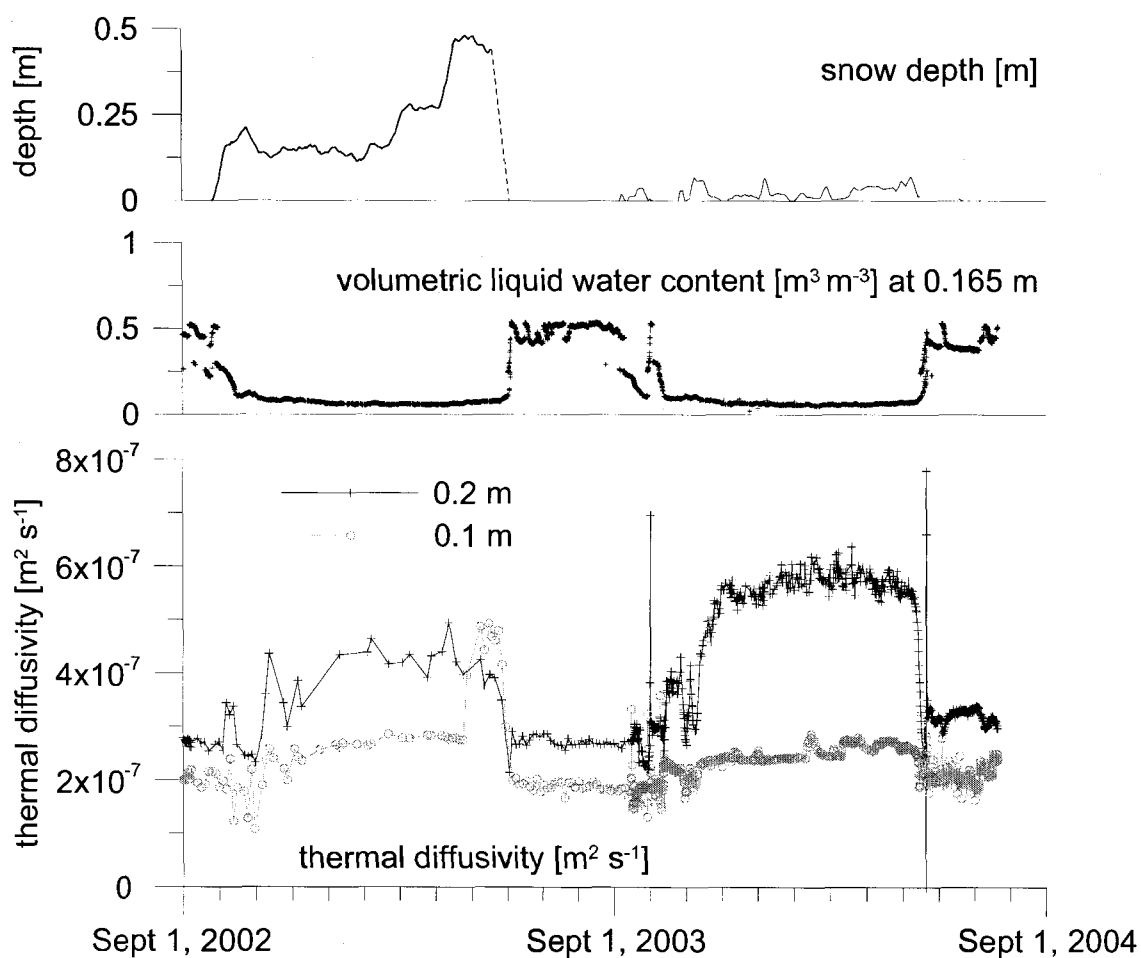
Figure 5.5. Snow depth for the winters of 2002/2003 and 2003/2004 are shown in the upper graph. Due to sensor malfunction, the 2002/03 record ends on May 19, 2002, before snowmelt occurs; a straight dashed line interpolates between this point and the end of melt. The second graph shows the volumetric liquid water content [$m^3 m^{-3}$] measured at 0.165 m depth. The thermal diffusivity [$m^2 s^{-1}$] as a function of time, calculated from measured thermal conductivity and soil composition at two depths, 0.1 (gray) and 0.2 m (black), is shown for the same period in the lower graph.
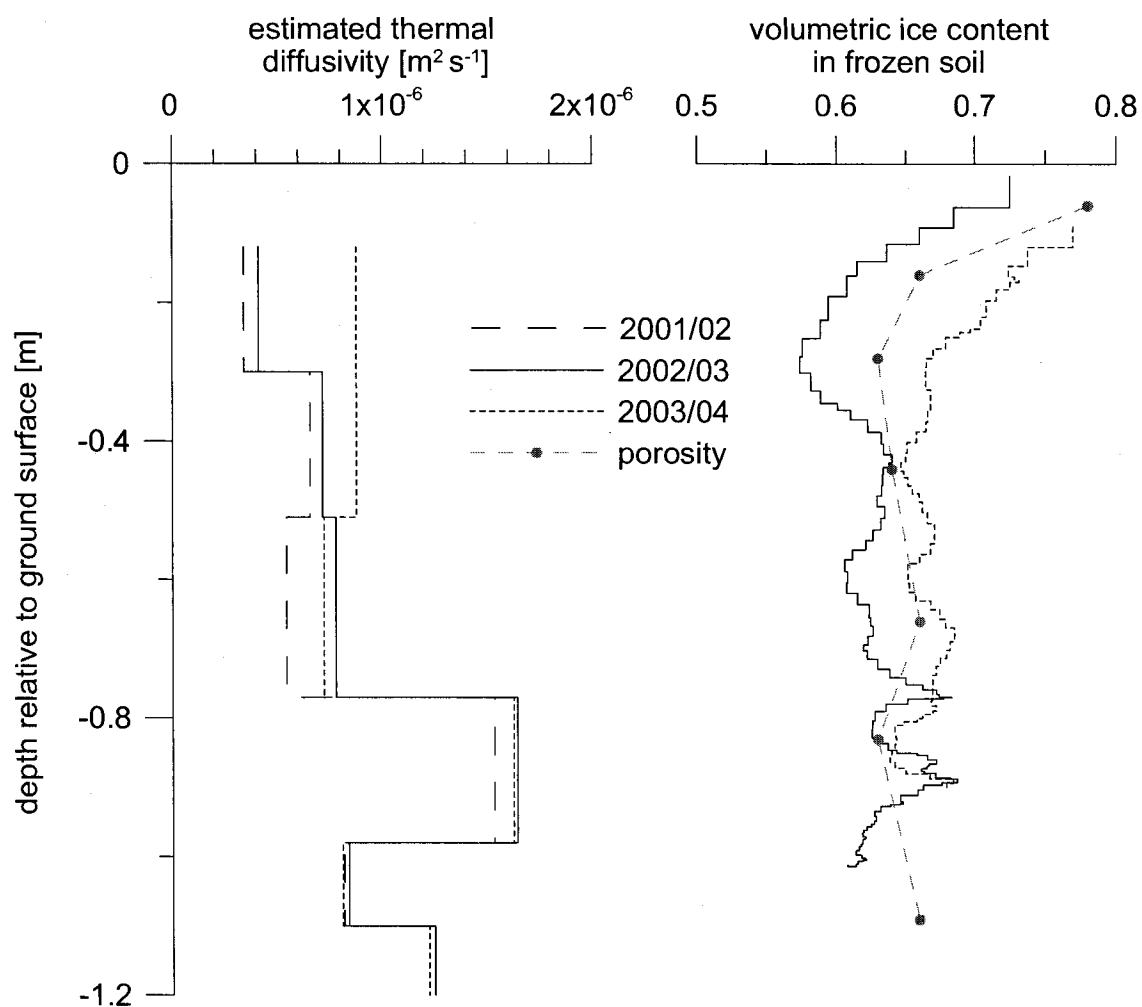
Figure 5.6. Bulk thermal diffusivity and volumetric soil ice content calculated based on the spring subsidence rate as a function of depth of thaw. Diffusivity is shown for all three years; ice content is available for 2002/2003 and 2003/2004 only. Porosity was measured on samples at various depths and is indicated as grey circles; porosity values are joined with a grey dashed line only as a visual aid.
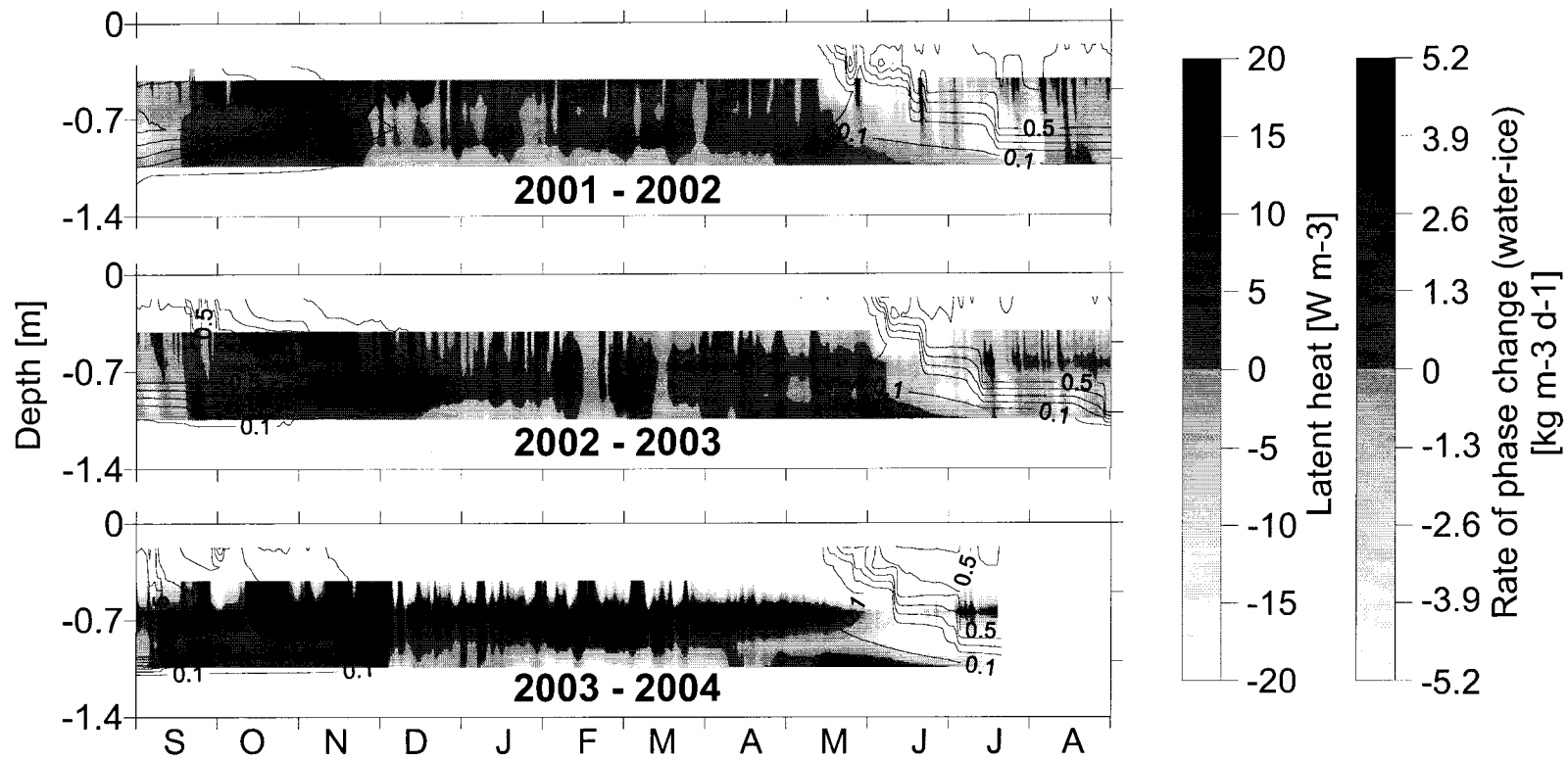
Figure 5.7. The latent heat production calculated from the temperature data and using thermal diffusivity as a function of depth (as shown on the left-hand side of Figure 5.6). The contour lines show liquid water content with a 0.1 contour interval. A discontinuity in the gray scale indicates the transition between heat source and sink.
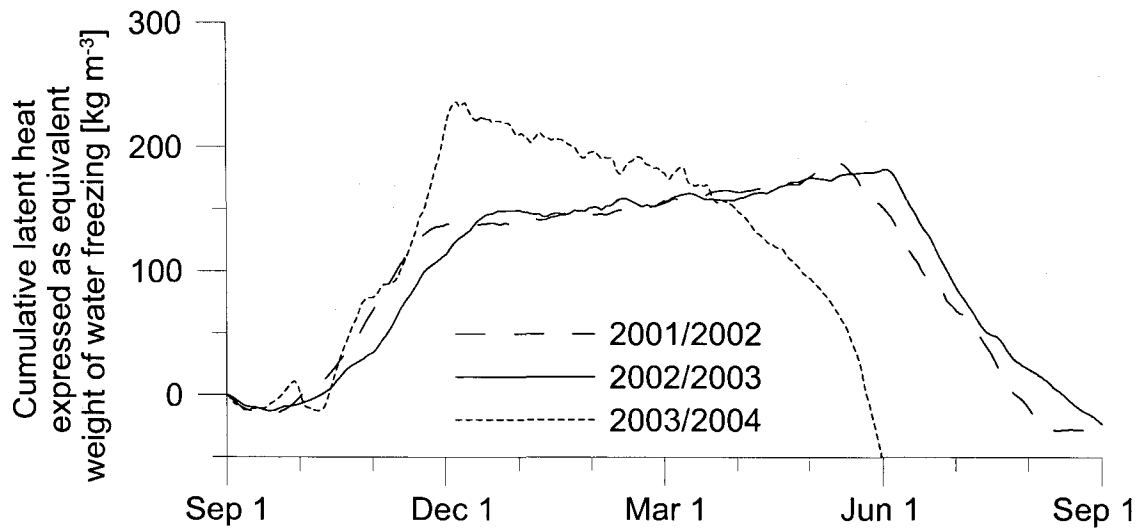
Figure 5.8. The net volumetric latent heat production integrated over the depth range 0.3 – 1.1 m for all three winter periods, expressed as the equivalent amount of water undergoing freezing or thawing. Accumulation of the latent heat production was set to 0 kg m^{-3} on September 1 for each year. Negative values represent the net consumption of latent heat, and positive values the release of latent heat.

Chapter 6 - Conclusions

The term patterned ground refers to quasi-periodic features formed by processes associated with cyclic freezing and thawing in a permafrost landscape. Patterned ground is identified by changes in the vegetation, and by small changes in microtopography. Sorting of soil particles by size is also a distinguishing feature but is not necessary for patterned ground. Patterned ground presents a set of challenges to field scientists, since it results in strong gradients of temperature and of soil components over small distances. The determination of the physical characteristics of the soil such as liquid water content and temperature, and bulk properties such as thermal conductivity and relative dielectric permittivity, require techniques that take into account variations in related material properties across spatial scales.

The use of electronic methods for measuring soil water content has become widespread since its introduction in the 1960s. Electronic methods offer a non-destructive means of obtaining high temporal resolution data. Their cost has fallen and the variety of sensors available has risen. Their use in organic matter rich soils is widespread, but only two manufacturers that we know of provide a calibration for their sensor in organic materials. Each of these sensors operates by measuring the bulk relative dielectric permittivity of the soil, either directly or through a proxy, and by relating this value to the volumetric liquid water content of the soil. We demonstrate that six of the sensors are suitable for use in feathermoss, a moss that is truly ubiquitous in Alaskan landcover, and throughout tundra and boreal landscapes. Nonetheless, variation between sensors providing direct

measurements of the relative dielectric permittivity is great, up to 0.15 $m^3 m^{-3}$. We provide sensor specific calibrations between sensor output or dielectric permittivity and water content. By comparing these calibrations to standard time domain reflectometry measurements, we provide a means for relating measurements across a much wider range of instruments. Most importantly for the work in this thesis, the calibrations permit direct comparison of water contents measured in the different soil types found in a patterned landscape. In general, we show that differences in soil organic content and temperature mandate sensor and soil specific calibrations for a variety of electronic volumetric water content sensors.

Analogous to water content measurements, bulk thermal conductivity measurements have the potential to be influenced by the nature of the material in which they are used. The effects of contact resistance between the sensor and the soil, and the relative heat capacities of the sensor and the soil are factors generally assumed to be of little importance, but that may become important when measurements in dramatically different soils are compared. Additionally, although thermal conductivity measurements have a long history, the thermal conductivity of the soil has rarely been measured in a field setting, with the result that temporal variations in conductivity on diurnal, seasonal and inter-annual time scales has not been recorded. We use a commercially available thermal conductivity sensor to monitor changes in active layer bulk thermal conductivity. The sensor is innovative, in that it measures a radial temperature difference in the soil, rather than the temperature of the sensor itself. We present a cylindrical source model for the heat flow around the sensor that explicitly includes contact resistance and sensor heat

capacity effects. Sensitivity analysis shows that they both affect the temperature field around the sensor strongly at small times. A large time approximation for the model is therefore introduced. Analysis of field data using the approximation suggests that it is a significant improvement over the line source model usually used with needle transient heat pulse sensors.

We apply these techniques to collect physical data from ground patterned by frost boils at Galbraith Lake in the Brooks Range, Alaska. Frost boils are cryoturbated upwellings of the soil. They represent localized changes in surface characteristics and material properties that affect the energy balance at the surface and the thermal dynamics of the soil. The frost boil center freezes more quickly, thaws deeper and is subject to more diurnal freezing and thawing cycles than the surrounding vegetated soil. Differences in material properties lead to lower water contents near the surface of the frost boil than adjacent to it. Changes in water content during freezing are smaller in the frost boil center than for the surrounding organic horizon. Despite saturation of the soil prior to freezing, changes in thermal conductivity for soils close to 0.25 m depth are not directly related to phase change of the soil constituents, but suggest that ice content increased substantially within the frost boil but not at its edge.

These ice content differences led to an investigation of the dynamics of ice content in the frost boil over three winters. The pre-thaw vertical distribution of ice in the active layer is estimated using settling of the ground surface and the development of the active layer. These estimates are consistent with changes in the bulk thermal diffusivity of the frozen soil calculated from soil temperatures. Measured thermal diffusivity shows clear

indications of changes in ice content as a result of snowmelt infiltration. As a result of changes in ice content during freezing, net winter heave reaches a maximum at the frost boil margins, while heave in the surrounding tundra is negligible. Subsidence at the frost boil center occurs mostly in spring, so that most seasonal ice segregation occurs in the upper portion of the active layer, regardless of the freezing rate the previous fall. Heave is controlled by water availability and heat removal rates form the active layer and the apparent stability of the Galbraith frost boils under changing freezing conditions suggests that a decrease in water availability would be required to degrade them. Thus, patterned ground that exists as a result of differential heave may serve as a better indicator of moisture conditions than intensity of freeze/thaw action.

The high temporal resolution, *in situ* data generated in these studies of ice content and thermal conductivity contribute to the currently available field-based soil thermal conductivity studies. Since the thermal conductivity of the soil is most strongly affected by its water content, particularly in soils with high organic content, the water content calibrations are also critical to our ability to predict thermal behaviour of the soil. These data are of particular importance to those modelling atmospheric or subsurface dynamics, since the thermal conductivity of the shallow subsurface controls the heat exchange between the two spheres.

Appendix A - Soil stripes and active layer dynamics on Alaska's North Slope[*]

Abstract

Periglacial landforms are ubiquitous in the Alaskan Arctic. Within a small catchment in the northern foothills of the Brooks Range, several types of ground patterning at different scales may be found whose distribution is correlated with topography. Soil stripes and unsorted frost circles cover the crests and shoulders of the slopes, where drainage leads to drier soils and greater thaw depths. The pattern at the surface consists of vegetation differences and slight differences in topography perpendicular to the slope. These vegetation differences affect the spatial distribution of active layer bulk apparent thermal diffusivity. The effect of differences in thermal diffusivity is to change the active layer depth distribution and heat transfer to and from the permafrost. These changes in turn have the potential to affect the down-slope routing of water.

We compare aerial photos and measured topography from the centimetre to kilometre scale to define the region characterized by soil striping, and the differences in vegetation that characterize the mesic and xeric regions. Sensor profiles were installed in the soils defining the soil stripes. Three-year temperature and moisture profiles in the shallow subsurface of soil stripes show small differences in thaw depth heat transfer.

---

[*] first presented at the 2nd European Conference on Permafrost, Potsdam, Germany, June 12-16, 2005 as: Overduin, P. P. and Kane, D. L., 2005. Soil stripes and active layer dynamics on Alaska's North Slope. in preparation for publication in conference proceedings special issue of Permafrost and Periglacial Processes.

The dry dwarf shrub covered stripes are warmer in summer and colder in winter than the moist dwarf shrub and sedge-dominated stripes. There is a greater accumulation (over 0.5 m) of peat beneath the mesic stripes, while the organic soil horizon of the xeric stripes is less than 0.05 m thick. This results in a difference in thermal diffusivity, leading to shallower penetration of the surface heat flux in the mesic stripes. Active layer temperatures in the dry soil stripes are over 3 °C and up to 10 °C warmer throughout the profile at the warmest time of summer, leading to an undulating frost table at a meter to decameter scale.

Introduction

The question of how spatial variability in soil properties affects larger spatial means becomes important when integrative variables, such as watershed discharge, or larger-scale processes, such as modelling at a global circulation model scale, are considered. We are extending our study to a larger scale by quantifying the influence of larger-scale patterning, such as soil stripes and watertracks, on water movement.

Distribution and characteristics of soil stripes

Soil stripes at Imnavait Creek in the northern foothills of the Brooks Range Alaska are found on the shoulders and crests of this hilly terrain, running up and down the hill slopes in the direction of maximum slope. They are visible in the middle ground as parallel stripes of changing vegetation cover and exposed mineral soil (Figure A.1). A detailed

close up of the vegetation differences across a soil stripe is provided in Figure A.2. Soil stripes and water tracks are visible on hill crests and slopes, respectively, on the black and white aerial photograph (Figure A.3, left). Both run up and down the hill slope. The soil stripes are from 2-5 m wide, whereas the soil stripes are more irregularly spaced features at a decametre range. In each case, a change in the landcover type creates the visible patterning at the ground surface. The IR image (Figure A.3, right) shows exposed mineral material along the crest and the shoulder of the slope, isolated protruding mineral materials on the slope, and a different cover on the colluvial material in the valley bottom. The soil stripe-affected area of the hillslope is estimated by identifying contiguous regions exceeding a threshold brightness in an image produced by combining the visual spectrum aerial photograph with the red band of the infrared red-green-blue (RGB) intensity image. Elevation was used as a criterium to avoid including the similarly bright valley-bottom (Figure A.3-right). Based on this estimate, 15% of the slope area is stripe-affected, 12% is filled with colluvium, and the remaining 73% is characterized by water tracks. Walker et al. (1989) estimated that 15.25% of the watershed area consisted of nonsorted stone stripes; vegetation for this region is characterized as dry dwarf-shrub, fruticose-lichen tundra dominated by *Cassiopeia tetragona*, a description which is most apt for the 'dry' stripes.

Results

Effects on water table

The volumetric water content shows that the water table is below 0.31 m depth at the xeric site in the first half of the summer, whereas the mesic site is saturated at this depth (Figure A.4). At both sites, the water table rises above the 0.23 m sensor in response to precipitation events, which is shown by the TDR sensor at that depth reaching and remaining at saturation water levels. The water table does not rise above 0.05 m below the surface at either site (data not shown here).

Heat flux at surface

Figure A.5 shows the mean monthly heat flux measured using heat flux plates installed just below the surface in both stripes over a two and half year period. The data show that the soil beneath the xeric vegetation is subject to greater extremes of heat flux and therefore temperature than beneath the mesic vegetation. The thermal conductivity of the peat material is lower than that of the mineral soils just beneath the surface at the xeric site. Whereas the mineral soil thermal conductivity value about doubles with water content increases, peat can increase by an order of magnitude on wetting and freezing (Yoshikawa et al., 1998). While the mesic site heat flux does not vary much from year to year, the xeric site is more sensitive to changes in snowpack in winter.

Thaw depth

Figure 6.6 shows the active layer development as a function of time for two and a half years beneath the dry and moist soil stripes. The dry stripe thaws more rapidly in spring than the moist, leading to a difference in active layer depth of over 0.5 m in mid- to late June. The rapid active layer development beneath the xeric vegetation results in a frost table that is corrugated at a 3-5 m interval in mid-summer (Figure A.7). Surface slopes the stripe-affected region range from 0 to 3°. As a result of differences in thaw depth, the inclination of the frost table between the xeric and mesic regions reaches 20° in early summer. In late summer, active layer depth exceeds the peat layer thickness. Local flow will occur within the organic material and have a larger component perpendicular to the hill slope gradient than parallel to it.

Discussion

In this setting, downslope water migration is almost entirely restricted to the organic soil layers under saturated conditions, since the saturated hydraulic conductivities of the organics are one order of magnitude greater than those in mineral horizons (Hinzman et al., 1991) and since the porosity of the shallow organic layer is high. The description of the soil stripes as dry and moist derives from the vegetation communities found on each of the soil stripe types. It also reflects the porosities of the substrates. Differential thaw rates probably lead to early summer recharge of the xeric stripes; from mid-July onwards, the peat stripes are thawed and down slope movement of water occurs there. The

morphology of the organic soil horizon determines flow direction. Since the base of the organic soil horizon has a steeper slope lateral to the topographic slope, we expect subsurface flow to have a large component that is lateral to the topographic slope.

Directions for future work

There is evidence that the effects of these sub-pixel size (from a DEM standpoint) processes on catchment hydrology significantly affect hydrologic processes at the catchment scale. Recent work by Schramm (2005) suggests that current distributed models would most benefit by improvements to representations of soil moisture storage and thaw dynamics. We suggest that soil stripes are one of three surface morphologies (including water tracks and valley fill) that alter the rate of transport of water downhill in watersheds of the northern foothills of the Brooks Range, Alaska. Soil stripes are defined by periodic changes in landcover type across the slope, resulting in changes to the thermal and hydrological properties of the active layer soil. We demonstrate that one way in which soil stripes might have an impact on subsurface routing of water. We seek to include the effects of these features at higher scales, while avoiding the need for even higher-resolution DEMs.

Acknowledgements

References for Appendix A

Hinzman, L. D., Kane, D. L., Gieck, R. E., Everett, K. R., 1991. Hydrologic and thermal properties of the active layer in the Alaskan Arctic. Cold Regions Science and Technology 19:95-110

Kane, D. L., Gieck, R. E., Bowling, L. C., 2003. Impacts of surficial permafrot landforms on surface hydrology. In: Proceedings of the 8th International Conference on Permafrost, Zurich, Phillips M, Springman SM, Arenson LU (eds). Balkema: Lisse, Netherlands; 507-511.

Schramm, I., 2005. Hydrologic modeling of an arctic watershed, Alaska. Diploma thesis, University of Potsdam, 89pp.

Walker, D. A., Binnian, E., Evans, B. M., Lederer, N. D., Nordstrand, E., Webber, P. J., 1989. Terrain, vegetation and landscape evolution of the R4D research site, Brooks Range Foothills, Alaska. Holarctic Ecology 12: 238-261.

Yoshikawa, K., Bolton, W. R., Romanovsky, V. E., Fukuda, M., Hinzman, L. D., 2003. Impacts of wildfire on the permafrost in the boreal forests of Interior Alaska. Journal of Geophysical Research 108(D1): 8148, doi:10.1029/2001jd000438.
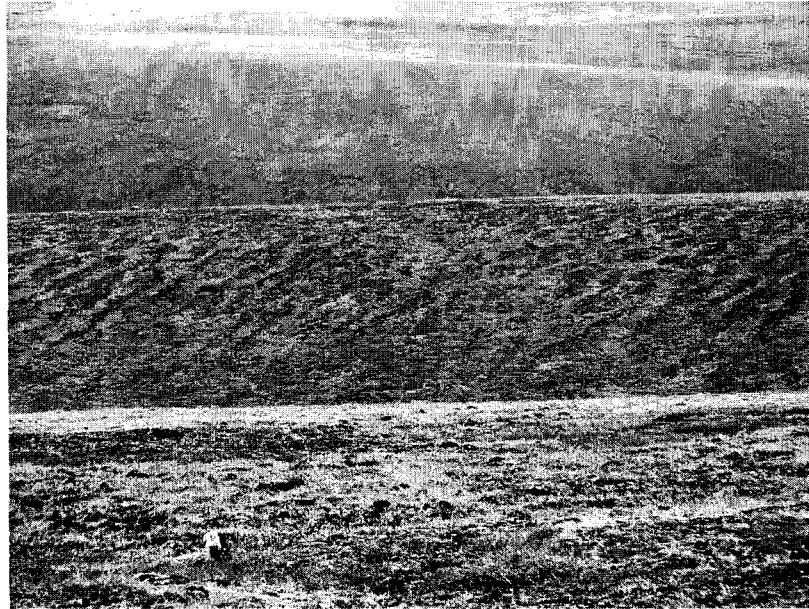
Figure A.1. Soil stripes at Imnavait Creek in the northern foothills of the Brooks Range Alaska are found on the shoulders and crests of this hilly terrain. They are visible in the middle ground in this photograph as parallel stripes of changing vegetation cover and exposed mineral soil.
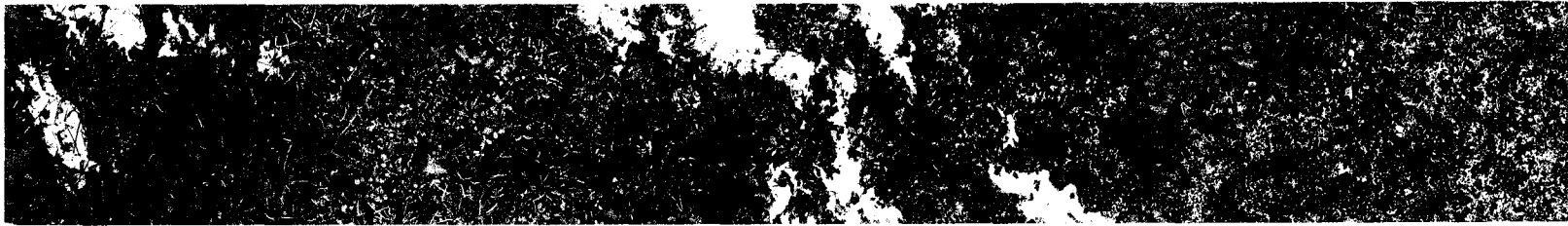
Figure A.2. The vegetative cover changes from the center of the mesic portion of the soil stripes (at left) to the center of the xeric portion (at right; the photograph is about 4 m wide). A frost boil (upper right portion of image) is evidence of active cryoturbation in the dwarf shrub stripe at right; frost boils are not found in the moist environment. Microtopography varies less than 0.2 m across the image. Digital elevation models are useful in identifying these features only if their lateral resolution is significantly better than 4 m. The characterization of the stripes as moist and dry is based on vegetation types (Walker et al., 1989).
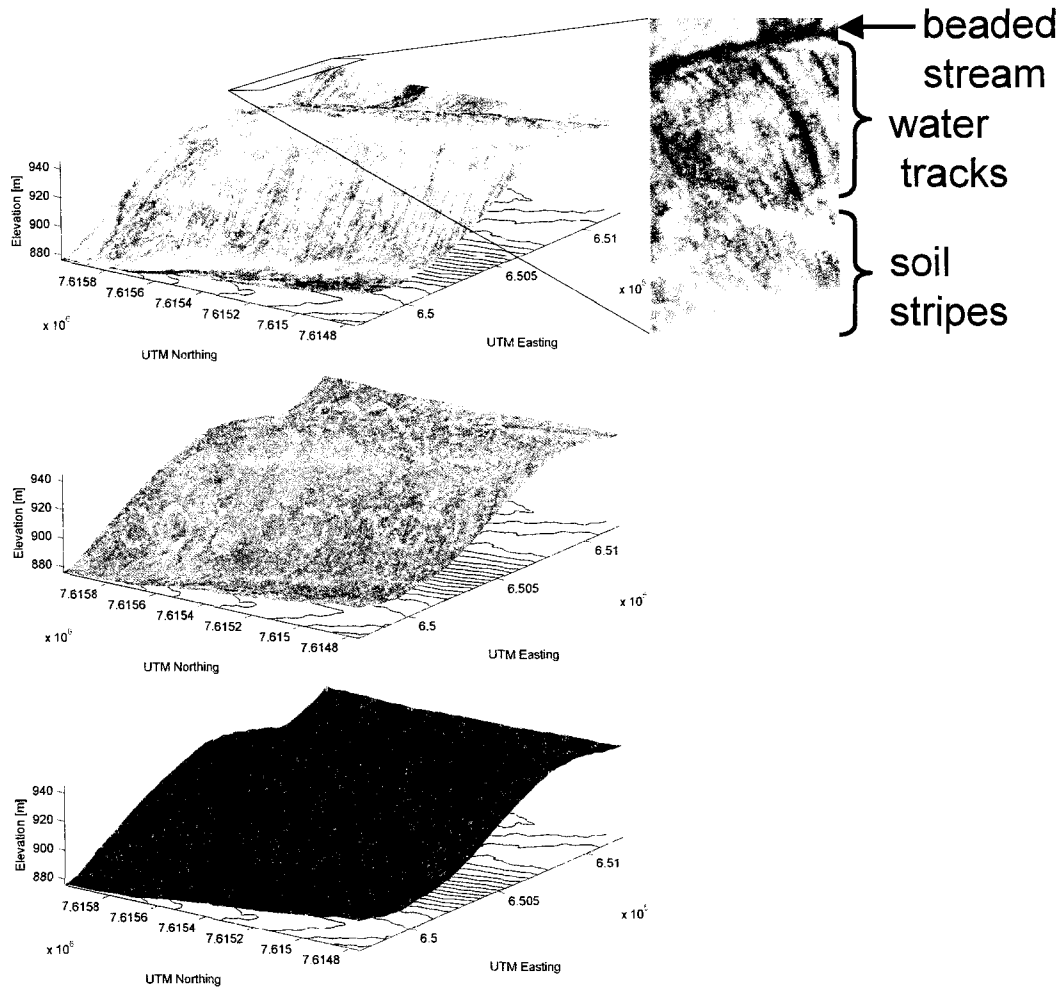
Figure A.3. A black and white image of the Imnaviat Creek west-facing hillslope taken during the 1950s is draped over the current topography in the upper image. Water tracks clearly mark the hillslope and the inset provides closer look at the distribution of water tracks and soil stripes from the crest of the hill (at the bottom of the inset) to the beaded stream in the valley. An infrared image of the west-facing hillslope (center image) shows differences in vegetation cover. The lower infrared intensity at higher elevations corresponds to lower vegetative cover. The topographic slope of the west-facing hillslope is shown in the lower image. Maximum values (in red) are 8° and minimum slopes (blue) are less than 0.01°. Fivefold vertical exaggeration has been applied to the images.
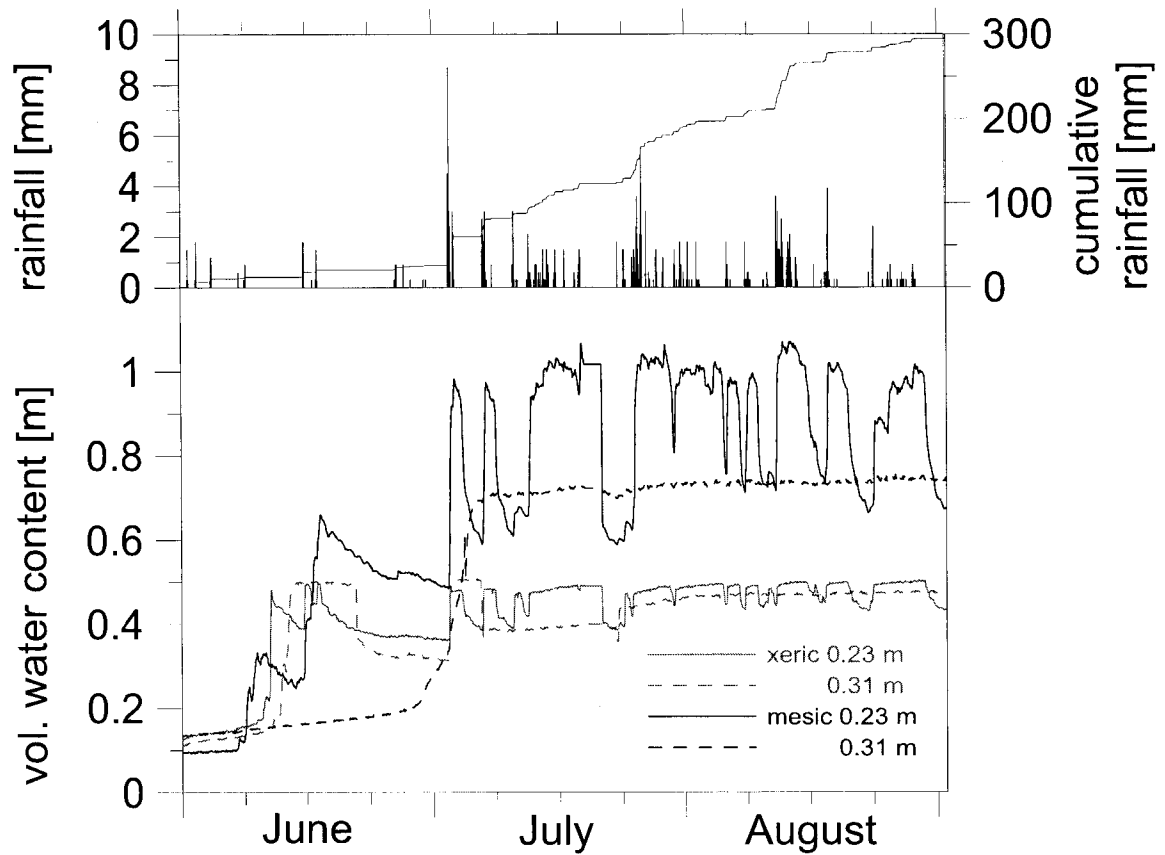
Figure A.4. Rainfall and changes in volumetric water content at two depths during the summer of 2003 are shown for the xeric and mesic stripes. Time domain reflectometry measurements of volumetric water content are treated using either a mineral or organic calibration, depending on soil horizon. Depths are expressed relative to a common datum.
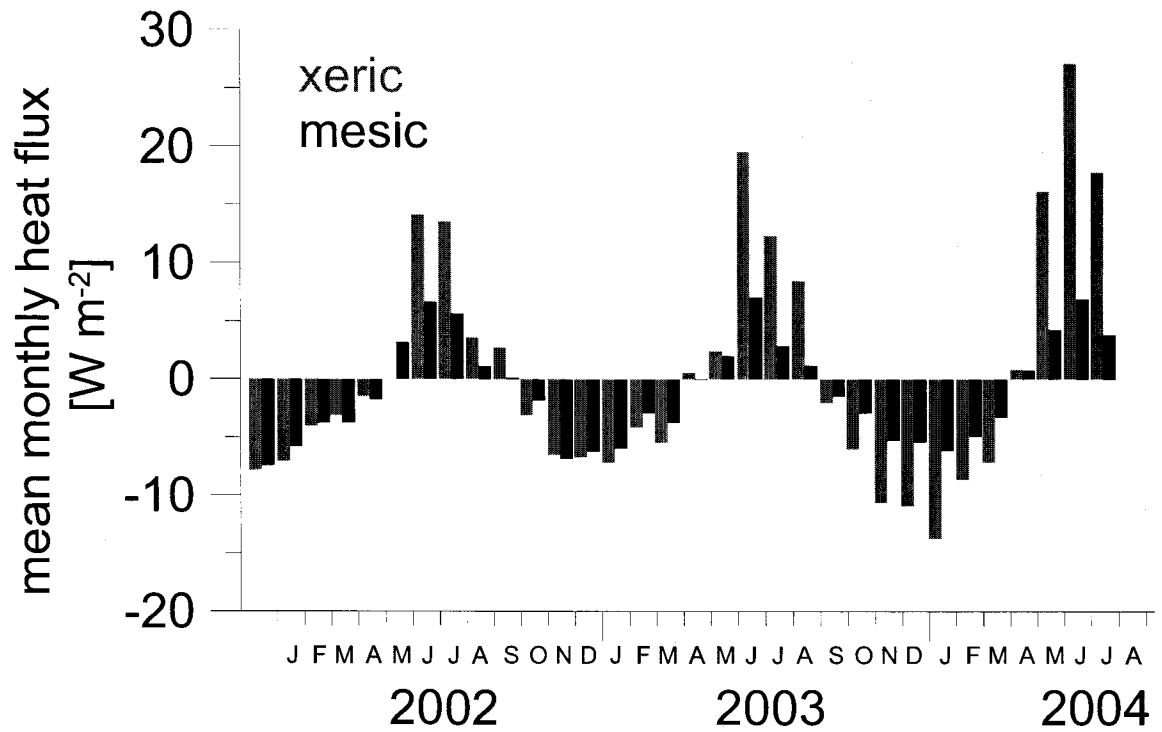
Figure A.5. Mean monthly heat flux measured using heat flux plates installed just below the surface in both stripes over a two and half year period.
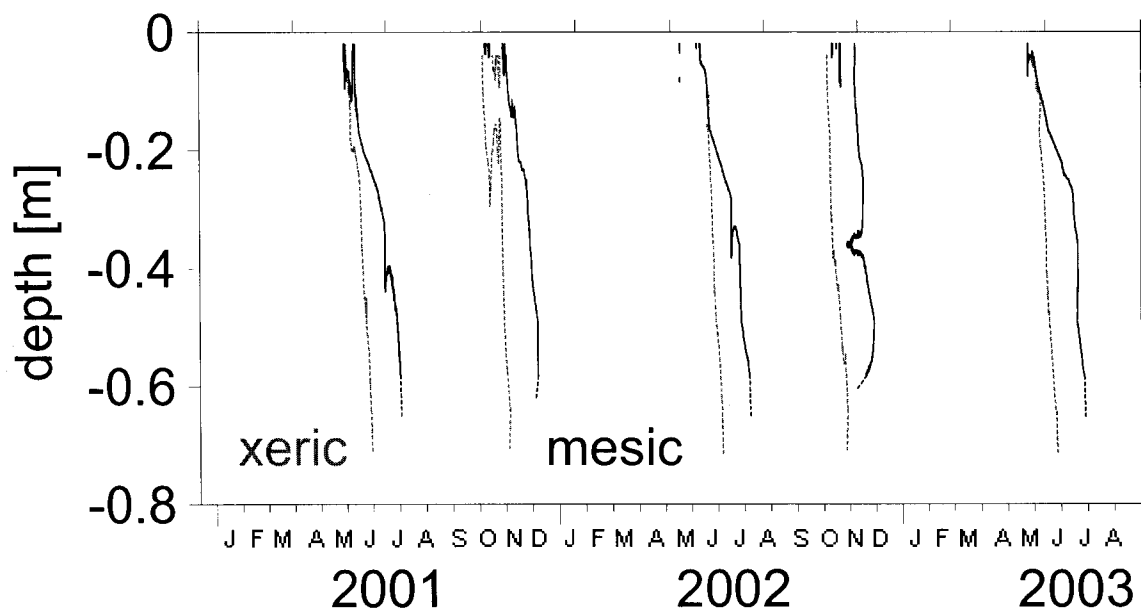
Figure A.6. The zero degree isotherm shows active layer development as a function of time for two and a half years beneath the dry (grey) and moist (black) soil stripes.
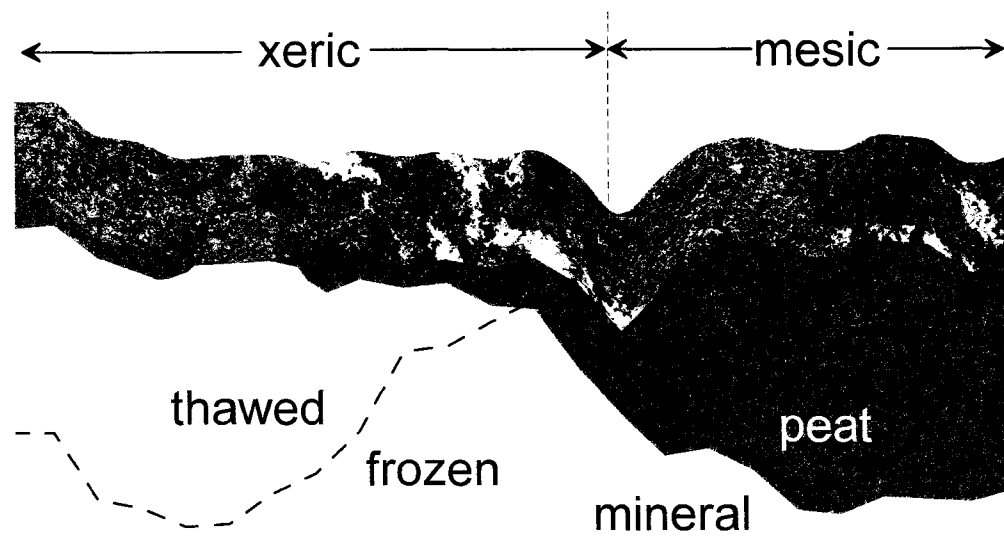
Figure A.7. The rapid active layer development beneath the xeric vegetation results in a frost table that is corrugated at a 3-5 m interval in mid-summer. A schematic of the active layer depth on June 20, 2003 is shown as a dashed line beneath the cover image.

Appendix B - Subsequent thermal data and analysis

The data presented in Chapter 4 pre-date the method of analysis of the thermal conductivity sensor output data developed in Chapter 3. Since publication of the manuscript, additional data have been collected and are available for analysis. This appendix presents and discusses these data and the results of the analytic method presented in Chapter 3.

Treatment of the Hukseflux TP01 thermal conductivity sensor data with a different model of heat flow led to a convergence of apparent thermal conductivities measured over multiple annual cycles in frozen soil (Chapter 3 and Figure 3.7). Based on the freezing characteristic curve there is some critical temperature (T_c) below which soil composition depends on temperature alone and the cooling and freezing arms of the freezing characteristic curve coincide (Bittelli, 2003; Figure 3.5). It is therefore reasonable to suppose that thermal conductivity values also converge to a single value over this temperature range, given the dependence of the thermal conductivity on soil composition and the reasonable assumption that the distribution of soil constituents does not differ greatly between cooling and warming soils. For this reason, I use the cylindrical heat flow model to re-evaluate the data presented in Chapter 4.

Figure B.1 presents thermal conductivity [W m^{-1} K^{-1}] in mineral ($<$ 2% carbon) and organic ($>$ 5% carbon) soils. The mineral soil sensors were installed at 0.06 (dry) and 0.18 m (wet) depth while the organic soil sensors were installed at 0.16 (dry) and 0.25 m (wet) depth. The mineral soil had higher thermal conductivities (0.4 to 1.6 W m^{-1} K^{-1})

than the organic (0.2 to 0.8 W m^{-1} K^{-1}), and the deeper sensors have higher conductivities

than shallow sensors. I disregard the spikes in apparent thermal conductivity associated

with soil temperatures close to the melting point of the soil solution, during phase change

in the spring and fall. The appearance of these spikes is discussed in Chapter 3 (page 62).

The lower thermal conductivity in the shallower soil is explained by lower water contents

there than in the deeper soil (Figure 5.3). Thermal conductivity values derived from the

heated cylinder model were significantly higher for the frozen soil than those obtained

using the linear heat source approximation. The low thawed mineral values, around 0.3

W m^{-1} K^{-1} (Figure 4.6), are an artefact of the analytic method, as shown in Figure B.2.

The changes in thermal conductivity with temperature for the same four sensors depicted

in Figure B.1 show a low value for near-surface organic material, around 0.2 W m^{-1} K^{-1},

which is almost independent of temperature. Moss and low-bulk density organic soil can

take on thermal conductivity values spanning an order of magnitude in variation

depending on moisture and ice content (Yoshikawa, 2003). The lack of variability

observed here can only be explained by a near-constant low liquid water contents. The

nearest TDR sensor is located 0.12 m away from this sensor, at about the same depth and

shows saturated conditions. The deeper organic sensor does show thermal conductivity

variability between 0.3 and 0.6 W m^{-1} K^{-1}, coinciding with changes in water content in

the thawed soil. In both organic and mineral soils, the increase in frozen soil thermal

conductivity with decreasing temperatures suggests significant ice content in the soil,

whereas the temperature independence of the frozen soil thermal conductivity for the

shallower sensors suggests an absence of ice.

The calculation of heat capacity in Chapter 4 was not based on measurements of soil composition, but on the ratio of thermal conductivity and diffusivity. Both were calculated using the linear heat source approximation. The interannual variability observed in the thermal conductivity using this model (Figure 3.7) thus creates interannual variability in the heat capacity that is an artefact of data treatment. Based on the sensitivities in Figure 3.1, the thermal diffusivity is subject to substantial uncertainty as it is best measured using radial temperature differences measured at short times. This has the result that the expected accuracy for thermal diffusivity measurements is +/- 20% (Hukseflux, 2001). Although local total moisture content is regarded as constant, measured spatial concentrations of soil components provide a more accurate means of estimating the heat capacity of the soil (e.g. Figure 3.6) than the thermal conductivity and diffusivity can provide, based on their high uncertainties.

Fitting a bimodal model of seasonal variability to thermal conductivity does not fit the measured data. Based on my observations, summer values vary depending on moisture contents, winter values are a function of temperature and the transition from summer to winter values occurs over a period of up to three months. Differences between organic and mineral soil values, and between summer and winter values, are smaller than tabulated values, such as those in Hinzman et al. (1998), Nakano and Brown (1972), Pavlov (1976), or Yershov (1990), that are often cited and used in modelling efforts (e.g. Anisimov et al., 1997). In the future, relating the thermal conductivity to liquid water content via the freezing characteristic may be the most effective means of

accommodating the temporal variability observed in models of active layer physical

dynamics.

References for Appendix B

Anisimov, O. A., Shiklomanov, N. I., Nelson, F. E., 1997. Global warming and active layer thickness: results from transient general circulation models. Global and Planetary Change 15: 61-77.

Bittelli, B., Flury, M., Gaylon S. C., 2003. A thermodielectric analyzer to measure the freezing and moisture characteristic of porous media. Water Resources Research 39(2), doi:10.1029/2001wr000930.

Hinzman, L. D., Goering, D. J., Kane, D. L., 1998. A distributed thermal model for calculating soil temperature profiles and depth of thaw in permafrost regions. Journal of Geophysical Research 103(D22): 28 975-28 991.

Hukseflux Thermal Sensors, 2000. TP01: Thermal Properties Sensor. Delft, Netherlands.

Nakano, Y. and Brown, J., 1972, Mathematical modelling and validation of the thermal regimes in tundra soils, Barrow, Alaska.Arctic and Alpine Research 4(1):19-38.

Pavlov, A.V, 1976. Thermophysics of Landscapes. Hydrometeoizdat, Leningrad, 276 pp. (in Russian).

Yershov, E. D., 1990, General Geocryology. Cambridge University Press, 580 pp.

Yoshikawa, K., Bolton, W. R., Romanovsky, V. E., Fukuda, M., Hinzman, L. D., 2003. Impacts of wildfire on the permafrost in the boreal forests of interior Alaska. Journal of Geophysical Research, 108(D1): 8148, doi:10.1029/2001jd000438.
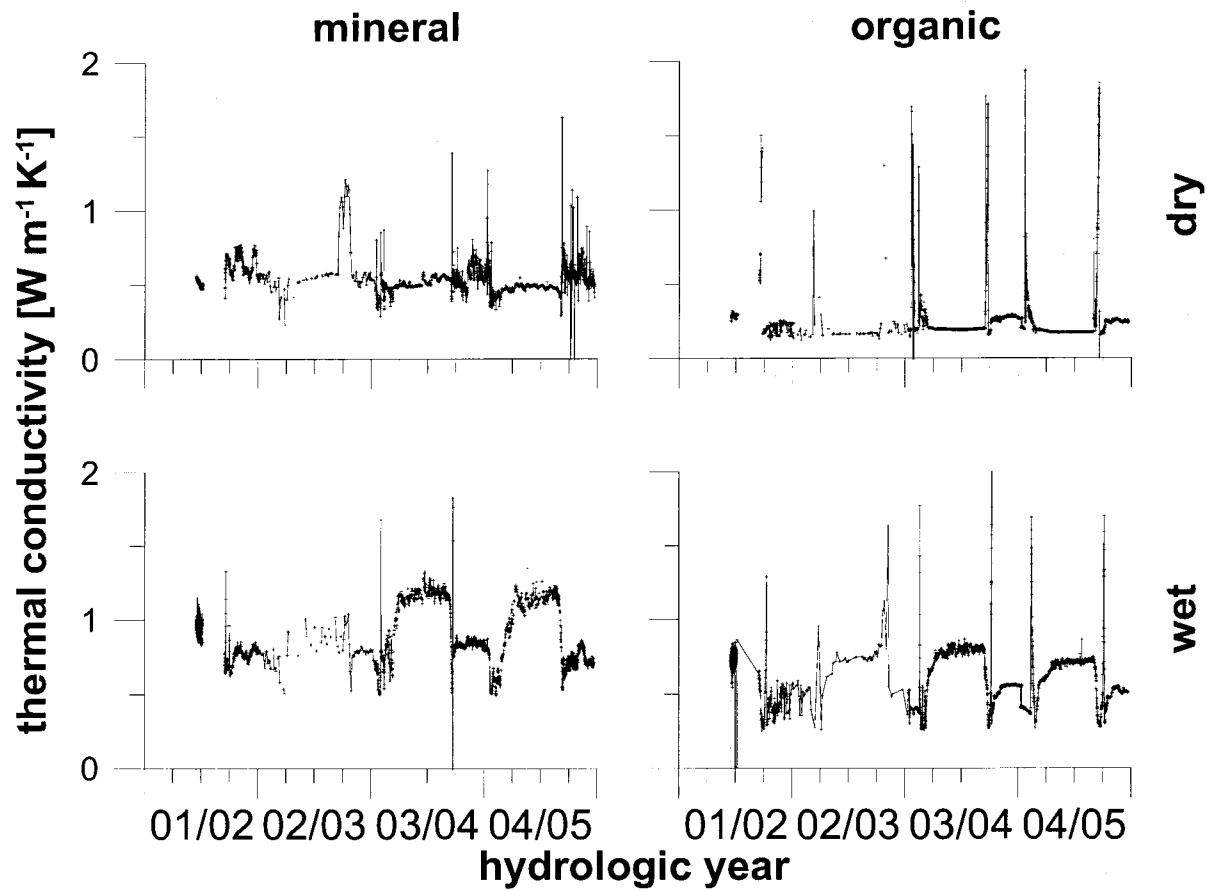
Figure B.1. The thermal conductivity [W m^{-1} K^{-1}] in mineral (< 2% carbon, at left) and organic (> 5% carbon, at right) soils. The mineral soil sensors were installed at 0.06 (dry) and 0.18 m (wet) depth while the organic soil sensors were installed at 0.16 (dry) and 0.25 m (wet) depth. The spikes in apparent thermal conductivity are associated with soil temperatures close to the melting point of the soil solution, during phase change in the spring and fall.
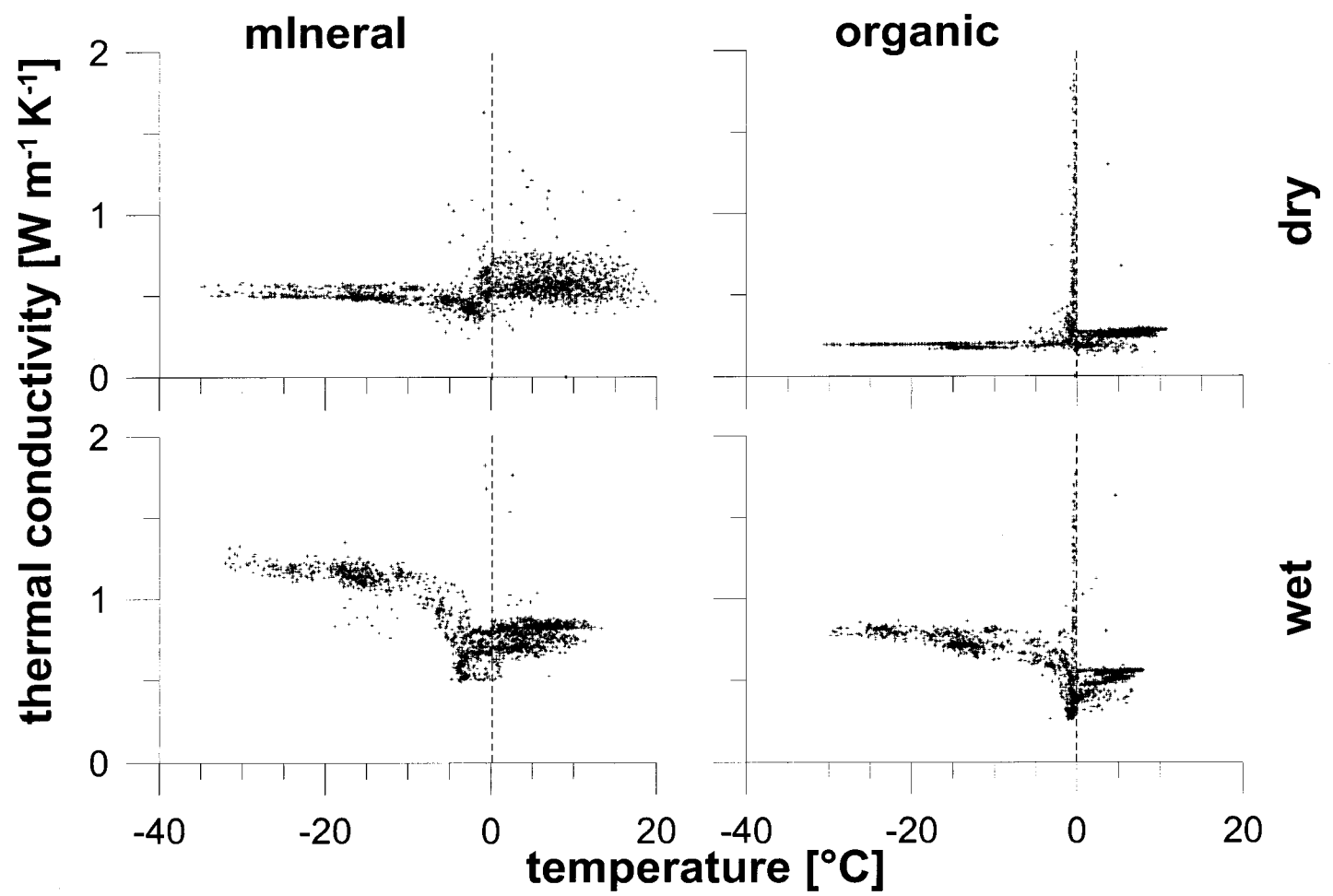
Figure B.2. Thermal conductivity [W m^{-1} K^{-1}] plotted as a function of soil temperature [°C] for the sensors described in Figure B.1.